Adsorbate-Induced Faceting of Transition Metal Surfaces

von
Payam Kaghazchi

im Fachbereich Physik der Freien Universität Berlin eingereichte
Dissertation zur Erlangung des akademischen Grades
DOCTOR RERUM NATURALIUM

Berlin 2009

Erstgutachter: Priv.-Doz. Dr. Timo Jacob
Zweitgutachter: Prof. Dr. Eberhard K. U. Gross
Disputationstermin: 01. Juli 2009

For Hadiyeh
and my parents

Contents

1 Introduction **1**

2 Method **5**

2.1 The Many-Body Problem 5
2.2 Born–Oppenheimer Approximation 6
2.3 Wave-Function-Based Methods 6
2.4 Density-Based Methods 7
2.4.1 The Thomas–Fermi Model 7
2.4.2 The Hohenberg–Kohn Theorems 8
2.4.3 The Kohn–Sham Approach 9
2.4.4 Exchange–Correlation Functionals 11
2.5 Periodic Systems 12
2.5.1 The Supercell Approach 13
2.5.2 Bloch Theorem 13
2.5.3 Sampling of The Brillouin Zone 14
2.5.4 Plane Waves 14
2.6 Pseudopotential Method 15
2.6.1 Norm Conserving Pseudopotentials 15
2.6.2 Ultrasoft Pseudopotentials 16
2.7 Multiscale Modeling 18
2.7.1 The *ab initio* Atomistic Thermodynamics Approach 18
2.8 Considerations on the Formation of Facets 21
2.8.1 Edge and Corner Energy 22
2.8.2 Strain Contribution 22
2.8.3 Facet Formation Condition 23

3 Experimental Observations on the Faceting of Re(11$\bar{2}$1) and Ir(210) 25

3.1 O/Re(11$\bar{2}$1) . . . 26
3.2 N/Re(11$\bar{2}$1) . . . 28
3.3 O/Ir(210) . . . 28
3.4 Applications of Faceted Surfaces . . . 29
3.4.1 The Use of Faceted Surfaces to Study Structure Sensitivity in Heterogeneous Catalysis . . . 29
3.4.2 The Use of Faceted Surfaces as Templates for Nanostructure Growth . . . 30

4 Properties of Bulk and Clean Surfaces 33

4.1 Bulk Properties . . . 33
4.1.1 Bulk Rhenium . . . 34
4.1.2 Density of States for Re Bulk . . . 36
4.1.3 Bulk Rhenium Oxide . . . 37
4.1.4 Bulk Rhenium Nitride . . . 39
4.2 Properties of the Clean Surfaces . . . 39
4.2.1 Re(11$\bar{2}$1) . . . 42
4.2.2 Re(10$\bar{1}$0)/Re(01$\bar{1}$0) . . . 43
4.2.3 Re(10$\bar{1}$1)/Re(01$\bar{1}$1) . . . 44
4.2.4 Re(13$\bar{4}$2)/Re(31$\bar{4}$2) . . . 45
4.2.5 Density of States for Re Surfaces . . . 46
4.2.6 Clean Rhenium Facets . . . 47

5 Oxygen and Nitrogen-covered Re Surfaces 49

5.1 Re(11$\bar{2}$1) . . . 50
5.1.1 O/Re(11$\bar{2}$1) . . . 51
5.1.2 N/Re(11$\bar{2}$1) . . . 52
5.2 Re(10$\bar{1}$0) . . . 54
5.2.1 Unreconstructed O/Re(10$\bar{1}$0)-(1×1) . . . 55
5.2.2 Reconstructed O/Re(10$\bar{1}$0)-(1×2) and -(1×3) . . . 58
5.2.3 Unreconstructed N/Re(10$\bar{1}$0)-(1×1) . . . 62
5.3 Re(10$\bar{1}$1) . . . 64

5.3.1 Unreconstructed O/Re(10$\bar{1}$1)-(1×1) 64
5.3.2 Reconstructed O/Re(10$\bar{1}$1)-(1×2) 66
5.3.3 Unreconstructed N/Re(10$\bar{1}$1)-(1×1) 68
5.3.4 Reconstructed N/Re(10$\bar{1}$1)-(1×2) 69
5.4 Re(13$\bar{4}$2) 71
5.4.1 O/Re(13$\bar{4}$2) 72
5.4.2 N/Re(13$\bar{4}$2) 73
5.5 Density of States of Adsorbate-covered Re Surfaces 76

6 Faceting of Re Surfaces **79**
6.1 Surface Phase Diagram of O/Re(10$\bar{1}$0) 80
6.2 Surface Phase Diagram of O and N/Re(11$\bar{2}$1) 84

7 Faceting of Ir(210) **91**
7.1 Experimental Observations 91
7.2 Oxygen-covered Ir Surfaces 92
7.2.1 O/Ir(210) 93
7.2.2 O/Ir(311) 95
7.2.3 O/Ir(110) 97
7.2.4 O/Ir(110)-Superstructure 98
7.3 Surface Phase Diagram of O/Ir(210) 100

8 Conclusions and Outlook **105**

A Convergence Tests **107**
A.1 Bulk Re 107
A.2 Bulk ReO_2 108
A.3 Molecular Properties 109
A.3.1 Oxygen 109
A.3.2 Nitrogen 111
A.4 Re Surfaces 112

B Binding Energies of O and N on Re Surfaces **117**
B.1 Re(11$\bar{2}$1) 117
B.2 Re(10$\bar{1}$0) 119
B.2.1 Unreconstructed Re(10$\bar{1}$0)-(1×1) 119
B.2.2 Reconstructed Re(10$\bar{1}$0)-(1×2) 120
B.2.3 Reconstructed Re(10$\bar{1}$0)-(1×3) 121
B.3 Re(10$\bar{1}$1) 124
B.3.1 Unreconstructed Re(10$\bar{1}$1)-(1×1) 124
B.3.2 Reconstructed Re(10$\bar{1}$1)-(1×2) 125
B.4 Re(13$\bar{4}$2) 126

References **129**

Summary **136**

Zusammenfassung **139**

Acknowledgements **141**

Curriculum Vitae **141**

Chapter 1

Introduction

Highly-disperse nanoparticles are often used to catalyze chemical reactions. Unfortunately, not all nanoparticles have the same size and shape, but show a relatively large distribution. Since the electronic properties of nanoparticles are correlated with their morphology, experimental measurements usually represent the averaged behavior of (almost) the entire ensemble of particles. This limits our understanding of the ongoing processes and makes direct comparison with theoretical studies difficult.
One way out of this dilemma is the formation of well-defined nanostructures or facets on single-crystal surfaces, which provide a reproducible basis and model systems for studying structural sensitivity in catalytic reactions.
Faceting, a form of self-assembly of nanometer-scale structures, occurs when an initially planar surface converts to a "hill-and-valley" structure, exposing new crystal faces of nanometer-scale dimensions. While clean surfaces rarely facet, adsorbate-induced faceting of surfaces, driven by the anisotropy of surface free energy, is a general phenomenon observed in many systems [1–3]. Usually, the resulting facets have more closely-packed surface structures than the original planar substrate, and the overall surface energy is reduced by facet formation, even though the total surface area may be increased. Although the enhancement of the anisotropy in surface free energy is the thermodynamic driving force for facet formation, in most cases this process is hindered by kinetic limitations. Therefore, not only is a critical adsorbate coverage required but also a minimum annealing temperature, allowing the system to overcome all kinetic barriers in the process of facet formation.
Studies of adsorbate-induced faceting can deepen our understanding of the stability of surfaces in contact with a reactive gas environment, which is essential for selecting and controlling a desired surface morphology. Faceted surfaces have also been used as model systems to study structural sensitivity in catalytic reactions [4–6] and may be used as templates to grow nanostructures [7, 8].
So far, adsorbate-induced faceting has been studied experimentally on various

metal surfaces such as W(111) [1,2], Mo(111) [9,10], Ni(210) [11,12], Pt(210) [13], Ir(210) [14], Rh(553) [15], Re(11$\bar{2}$1), and Re(12$\bar{3}$1) [16, 17], as well as vicinal Cu surfaces [18–21].
To understand the influence of differently strong interacting adsorbates on the surface morphology of transition metals, Dr. Hao Wang in the group of Prof. Dr. Theodore E. Madey from the Rutgers University has characterized faceting of Re(11$\bar{2}$1) in the presence of oxygen and nitrogen using LEED and STM [7]. Dosing a large amount of oxygen (exposure $>$ 100 L) at temperatures between 900 and 1000 K, the planar Re(11$\bar{2}$1) surface converts to a morphology with four-sided nanoscale pyramids exposing faces of (01$\bar{1}$0), (10$\bar{1}$0), (01$\bar{1}$1), and (10$\bar{1}$1) orientations (Fig. 1.1). Regarding nitrogen, which was introduced by exposing the system to ammonia at temperatures above 600 K, the initially planar Re(11$\bar{2}$1) surface becomes completely faceted at 900 K and a pressure of 5×10^{-10} atm. The facets that appear were characterized as ridge-like structures with faces having (13$\bar{4}$2) and (31$\bar{4}$2) orientations (Fig. 1.2). Interestingly, the facets resulting from nitrogen adsorption on Re(11$\bar{2}$1) are substantially different from those induced by oxygen.

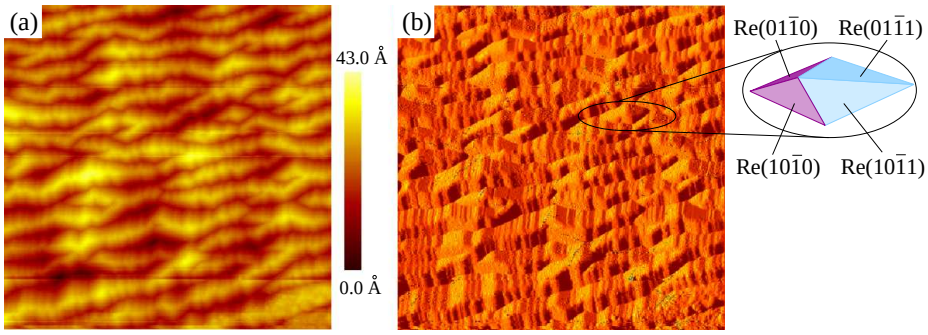

Figure 1.1: STM (a) and x-slope (b) images of the faceted Re(11$\bar{2}$1) surface prepared by oxygen adsorption (exposure of 300 L) at 1000 K. Both figures show a surface area of 1000 Å$\times$1000 Å. From ref. [7].

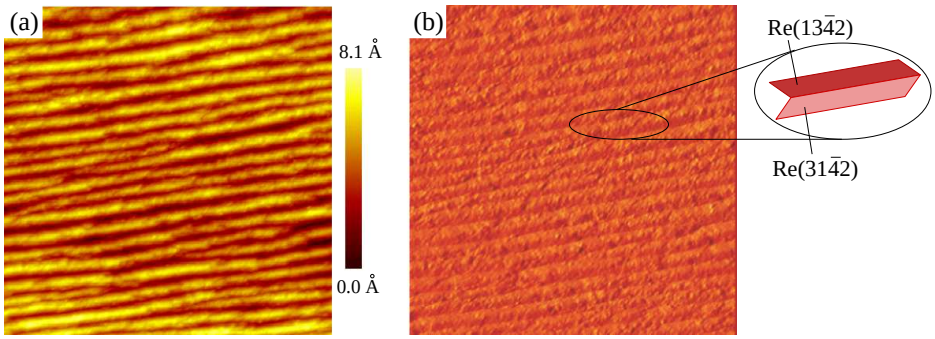

Figure 1.2: STM (a) and x-slope (b) images of the faceted Re(11$\bar{2}$1) surface prepared by ammonia adsorption (exposure of 300 L) at 900 K. Both figures show a surface area of 1000 Å$\times$1000 Å. From ref. [7].

Similar studies by Dr. Ivan Ermanoski in the group of Prof. Madey showed that O adsorption can induce faceting of Ir(210) [14,22]. Starting with planar Ir(210), which is a relatively open surface, and depositing oxygen at coverages > 0.5 ML, he could produce three-sided nanopyramids (Fig. 1.3) by annealing the O-covered Ir(210) surface to temperatures higher than 600 K.

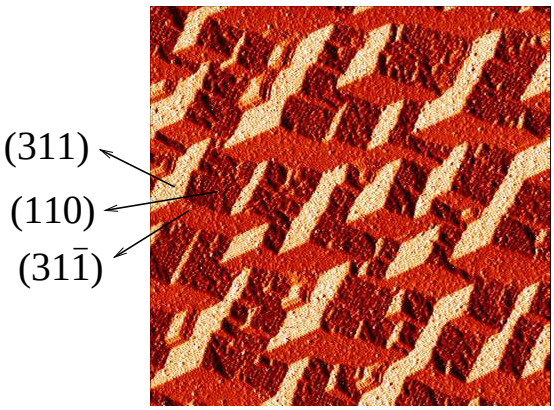

Figure 1.3: x-slope STM image (1000 Å×1000 Å) of O-covered faceted Ir(210) prepared by flashing Ir(210) in O_2 (5×10^{-8} Torr) to $T >$1700 K and subsequent cooling in O_2 to 300 K. Following a flash annealing in O_2, facets form as the crystal cools below ∼1150 K. From ref. [23].

There have been some advances in the theory of faceting. Oleksy has recently applied a simple solid-on-solid model [24–27] to study the adsorbate-induced faceting of different bcc (111) surfaces [28]. Using Monte Carlo simulations and assuming a constant coverage of one physical ML, his calculations showed that the facet size increased with annealing temperature and that disordered phases became relevant at higher temperatures. Furthermore, his simulations on the faceting–defaceting transition indicated a reversible process involving a hysteresis effect in the surface formation energy with respect to an alternating heat treatment. Besides mesoscopic approaches, first principles electronic structure calculations have also been used to provide information on the overlayer-induced faceting of few surfaces [29–32]. These studies in general showed that strongly interacting adsorbates enhanced the anisotropy in the surface free energy of both planar and faceted surfaces. However, these approaches have never been applied to open surfaces such as Re(11$\bar{2}$1) and Ir(210). In addition, the influence of pressure and temperature of the gas environment cannot be treated using these approaches.
In this thesis, motivated by experiments performed in the group of Prof. Madey, adsorbate-induced faceting of Re(11$\bar{2}$1) and Ir(210) has been studied using the *ab initio* atomistic thermodynamics approach in conjunction with density functional theory calculations. This approach allows us to evaluate the stability of surfaces in contact with a surrounding gas atmosphere under various temperature and

pressure conditions.
This work is organized as follows. In Chapter 2, the theoretical methods are described. Chapter 3 summarizes experimental results on the faceting of Re(11$\bar{2}$1) and Ir(210), while Chapter 4 shows the studies of properties of the rhenium bulk and clean surfaces, which are involved in faceting by forming four-sided pyramids (Re(10$\bar{1}$0) and Re(10$\bar{1}$1)) and ridge-like structures (Re(13$\bar{4}$2)) as well as planar surface (Re(11$\bar{2}$1)). The adsorption of O and N on the Re surfaces are the subject of Chapter 5. Here different overlayers and coverages are investigated. For the close-packed Re(10$\bar{1}$0) and Re(10$\bar{1}$1) surfaces, that showed indications for reconstructions, we also investigated these reconstructions. The obtained energies for all clean and adsorption systems are then used in Chapter 6 to construct phase diagrams for surface faceting on Re(11$\bar{2}$1) in the presence of an O or N atmosphere. In Chapter 7, we report oxygen-induced faceting of Ir(210). There calculations on the oxygen adsorption on Ir(210), (311), and (110) surfaces are discussed, concluding with the corresponding surface phase diagram for the faceting of Ir(210).

Chapter 2

Method

2.1 The Many-Body Problem

Many properties of materials that are of interest for physicists and chemists can be obtained by solving the many-body Schrödinger equation. This equation in stationary, non-relativistic treatment can be written as

$$H\Psi(\mathbf{r}_i\sigma_i, \mathbf{R}_I) = E\Psi(\mathbf{r}_i\sigma_i, \mathbf{R}_I), \tag{2.1}$$

where H is the Hamilton operator, $\Psi(\mathbf{r}_i\sigma_i, \mathbf{R}_I)$ the many-body wave function, E the total energy of the system, σ_i the spin coordinate of electron i, and finally $\mathbf{r}_i$ and $\mathbf{R}_I$ denote the spatial coordinate of electron i and nucleus I, respectively. The Hamiltonian for a system consisting of a set of nuclei and electrons can be written as[1]

$$H = -\sum_{I=1}^{N_n} \frac{1}{2M_I}\nabla_I^2 + -\sum_{i=1}^{N_e} \frac{1}{2}\nabla_i^2 + \sum_{I=1}^{N_n}\sum_{J>I}^{N_n} \frac{Z_I Z_J}{\mid \mathbf{R}_I - \mathbf{R}_J \mid} + \sum_{i=1}^{N_e}\sum_{j>i}^{N_e} \frac{1}{\mid \mathbf{r}_i - \mathbf{r}_j \mid} - \sum_{i=1}^{N_e}\sum_{I=1}^{N_n} \frac{Z_I}{\mid \mathbf{r}_i - \mathbf{R}_I \mid}, \tag{2.2}$$

where M_I is the mass and Z_I the atomic number of nucleus I and finally N_n and N_e are the total numbers of nuclei and electrons in the system. Here we have two species (electrons and nuclei), which interact with each other and themselves. It is difficult to solve such coupled system, since the motion of any particle is influenced by all others. Except for simple systems such as a hydrogen atom, the solution of eq. (2.1) with the corresponding Hamiltonian defined by eq. (2.2) is non-trivial for most materials that consist of several electrons and nuclei. Therefore, in order to solve realistic problems different approximations have to be applied.

[1]Equations have been expressed in atomic units throughout this thesis.

2.2 Born–Oppenheimer Approximation

Within the Born–Oppenheimer (BO) approximation (introduced by Max Born and J. Robert Oppenheimer in 1927 [33]) the electronic and ionic degrees of freedom are decoupled. It is based on the fact that the nuclei are much more massive than the electrons. Therefore, it is assumed that electrons would instantaneously follow the motion of the nuclei. Consequently, on the time-scale of the motion of the electrons, the ions appear almost stationary. With this assumption the total wave function of eq. (2.1) can be written as

$$\Psi(\mathbf{r}_i\sigma_i, \mathbf{R}_I) = \psi_e(\mathbf{r}_i\sigma_i, \{\mathbf{R}_I\})\, \psi_n(\mathbf{R}_I) \tag{2.3}$$

where $\psi_e(\mathbf{r}_i\sigma_i, \{\mathbf{R}_I\})$ and $\psi_n(\mathbf{R}_I)$ are the electronic and nuclei wave functions, and $\{\mathbf{R}_I\}$ denotes that nuclear spatial coordinates are parameters and not variables. Then we have divided the electronic and nuclear parts into

$$\begin{aligned} &H_e\psi_e(\mathbf{r}_i\sigma_i, \{\mathbf{R}_I\}) \\ &\quad= \left(-\sum_{i=1}^{N_e} \frac{1}{2}\nabla_i^2 + \sum_{i=1}^{N_e}\sum_{j>i}^{N_e} \frac{1}{\mid \mathbf{r}_i - \mathbf{r}_j \mid} - \sum_{i=1}^{N_e}\sum_{I=1}^{N_n} \frac{Z_I}{\mid \mathbf{r}_i - \mathbf{R}_I \mid} \right) \psi_e(\mathbf{r}_i\sigma_i, \{\mathbf{R}_I\}) \\ &\quad= E_e\psi_e(\mathbf{r}_i\sigma_i, \{\mathbf{R}_I\}) \end{aligned} \tag{2.4}$$

and

$$\left(-\sum_{I=1}^{N_n} \frac{1}{2M_I}\nabla_I^2 + \sum_{I=1}^{N_n}\sum_{J>I}^{N_n} \frac{Z_I Z_J}{\mid \mathbf{R}_I - \mathbf{R}_J \mid} + E_e(\mathbf{R}_I) \right) \psi_n(\mathbf{R}_I) = E_{\text{tot}}\psi_n(\mathbf{R}_I). \tag{2.5}$$

In eq. (2.4), H_e and ψ_e do not depend on the momenta of the nuclei, but only on their positions. In the case of negligible non-adiabatic effects, this approximation usually introduces a very small error to the energies and for heavier elements this inaccuracy becomes even smaller [34]. Applying this approximation, we can restrict ourselves to the electronic part (eq. (2.4))[2], which can be solved exactly only for one-electron systems. Thus, we need further approximations for systems with many electrons. There exist many attempts to solve the Schrödinger equation from first-principles (*ab initio*). Two common types of *ab initio* methods are the wave-function-based and the density-based approaches [35], which both have been applied extensively in material science.

2.3 Wave-Function-Based Methods

Hartree–Fock (HF) theory, which is the starting point for most quantum chemistry methods, is a wave-function-based method. In this theory, the total

[2]Although eq. (2.4) is main electronic contribution, in practice, we usually also consider the second term of eq. (2.5).

wave function is approximated by a single Slater determinant formed from a set of orthonormal single-particle orbitals. By minimizing the expectation value of the Hamiltonian with respect to the wave function, we can obtain both the energy and the wave function. In the HF method, exchange interaction, which is the consequence of imposing Pauli's principle on the electrons of like spin, is captured completely. This is because the many-body wave function (Slater determinant) fulfills the Pauli exclusion principle. The HF theory does not take into account the correlation coming from the Coulomb repulsion between electrons of like and unlike spins. Thus the calculated total energy is always larger than the exact total energy.
Although electron correlation contributions are very small, they usually affect the chemical properties of the considered system. In wave-function-based quantum chemistry, there are several ways to treat the correlation between electrons: configuration interaction (CI) [36], coupled cluster (CC) [37] or perturbation theory (such as MP2 and MP4) [38].

2.4 Density-Based Methods

Instead of employing many body wave functions, density-based methods use the electron density as the basic variable to evaluate the total energy and other properties. A well known density-based approach is the density-functional theory (DFT), which was introduced by Hohenberg and Kohn in 1964 [39] and further developed by Kohn and Sham in 1965 [40]. The origin of the widely used DFT method goes back to the works of Thomas and Fermi (TF). Therefore, before describing the DFT approach itself, we briefly review the TF model.

2.4.1 The Thomas–Fermi Model

The many-body wave function of an N_e electron system $\psi(\mathbf{r}_1\sigma_1, ..., \mathbf{r}_{N_e}\sigma_{N_e})$ is not easy to calculate, since it depends on $4N_e$ coordinates ($3N_e$ coordinates if spin is not considered). To reduce this complexity Thomas and Fermi proposed a model based on the electron density of the system $\rho(\mathbf{r})$ as the basic variable [41, 42].
The electron density of N_e electrons in a volume element $d\mathbf{r}_1$, is written as

$$\rho(\mathbf{r}_1) = N_e \int \mid \psi(\mathbf{r}_1\sigma_1, \mathbf{r}_2\sigma_2, ..., \mathbf{r}_{N_e}\sigma_{N_e}) \mid^2 d\sigma_1 d(\mathbf{r}_2\sigma_2)...d(\mathbf{r}_{N_e}\sigma_{N_e}). \qquad (2.6)$$

This electron density only depends on 3 instead of $3N_e$ spatial coordinates.
In the TF model, the ground-state (GS) total energy and other properties can be expressed as functionals of the electron density. By assuming that the kinetic

energy density is locally equal to that of a homogeneous electron gas, Thomas and Fermi formulated the total energy functional $E_{\mathrm{TF}}[\rho(\mathbf{r})]$ as

$$E_{\mathrm{TF}}[\rho(\mathbf{r})] = \frac{3(3\pi^2)^{\frac{2}{3}}}{10}\int \rho(\mathbf{r})^{\frac{5}{3}}d\mathbf{r} - Z\int \frac{\rho(\mathbf{r})}{\mathbf{r}}d\mathbf{r} + \frac{1}{2}\int\int \frac{\rho(\mathbf{r})\rho(\mathbf{r}')}{\mid \mathbf{r}-\mathbf{r}' \mid}d\mathbf{r}d\mathbf{r}', \quad (2.7)$$

where the first term is the kinetic energy of non-interacting electrons, the second and third terms are the classical electrostatic energy of electron–nucleus attraction and electron–electron repulsion, respectively. The exchange energy, which has no classical analogue, was included as an additional term to the TF model later by Dirac [43]:

$$E_{\mathrm{x}}^{\mathrm{Dirac}} = -\frac{3}{4}\left(\frac{3}{\pi}\right)^{\frac{1}{3}}\int \rho(\mathbf{r})^{\frac{4}{3}}d\mathbf{r}. \quad (2.8)$$

In the resulting model (Thomas–Fermi–Dirac (TFD) model), the value of $E[\rho]$ is lower compared to that in the TF. This is due to the fact that the additional exchange term in the TFD is negative. But even by considering this correction the obtained total energies are not accurate, since the kinetic energy is poorly described in this approach. Although the TF model was not very successful in quantum chemistry and solid-state physics, it was the starting point for DFT in the sense of using the electron density for solving the many-body problem.

2.4.2 The Hohenberg–Kohn Theorems

The theoretical basis of DFT are two fundamental theorems, which have been formulated and mathematically proven by Hohenberg and Kohn [39] for non-degenerate ground states.
According to the first theorem, the electron density uniquely determines the external potential (the potential of the ions or nuclei), to within a constant. Therefore, the total electronic energy of a system E can be expressed as a functional of the electron density ρ

$$E[\rho] = T[\rho] + \int \rho(\mathbf{r})V_{\mathrm{ext}}(\mathbf{r})d\mathbf{r} + E_{ee}[\rho], \quad (2.9)$$

where $T[\rho]$ is the kinetic energy functional and $E_{ee}[\rho]$ is the electron–electron interaction energy and also a functional. By defining the Hohenberg–Kohn functional:

$$F_{\mathrm{HK}}[\rho] = T[\rho] + E_{ee}[\rho] \quad (2.10)$$

we obtain

$$E[\rho] = \int \rho(\mathbf{r}) V_{\text{ext}}(\mathbf{r}) d\mathbf{r} + F_{\text{HK}}[\rho]. \tag{2.11}$$

The exact solution to the Schrödinger equation could be obtained if we had an explicit expression for the universal functional of $F_{\text{HK}}[\rho]$. Unfortunately this expression is presently still unknown.
The electron–electron interaction $E_{ee}[\rho]$ can be written as

$$E_{ee}[\rho] = J[\rho] + E_{\text{ncl}}[\rho], \tag{2.12}$$

where the first term is simply the classical Coulomb repulsion and the second one is the non-classical part, which contains self-interaction correction, exchange, and Coulomb correlation energy.
The second Hohenberg–Kohn theorem provides the energy variational principle. It states that the ground-state density $\rho_0(\mathbf{r})$ is the density that minimizes $E[\rho]$

$$E_0 = E[\rho_0(\mathbf{r})] \leq E[\rho(\mathbf{r})] \tag{2.13}$$

with the following conditions on the electron density $\rho(\mathbf{r})$

$$\rho(\mathbf{r}) \geq 0 \text{ and } \int \rho(\mathbf{r}) d\mathbf{r} - N_e = 0. \tag{2.14}$$

The minimization of energy functional, which fulfills the Euler–Lagrange equation subject to the constraint of a constant number of electrons N_e (eq. (2.14)), can be written as

$$\mu = \frac{\delta E[\rho(\mathbf{r})]}{\delta \rho(\mathbf{r})} = V_{\text{ext}}(\mathbf{r}) + \frac{\delta F_{\text{HK}}[\rho(\mathbf{r})]}{\delta \rho(\mathbf{r})}, \tag{2.15}$$

where the Lagrange multiplier μ is the chemical potential of the electrons. Although by using this formulation all ground-state properties can be obtained exactly, the Hohenberg–Kohn theorems do not tell us how to find the universal functional $F_{\text{HK}}[\rho]$. Later on, Kohn and Sham [40] found rather accurate approximations for $F_{\text{HK}}[\rho]$. After them many others continued and are continuing this work.

2.4.3 The Kohn–Sham Approach

To approximate the universal functional $F_{\text{HK}}[\rho]$ defined by eq. (2.10), Kohn and Sham decomposed the exact kinetic energy functional $T[\rho]$ into two parts:

1. The kinetic energy of a system of non-interacting electrons T_{s} given by

$$T_{\text{s}} = -\frac{1}{2} \sum_{i=1}^{N_e} < \phi_i \mid \nabla^2 \mid \phi_i > \tag{2.16}$$

in which ϕ_i is a set of one-electron wave functions.

2. Whatever needed to describe the neglected interactions in this non-interacting system ($T - T_\mathrm{s}$).

The second contribution is a small correction and together with the non-classical part of the electron–electron interaction E_ncl are defined as exchange–correlation energy

$$E_{xc}[\rho] = (T[\rho] - T_s[\rho]) + (E_{ee}[\rho] - J[\rho]). \tag{2.17}$$

With this definition the energy functional eq. (2.9) can be written as

$$E[\rho] = T_\mathrm{s}[\rho] + \int \rho(\mathbf{r}) V_\mathrm{ext}(\mathbf{r}) d\mathbf{r} + J_\mathrm{ee}[\rho] + E_\mathrm{xc}[\rho]. \tag{2.18}$$

Finding suitable expressions for the $E_\mathrm{xc}[\rho]$ term is the main challenge in DFT development, since it consists of all contributions which so far are not known exactly. The Euler–Lagrange equation (2.15) can now be expressed as

$$\mu = \frac{\delta E[\rho(\mathbf{r})]}{\delta \rho(\mathbf{r})} = \frac{\delta T_\mathrm{s}[\rho(\mathbf{r})]}{\delta \rho(\mathbf{r})} + V_\mathrm{eff}(\mathbf{r}) \tag{2.19}$$

with

$$V_\mathrm{eff}(\mathbf{r}) = V_\mathrm{ext}(\mathbf{r}) + \int \frac{\rho(\mathbf{r}')}{\mid \mathbf{r} - \mathbf{r}' \mid} d\mathbf{r}' + V_\mathrm{xc}(\mathbf{r}), \tag{2.20}$$

where the exchange–correlation potential $V_\mathrm{xc}(\mathbf{r})$ is

$$V_\mathrm{xc}(\mathbf{r}) = \frac{\delta E_\mathrm{xc}[\rho(\mathbf{r})]}{\delta \rho(\mathbf{r})}. \tag{2.21}$$

The solution of eq. (2.19) is obtained by solving the following set of one-electron equations

$$\left[-\frac{1}{2}\nabla^2 + V_\mathrm{eff}(\mathbf{r}) \right] \phi_i = \epsilon_i \phi_i, \tag{2.22}$$

where the density of the real system can be constructed from the Kohn–Sham orbitals

$$\rho(\mathbf{r}) = \sum_{i=1}^{\mathrm{occ}} \mid \phi_i(\mathbf{r}) \mid^2, \tag{2.23}$$

where the summation runs over all occupied orbitals (occ). The eqs. (2.20), (2.22), and (2.23) are known as Kohn–Sham equations.
Here, V_eff depends on $\rho(\mathbf{r})$ that we are seeking for. To solve this problem we start with a guessed $\rho(\mathbf{r})$, determine V_eff from eq. (2.20) and then obtain a new

$\rho(\mathbf{r})$ from eqs. (2.22) and (2.23). This procedure is then repeated until $\rho(\mathbf{r})$ is converged and the total energy is obtained[3].
We could determine the exact total energy from the DFT method, if we would possess the exact exchange–correlation energy functional. Since this is not the case, one must approximate this functional. The problem of finding more accurate expression for this contribution is still a great challenge in DFT.

2.4.4 Exchange–Correlation Functionals

A simple approximation method for calculating the exchange–correlation term is called the local-density approximation (LDA). In the LDA, the exchange–correlation energy of an inhomogeneous system is obtained by assuming that the density locally can be treated as a uniform electron gas. The exchange–correlation energy then can be written as

$$E_{\mathrm{xc}}^{\mathrm{LDA}}[\rho] = \int \rho(\mathbf{r})\epsilon_{\mathrm{xc}}(\rho(\mathbf{r}))d\mathbf{r}, \tag{2.24}$$

where $\epsilon_{\mathrm{xc}}(\rho(\mathbf{r}))$ is the exchange–correlation energy per particle of the homogeneous electron gas and can be splitted into exchange and correlation terms

$$\epsilon_{\mathrm{xc}}(\rho(\mathbf{r})) = \epsilon_{\mathrm{x}}(\rho(\mathbf{r})) + \epsilon_{\mathrm{c}}(\rho(\mathbf{r})). \tag{2.25}$$

The exchange part is given by the Dirac expression (eq. (2.8))

$$\epsilon_{\mathrm{x}}(\rho(\mathbf{r})) = -\frac{3}{4}\left(\frac{3}{\pi}\right)^{\frac{1}{3}} \rho(\mathbf{r})^{\frac{1}{3}}. \tag{2.26}$$

The correlation component ϵ_{c} has been determined by Monte Carlo (MC) calculations for a uniform electron gas considering a number of different densities [34]. Although one might expect that the LDA is only valid for a slowly varying density that can locally be treated as a uniform electron gas, experience shows that this approximation is surprisingly successful in a wide range of problems in solid-state physics and materials science. However, for highly inhomogeneous systems, the LDA results are usually not very accurate. It is well known that in the LDA binding and cohesive energies are overestimated while bond lengths and lattice constants are underestimated.
An improvement to the LDA is the generalized-gradient approximation (GGA) in which, in addition to the density, the gradient of the density, $\nabla\rho(\mathbf{r})$, is included

$$E_{\mathrm{xc}}^{\mathrm{GGA}}[\rho] = \int \rho(\mathbf{r})\epsilon_{\mathrm{xc}}\left(\rho(\mathbf{r}), \nabla\rho(\mathbf{r})\right) d\mathbf{r}. \tag{2.27}$$

[3]This iterative process is known as the self-consistent field (SCF) approach.

One form of GGA introduced by Perdew, Burke, and Ernzerhof (PBE) [44] is widely used in surface physics. In this approximation the correlation energy is expressed as

$$E_{\mathrm{c}}^{\mathrm{GGA}}[\rho] = \int \rho \left[\epsilon_c^{\mathrm{unif}}(\rho) + H(\rho, t)\right] d\mathbf{r}, \tag{2.28}$$

with

$$H(\rho, t) = \gamma \ln\left[1 + \frac{\beta t^2}{\gamma}\left(\frac{1 + At^2}{1 + At^2 + A^2 t^4}\right)\right] \tag{2.29}$$

and

$$\gamma \simeq 0.031091;\ \beta \simeq 0.066725;\ A = \frac{\beta}{\gamma}\frac{1}{e^{-\epsilon_{\mathrm{c}}^{\mathrm{unif}}/\gamma} - 1};\ t = \frac{|\ \nabla\rho\ |}{2\left(\sqrt{\frac{4(3\pi^2\rho)^{1/3}}{\pi}}\right)\rho}. \tag{2.30}$$

Here t is a dimensionless density gradient.
The exchange energy in terms of an enhancement factor F_{x} is written as

$$E_{\mathrm{x}}^{\mathrm{GGA}}[\rho] = \int \rho \epsilon_{\mathrm{x}}^{\mathrm{unif}}(\rho) F_{\mathrm{x}}(s) d\mathbf{r}, \tag{2.31}$$

where $\epsilon_{\mathrm{x}}^{\mathrm{unif}}(\rho)$ is the exchange energy per particle of a homogeneous electron gas at point $\mathbf{r}$ (see eq. (2.26)) and s is another dimensionless density gradient

$$s = \frac{|\ \nabla\rho\ |}{2(3\pi^2\rho)^{1/3}\rho}. \tag{2.32}$$

Finally, the function $F_{\mathrm{x}}(s)$ is

$$F_{\mathrm{x}}(s) = 1 + \kappa - \frac{\kappa}{1 + \frac{\mu s^2}{\kappa}}, \tag{2.33}$$

where $\kappa = 0.804$ and $\mu \simeq 0.21951$.
In this work, we carried out GGA calculations using the PBE functional. We also performed some of the calculations using the LDA functional. By comparing the results provided by different functionals, one usually can estimate the uncertainties arising from E_{xc} for the computed quantities of interest.

2.5 Periodic Systems

Although the many-body problem has been simplified by employing DFT, calculating an extended systems still remains a formidable task. When studying extended systems, we have to obtain a wave function for each of the infinite number of electrons in the solid and an infinite basis set is also required to expand each of these wave functions. In order to make the problem tractable, we assume periodic boundary conditions and apply the Bloch theorem [45].

2.5.1 The Supercell Approach

To model a periodic system, the smallest possible unit cell representing the system is chosen and periodically repeated over all space. For the bulk materials this box of atoms is mostly set up by using the primitive unit cell of the crystal. For a surface the periodicity in direction perpendicular to the surface is broken. In the present work, in order to maintain the periodicity in this direction, surfaces are modeled by a periodic 3D structure containing crystal slabs separated by vacuum regions (see Fig. (2.1)). In this so-called supercell approach the surfaces are represented by the periodically repeated slabs. Note that it is essential to ensure that the interaction between neighboring slabs are decoupled by using a wide enough vacuum. A slab must be also thick enough to avoid the interactions of the two surfaces of slab via the bulk crystal. Therefore, the convergence of the vacuum size and slab thickness need to be carefully tested (see Appendix A).

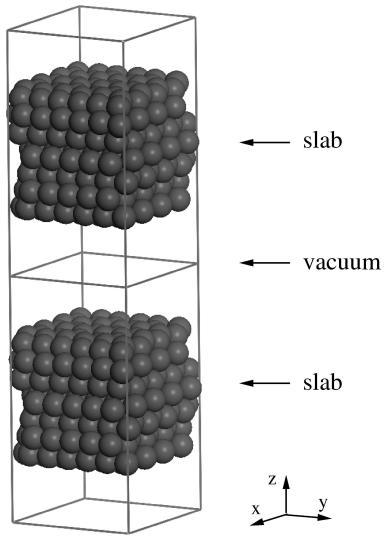

Figure 2.1: Schematic representation of the supercell approach for modeling a surface.

2.5.2 Bloch Theorem

The Bloch theorem states that each electronic wave function in a periodic solid can be written as the product of a periodic function, $u_{n,\mathbf{k}}(\mathbf{r})$, and a plane wave leading to

$$\psi_{n,\mathbf{k}} = u_{n,\mathbf{k}}(\mathbf{r})e^{i\mathbf{k}\cdot\mathbf{r}}, \tag{2.34}$$

where $\mathbf{k}$ is the wave vector that lies inside the first brillouin zone (Bz) and the index n, which is called the *band* index, labels the wave functions for the given $\mathbf{k}$. The function $u_{n,\mathbf{k}}(\mathbf{r})$ has the periodicity of the supercell and can be expanded using a set of plane waves

$$u_{n,\mathbf{k}}(\mathbf{r}) = \sum_{\mathbf{G}} c_{n,\mathbf{k}}(\mathbf{G})e^{i\mathbf{G}\cdot\mathbf{r}}, \tag{2.35}$$

where the wave vectors $\mathbf{G}$ are reciprocal lattice vectors fulfilling the following condition

$$\mathbf{G}\cdot\mathbf{L} = 2\pi\nu. \tag{2.36}$$

Here $\mathbf{L}$ are lattice vectors and ν is an integer number. Using the expression of eq. (2.35) for $u_{n,\mathbf{k}}(\mathbf{r})$, each wave function can be written as

$$\psi_{n,\mathbf{k}} = \sum_{\mathbf{G}} c_{n,\mathbf{k}}(\mathbf{G}) e^{i(\mathbf{k}+\mathbf{G})\cdot\mathbf{r}}. \tag{2.37}$$

On the basis of this theorem, for a periodic system, one can expand the Kohn–Sham wave functions by plane waves. Important advantages of plane waves are as follows: (i) they are mathematically simple and (ii) they are not biased to any specific position in the considered structure. All calculations of this work were performed using plane wave basis sets.

2.5.3 Sampling of The Brillouin Zone

The physical quantities of a system, such as the electron density and total energy, are obtained by performing integration in reciprocal space. Numerically, the integral over the Brillouin zone in reciprocal space can be transformed into a sum over only a finite number of $\mathbf{k}$-points, called the $\mathbf{k}$-point mesh:

$$\int_{\mathrm{BZ}} \frac{1}{\Omega_{\mathrm{BZ}}} d\mathbf{k} \rightarrow \sum_{\mathbf{k}} \omega_{\mathbf{k}}. \tag{2.38}$$

The error introduced by this approximation can be minimized if a sufficiently dense set of $\mathbf{k}$-points is used, but the computational effort grows quickly with the number of $\mathbf{k}$-points. Therefore, it is crucial to test the convergence of the results with respect to the number of $\mathbf{k}$-points and choose an appropriate mesh size to reach reasonable accuracy while using few computational resources. There are several methods to construct such $\mathbf{k}$-point meshes. In the present work the scheme proposed by Monkhorst and Pack [46] is used in which a homogeneous grid of $\mathbf{k}$-points is generated in the Brillouin zone and along the three axes in reciprocal space.

2.5.4 Plane Waves

In principle, infinite number of plane waves are required to obtain the electronic wave function exactly. However, in practice, a finite number of plane waves will give sufficiently accurate results. Thus, electronic wave functions can be expanded in plane waves with kinetic energies up to a certain cutoff, E_{cutoff},

$$\frac{1}{2} \mid \mathbf{k} + \mathbf{G} \mid^2 \leq E_{\mathrm{cutoff}}. \tag{2.39}$$

Employing a finite basis set introduces a new source of inaccuracy, which can be reduced by increasing the number of plane waves. Therefore, appropriate convergence tests have to be performed in order to find an E_{cutoff} above that the calculated property is converged to the required accuracy. In the following section, we show that applying pseudopotential (PP) approximation enables us to have accurate results by taking into account even fewer number of electrons.

2.6 Pseudopotential Method

Valence wave functions (ψ_{v}) show very large oscillations in the core region, since they must maintain the orthogonality with core states (ψ_{c}). A large number of plane waves would be required to reproduce the oscillations as well as to expand the core wave functions. It is well known that valence electrons determine most physical and chemical properties of solids, while the core electrons are tightly bound to the nucleus and their participation in bonding is only indirect. Thus, within the frozen core (FC) approximation [47], it is sufficient to calculate only the valence electrons explicity. The pseudopotential (PP) methods start with the FC approximation. In PPs, the potential of core electrons and ions ($V = V_{\text{core}} + V_{\text{ion}}$) are replaced by a weaker pseudopotential (V^{ps}) inside a defined cutoff radius r_{c}. Outside r_{c} the V^{ps} is assumed to be identical to the real potential. In addition, a pseudo wave function (ϕ^{ps}) is constructed so that it becomes equal to the all electron wave function (ψ) beyond r_{c} and nodeless inside the r_{c}.
Most pseudopotential calculations are based on either norm-conserving pseudopotentials (NCPP) or, more recently, ultrasoft pseudopotentials (USPP). All the results in the present study were obtained by employing the USPP. Since the concept of the USPP has a close relation to the NCPP, we first briefly describe the latter type.

2.6.1 Norm Conserving Pseudopotentials

Norm-conserving pseudopotentials are constructed to satisfy the following requirements [48]:

1. True and pseudo valence eigenvalues agree for a chosen atomic configuration.

2. True and pseudo wave functions match outside a chosen r_{c}.

3. Norm of the true and pseudo wave functions are equal inside r_{c} (norm-conservation).

4. The logarithmic derivatives of the true and pseudo wave functions agree at r_c.

5. The first derivative of the logarithmic derivatives of the true and pseudo wave functions with respect to the energy match at r_c.

The last three conditions ensure for an improved transferability among a variety of atomic configurations. Despite the success of NCPP in many systems, still a very large number of plane waves is needed to expand the wave functions in transition metals and first-row elements. For computational purposes, it is very important to reduce the size of the basis set as much as possible. It means that the pseudopotentials have to be chosen as soft (smooth) as possible to save the computational effort without compromising accuracy. One method, which can be used for this purpose, is the Ultrasoft Pseudopotential method.

2.6.2 Ultrasoft Pseudopotentials

Ultrasoft pseudopotentials were introduced by Vanderbilt [49] as an alternative to NCPPs that were discussed in the previous section. In this scheme, similar to NCPPs the real and pseudo wave functions match beyond r_c, while inside this cutoff radius the norm-conservation condition is removed. Relaxing this constrain allows one to use much smaller basis set in the calculations, but this introduces the following complication: the norm of the pseudo wave functions is not equal to that of the true wave functions for $r < r_c$ and the pseudo charge density cannot be calculated simply by $\sum_i \mid \phi_i^{\mathrm{ps}}(\mathbf{r}) \mid^2$. In order to calculate the pseudo charge density we have to add an augmentation charge (inside the core region), ρ_{au}, to the square of the pseudo wave functions as

$$\rho(\mathbf{r}) = \sum_i \mid \phi_i^{\mathrm{ps}}(\mathbf{r}) \mid^2 + \rho_{\mathrm{au}}(\mathbf{r}). \tag{2.40}$$

In this approach the total energy in the DFT framework is expressed as

$$E_{\mathrm{tot}} = \sum_i \langle \phi_i^{\mathrm{ps}} \mid T + V_{\mathrm{nonloc}} \mid \phi_i^{\mathrm{ps}} \rangle + \int V_{\mathrm{loc}}(\mathbf{r})\rho(\mathbf{r})d\mathbf{r} + \frac{1}{2}\int \frac{\rho(\mathbf{r})\rho(\mathbf{r}')}{\mid \mathbf{r} - \mathbf{r}' \mid} d\mathbf{r}d\mathbf{r}' + E_{xc}[\rho(\mathbf{r})], \tag{2.41}$$

where T is the kinetic energy operator, V_{loc} is the local part and V_{nonloc} the non-local component of the PP, which for one atom can be written as

$$V_{\mathrm{nonloc}} = \sum_{uv} D_{uv}^{(0)} \mid \beta_u \rangle \langle \beta_v \mid, \tag{2.42}$$

where the functions, β_u, and the coefficients, $D_{uv}^{(0)}$, together with $V_{\rm loc}$ determine the PP. The β_u are constructed in terms of spherical harmonics multiplied by radial functions, which vanish outside r_c. The $\rho_{\rm au}$ is then written as

$$\rho_{\rm au}(\mathbf{r}) = \sum_j \sum_{uv} Q_{uv}(\mathbf{r}) \langle \phi_j^{\rm ps} \mid \beta_u \rangle \langle \beta_v \mid \phi_j^{\rm ps} \rangle, \tag{2.43}$$

where the $Q_{uv}(\mathbf{r})$ are local augmentation functions in the core regions, which will be discussed later.

Generating USPPs [50]: For generating ultrasoft pseudopotentials all-electron (AE) calculations are performed for a reference configuration. The Schrödinger equation is solved for a set of reference energies E_{lmj}. After the all-electron wave functions (ψ_{lmj}) have been obtained, pseudo wave functions are generated such that they match ψ_{lmj} at r_c. A smooth local potential, $V_{\rm loc}$, is also determined such that it agrees with AE potential beyond r_c. Then local wave functions are defined as

$$|\chi_{lmj}\rangle = (E_{lmj} - T - V_{\rm loc}) \, |\phi_{lmj}^{\rm ps}\rangle. \tag{2.44}$$

χ_{lmj} is zero at $r > r_c$, where $V_{\rm loc}$ and $\phi_{lmj}^{\rm ps}$ become equal to $V_{\rm AE}$ and ψ_{lmj}, respectively.
Then the charge augmentation function is determined

$$Q_{uv}(\mathbf{r}) = \psi_u^*(\mathbf{r})\psi_v(\mathbf{r}) - \phi_u^{\rm ps*}(\mathbf{r})\phi_v^{\rm ps}(\mathbf{r}). \tag{2.45}$$

Here u and v run over the $\{lmj\}$. By constructing the matrix $\mathrm{B}_{uv} = \langle \phi_u^{\rm ps} \mid \chi_v \rangle$, the β_u functions are given by

$$|\beta_u\rangle = \sum_v (B^{-1})_{vu} |\chi_v\rangle. \tag{2.46}$$

The remaining components of the PP are obtained by the identity formula

$$\left[T + V_{\rm loc} + \sum_{uv} D_{uv} \mid \beta_u \rangle\langle \beta_v \mid \right] \mid \phi_u^{\rm ps} \rangle = E_u \left[1 + \sum_{uv} q_{uv} \mid \beta_u \rangle\langle \beta_v \mid \right] \mid \phi_u^{\rm ps} \rangle, \tag{2.47}$$

where $D_{uv} = B_{uv} + E_v q_{uv}$. Once the D_{uv} are determined, one can find the non-local coefficients (see eq. (2.42))

$$D_{uv}^{(0)} = D_{uv} - \int V(\mathbf{r})\rho(\mathbf{r}) d\mathbf{r} \tag{2.48}$$

and the local part of the PP

$$V_{\rm loc}^{\rm ion}(\mathbf{r}) = V_{\rm loc}(\mathbf{r}) - \int \frac{\rho(\mathbf{r}')}{\mid \mathbf{r} - \mathbf{r}' \mid} d\mathbf{r}' - V_{xc}(\mathbf{r}). \tag{2.49}$$

2.7 Multiscale Modeling

In material science we may distinguish three different length and time scales:

1. The microscopic scale, where the electrons and atomic nuclei predominantly determine the physical and chemical properties.

2. The mesoscopic scale, in which phenomenological theories are usually applied to microstructural elements such as grain boundaries and dislocations.

3. The macroscopic scale, where the continuum mechanics deals with quantities such as velocity, temperature, density, displacement, stress, and strain.

When we aim to determine the overall thermodynamics and properties of a system, multiple lengths and time regimes must be taken into account. Bridging the different scales to a more general framework is known as *multiscale modeling approach* [51, 52]. Such approaches enable us to study the properties of a system across scales.
The behavior of materials at the macroscopic regime can be determined by the interactions at the microscopic level. Here we employ DFT to treat electrons at the microscopic scale. Statistical mechanics is then used as a theoretical bridge between the microscopic and the macroscopic world. The stability of a particular surface structure is given by its surface free energy, γ, which is the energy required to create a unit surface area. In this work, the *ab initio* atomistic thermodynamics approach is used [53–56] to evaluate the (p,T)-dependent surface free energies from first principles. The surface free energies are then used with the facet formation conditions (see Section 2.8) to study the stability of different structures.

2.7.1 The *ab initio* Atomistic Thermodynamics Approach

DFT is a zero-temperature and -pressure technique and cannot be used to study the influence of temperature and pressure on surface properties in the macroscopic regime. But when combined with thermodynamic considerations it becomes an applicable tool for predicting surface properties under realistic environmental conditions at a specific temperature and pressure. Here, we discuss the thermodynamic considerations which can be used to construct surface phase diagrams for surface faceting.
We first assume that a surface is in thermodynamic equilibrium with different phases (e.g., a surrounding gas phase environment or a macroscopic bulk phase) that can give (or take) any amount of atoms to (or from) the surface without

changing the temperature or pressure. The appropriate thermodynamic potential for a (T, p)-ensemble is the Gibbs free energy G

$$G = U - TS + pV, \tag{2.50}$$

where U is the internal energy and S is the entropy. The stability of different surfaces can be compared through the surface free energy (γ), which is the energy required to create a unit surface area from the components (bulk and gas phase). The most stable surface structure under given conditions (temperature and pressure) is the one that has lowest surface free energy. This quantity can be obtained by subtracting from the Gibbs free energy of the particular slab (G_{surf}) the Gibbs free energies of the components and normalizing to the surface area, A, [56]

$$\gamma\left(T, p_i\right) \;=\; \frac{1}{A}\left[G_{\mathrm{surf}}(T, p_i, N_i) - \sum_i N_i \mu_i\left(T, p_i\right)\right], \tag{2.51}$$

where $\mu_i(T, p_i)$ is the chemical potential of the species of ith type, and N_i is the number of atoms of the ith species in the considered reservoir. In this work, indices O, N, and M refer to oxygen, nitrogen, and metal species. The chemical potential of surrounding gas phase can be described by ideal gas laws, which then enables us to relate μ_{gas} to specific temperatures and pressures. If we consider O_2 as the surrounding gas reservoir (a similar approach can also be applied for other gaseous environments) then we have

$$\mu_{\mathrm{O}}^{\mathrm{gas}}\left(T, p_{\mathrm{O_2}}\right) = \frac{1}{2}\left[E_{\mathrm{O_2}}^{\mathrm{tot}} + \bar{\mu}_{\mathrm{O_2}}\left(T, p^0\right) + k_{\mathrm{B}}\, T \ln\left(\frac{p_{\mathrm{O_2}}}{p^0}\right)\right]. \tag{2.52}$$

Here, $E_{\mathrm{O_2}}^{\mathrm{tot}}$ is the calculated total energy of an isolated O_2 molecule and $\bar{\mu}_{\mathrm{O_2}}(T, p^0)$ is the standard chemical potential at temperature T, which includes all the contributions from vibrations and rotations of the molecule, and the ideal gas entropy at 1 atm. Although the standard chemical potentials can be calculated from first principles, for the phase diagram, which will be discussed later, we used the corresponding $\bar{\mu}_{\mathrm{O_2}}(T, p^0)$ values from the JANAF thermodynamic tables [57].
The Gibbs free energy defined by eq. (2.50) can be written for solid phases as

$$G = E_{\mathrm{tot}} + F_{\mathrm{conf}} + F_{\mathrm{vib}} + pV, \tag{2.53}$$

where E_{tot} is the total energy, F_{conf} is the configurational free energy, and F_{vib} is the vibrational free energy. The largest contribution to eq. (2.53) arises from the first term E_{tot}, which in the present work is obtained by DFT calculations. An exact evaluation of F_{conf} needs large computational effort, since a huge number of possible configurations of adatoms and substrate must be studied for a given structure. This approach seems to be impractical for open surfaces, which have

been studied here, with large number of adsorbate sites. Fortunately for sufficiently low temperatures this term is usually much smaller than the total energy term in eq. (2.53) and is almost negligible. The vibrational free energy contains a zero point energy E^{ZPE} contribution and an entropy contribution S^{vib} as

$$F^{\mathrm{vib}}(T, V, N_{\mathrm{M}}, N_{\mathrm{O}}) = \int d\omega F^{\mathrm{vib}}(T, \omega)\sigma(\omega) = E^{\mathrm{ZPE}} - TS^{\mathrm{vib}}, \tag{2.54}$$

where $\sigma(\omega)$ is the phonon density of state (DOS), and the frequency-dependent function $F^{\mathrm{vib}}(T, \omega)$ is

$$F^{\mathrm{vib}}(T, \omega) = \frac{1}{2}\hbar\omega + k_{\mathrm{B}}T \ln\left(1 - e^{-\frac{\hbar\omega}{k_{\mathrm{B}}T}}\right). \tag{2.55}$$

The vibrational contribution to the surface free energy, γ^{vib}, is then obtained as the difference in the vibrational energy of atoms on the surface and in the reservoirs

$$\gamma^{\mathrm{vib}}(T, V) = \frac{1}{A}\int F^{\mathrm{vib}}(T, \omega)\left(\sigma_{\mathrm{surf}}(\omega) - N_{\mathrm{M}}\sigma_{\mathrm{M}}^{\mathrm{bulk}}(\omega) - \frac{N_{\mathrm{O}}}{2}\sigma_{\mathrm{O_2}}^{\mathrm{gas}}(\omega)\right) d\omega. \tag{2.56}$$

Although the entire phonon DOS for the surfaces can be obtained using DFT, in the present work we use the Einstein model in which the phonon DOS is simply a delta function at one characteristic frequency $\bar{\omega}$. If we assume that the vibrational frequency of the metal atoms in the clean surface is similar to that in the adlayer structure, then the vibrational contributions to γ coming from oxygen can be estimated by [58]:

$$\gamma^{\mathrm{vib}}(T) \sim \frac{1}{A}\left[\sum_{i}^{N_{\mathrm{O}}} F_i^{\mathrm{vib}}(T, \bar{\omega}_i^{\mathrm{surf}}) - \frac{N_{\mathrm{O}}}{2}F^{\mathrm{vib}}(T, \bar{\omega}_{\mathrm{O_2}}^{\mathrm{gas}})\right], \tag{2.57}$$

where $\bar{\omega}_i^{\mathrm{surf}}$ is the O–surface stretch frequency of the ith adsorbed oxygen in the corresponding configuration and $\bar{\omega}_{\mathrm{O_2}}^{\mathrm{gas}}$ is for the O_2 molecule in the gas-phase. Using this approach the vibrational contributions to γ were estimated for the most stable configurations determined in our calculations. In all cases, we found that these contributions are rather small and they cause no modifications in the ordering of surface phases. Therefore, in the present work vibrational contributions have not been included.

It can be seen from a dimensional analysis that the last term of eq. (2.53), pV term, will be less than ~ 0.001 meV/Å^2 for pressures up to 1 atm and can therefore be neglected.

Finally, we come to the conclusion that the temperature and pressure dependence of the solid phases (surface and bulk) is expected to be much smaller than that of gaseous phases, whose chemical potential dominates the T- and p-dependence of the surface free energies. Therefore, the difference in the Gibbs free energy of the slab and the bulk can be replaced by their corresponding total energies, which then can be evaluated using first-principles approaches.

2.8 Considerations on the Formation of Facets

A geometric way to determine the equilibrium crystal shape (ECS) of a system has been proposed by Wulff [59]. If the orientation-dependent surface free energy is known for the system, one can obtain the so-called Wulff plot, which is a polar plot of surface free energy (γ) versus orientation. Then the ECS is given by the inner envelope of planes perpendicular to the radius vector at each point of this polar plot.
Further developments on the theory of the thermodynamic stability of crystal surfaces have been made by Herring [60]. The important conclusion of Herring's work was:"If a given macroscopic surface of a crystal does not coincide in orientation with some portion of the boundary of the equilibrium shape, there will always exist a hill-and-valley structure, which has a lower free energy than a flat surface, while if the given surface does occur in the equilibrium shape, no hill-and-valley structure can be more stable." Therefore, under certain conditions a flat surface minimizes the overall γ by converting to a "hill-and-valley" structure, exposing new crystal faces.
Since facet formation is thermodynamically driven, the important quantity is the formation energy, which can be expressed as a sum of changes in the Gibbs free energies, mainly related to surface, edge, corner, and strain contributions:

$$\Delta G^{\text{form}} = \Delta G^{\text{surface}} + \Delta G^{\text{edge}} + \Delta G^{\text{corner}} + \Delta G^{\text{strain}} + \dots \tag{2.58}$$

In the case of facet formation on the initially planar surface, the first term, $\Delta G^{\text{surface}}$ is expressed as

$$\Delta G^{\text{surface}} = \sum_f A_f^{\text{final}} \gamma_f^{\text{final}} - A^{\text{initial}} \gamma^{\text{initial}}, \tag{2.59}$$

where the initial surface is characterized by the surface free energy γ^{initial} and an overall surface area A^{initial}, and the fth face of the facets accordingly by γ^{final} and A^{final}. The change in Gibbs free energy for edges and corners, ΔG^{edge} and ΔG^{corner}, are given by [61]:

$$\Delta G^{\text{edge}} = \sum_i L_i \Gamma_i, \tag{2.60}$$

and

$$\Delta G^{\text{corner}} = \sum_j W_j \beta_j, \tag{2.61}$$

where the Γ_i is the edge free energy of the edge i with the length L_i, while β_j and W_j are the corner free energy and the number of corners j, respectively. The last term in eq. (2.58), ΔG^{strain}, is related to elastic strain relaxation at the facet edges.

2.8.1 Edge and Corner Energy

Although, for certain systems, contributions from edges and corners have been found to play a substantial role in the growth and stabilization of facets over planar surfaces, the evaluation of these contributions is rather demanding for atomistic calculations. We are not aware of any first-principles theoretical study on edge and corner free energies. Note that edge energies defined here are different from the step energies, which have been investigated extensively. For some systems there exist experimental estimations of the edge energy. However, none of this information is available for the structures studied in the present work.
For large facets the number of atoms in the edges and corners are considerably less than that in the faces of the facets. In this case, the importance of edges and corners is expected to be much smaller than that of surfaces, and therefore usually omitted [61]. Consequently, so far, theoretical studies have been limited to systems that show a high enough anisotropy in surface free energy but additionally small edge and corner energies [23]. In this thesis, we have also neglected the contributions of edges and corners to the overall free energy.

2.8.2 Strain Contribution

For homogenous systems as studied here, the strain energy change is mainly due to the elastic relaxation energy at crystal edges where the intrinsic surface stress tensor $\tau_{\alpha\beta}$ has a discontinuity. The elastic energy as a function of strain ϵ_{xy} is given by the following general formula [62]

$$E_{el} = \frac{1}{2}\int \lambda_{ijlm}\epsilon_{ij}\epsilon_{lm}dV + \int \tau_{\alpha\beta}(\mathbf{m})\epsilon_{\alpha\beta}dA, \tag{2.62}$$

where λ_{ijlm} have the meaning of surface excess elastic moduli and $\mathbf{m}$ is the coordinate-dependent unit vector normal to the surface at each point. Here $\tau_{\alpha\beta}(\mathbf{m})$ has components only in the surface plane (α, β=1,2). The values of $\tau_{\alpha\beta}(\mathbf{m})$ can be negative (compressive) or positive (tensile). For a compressive stress surface relaxes by expansion, while for a tensile stress surface favors contraction near the edges. The divergence of the surface stress tensor gives an effective force at the crystal edges. This force causes the strain field, leading to the changes in the stability of a faceted surface. However, the strain free energy near the edges of large facets has usually negligible influence on the stability of the facets. Therefore, through this study we have not accounted for these contributions to the overall free energy.

2.8.3 Facet Formation Condition

Assuming the facets to be large, the overall formation energy can be approximated by the surface contribution only. On the basis of this assumption with the definitions of eqs. (2.58) and (2.59), facet formation should occur when

$$\Delta G^{\text{form}} \approx \Delta G^{\text{surface}} = \sum_f A_f^{\text{final}} \gamma_f^{\text{final}} - A^{\text{initial}} \gamma^{\text{initial}} < 0. \tag{2.63}$$

Since, in the present case, facets showing different faces are formed on the initially planar surface after adsorption of an adsorbate (e.g. gaseous), eq. (2.63) converts into the following condition, which has to be fulfilled in order to show facet formation

$$\sum_f \frac{S_f}{\cos \vartheta_f} \cdot \gamma_f^{\text{final}} \left(T, p_{\text{gas}}\right) < \gamma^{\text{initial}} \left(T, p_{\text{gas}}\right). \tag{2.64}$$

Here, the parameters S specify the partial contributions of the different faces to each nano-shaped facet, while ϑ are the tilt angles of the faces with respect to the initial substrate, T is the temperature and p_{gas} is the partial pressure of the surrounding gas, whose adsorption induces the faceting. While all previously mentioned parameters are either given by the experimental conditions (*i.e.*, T and p_{gas}) or can be obtained by geometrical considerations (*i.e.*, S and ϑ), the remaining information required for eq. (2.64) are the surface free energies of the initial substrate, as well as the faces of the final facets. To evaluate the different surface free energies relevant to eq. (2.64), the *ab initio* atomistic thermodynamics approach (see Section 2.7.1) can be used, which allows one to evaluate the stability of surfaces/interfaces that are in contact and in thermodynamic equilibrium with a surrounding atmosphere.

Chapter 3

Experimental Observations on the Faceting of Re(11$\bar{2}$1) and Ir(210)

The formation of facets on solid surfaces is generally driven thermodynamically by the anisotropy in the surface free energy but limited by kinetics. Before discussing specific faceted surfaces, we begin by summarizing several general characteristics of faceting [23].

1. The spontaneous faceting of clean planar metal surfaces is not commonly observed, because the anisotropy in surface free energy is generally too small for an atomically-rough surface to form facets.

2. The faceting of initially planar surfaces is facilitated by the adsorption of gases or metallic adsorption that enhance the anisotropy of the surface free energy. The development of faceted structures on surfaces demonstrates that the minimum in surface free energy does not imply a minimum in surface area; the surface area of faceted substrates is often a few percent higher than that of the original planar substrate. When 3-D faceted features appear, the surfaces of the facets are generally more close-packed and invariably have a lower overall surface free energy than the initial atomically-rough planar surface.

3. Although faceting is driven by thermodynamics, *i.e.*, the minimization of surface free energy, it is controlled by kinetic barriers (*i.e.*, the kinetics of diffusion and nucleation), meaning that mass transport generally limits facet growth. In general, there is a material-dependent "temperature window" within which facets are observed. At low temperatures, an adsorbate-covered surface can be metastable; as the temperature increases, kinetic barriers to diffusion and nucleation are overcome and facets form. Facet

sizes increase over a limited range of temperatures as the edge density is minimized. At high temperatures, the desorption of adsorbates and/or temperature-dependent surface free energies reduce the anisotropy of surface free energy, and the surface relaxes back to planar.

A schematic of the faceting process is shown in Fig. 3.1. Faceting of an initially planar surface with a relatively high surface free energy (*i.e.*, a surface that is rough on the atomic scale, such as bcc W(111), fcc Ir(210) or hcp Re(11$\bar{2}$1)) is facilitated by the adsorption of gases and metallic adsorbates.
In the following sections (3.1–3.3), we will discuss oxygen and nitrogen-induced faceting of Re(11$\bar{2}$1) that has been studied by Dr. Hao Wang [7] as well as oxygen-induced faceting of Ir(210) that has been studied by Dr. Ivan Ermanoski [14, 22] in the group of Prof. Dr. Theodore E. Madey from the Rutgers University. They investigated faceting of Re(11$\bar{2}$1) and Ir(210) by using LEED and STM. The utilization of faceted surfaces in studying structure sensitive reactions (*e.g.*, CO oxidation or ammonia decomposition) and as templates for growth of metallic nanostructures is the subject of Section 3.4.

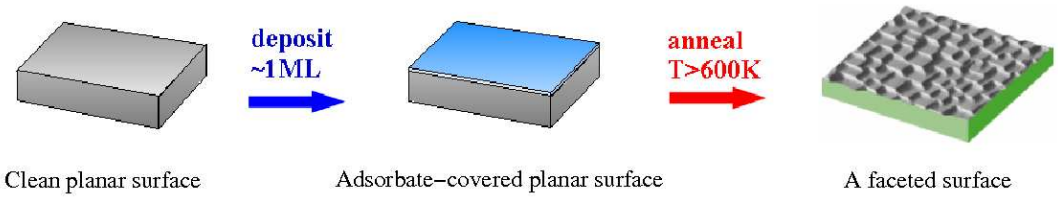

Figure 3.1: A schematic of the faceting process on a planar surface. Facets form when the adsorbate-covered surface is heated and kinetic barriers are overcome. From ref. [23].

3.1 O/Re(11$\bar{2}$1)

For initially planar Re(11$\bar{2}$1), depositing oxygen at room temperature with exposures less than 30 L, followed by annealing at elevated temperatures causes the planar Re(11$\bar{2}$1) surface to become partially faceted with (11$\bar{2}$1) and (10$\bar{1}$0) faces forming zig-zag chains (see Fig. 3.2). Dosing a larger amount of oxygen (exposure $>$ 100 L) at temperatures between 900 and 1000 K, the surface converts to a morphology with four-sided nanoscale pyramids exposing faces of (01$\bar{1}$0), (10$\bar{1}$0), (01$\bar{1}$1), and (10$\bar{1}$1) (see Fig. 3.3).
By performing LEED simulations, Wang *et al.* also proposed that the Re(10$\bar{1}$1) faces on the oxygen-covered faceted Re(11$\bar{2}$1) surface are reconstructed and have a (1×2) missing-row structure.
Although the oxygen-covered Re(10$\bar{1}$0) facets, which are formed on the four-sided

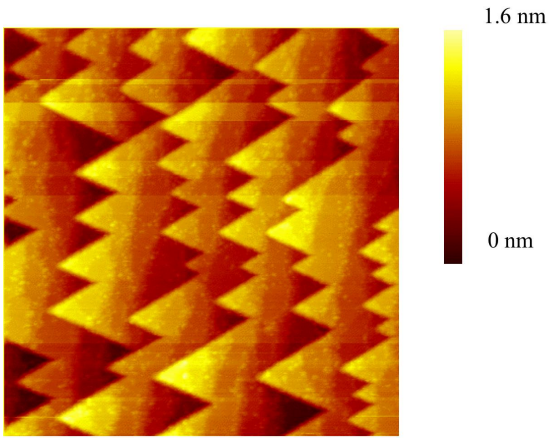

Figure 3.2: STM image (1000 Å×1000 Å) of the partially faceted Re(11$\bar{2}$1) surface, prepared by dosing 10 L O_2 at 300 K and annealing at 1000 K. From ref. [7].

pyramids in addition to the Re(10$\bar{1}$1) facets, have not been investigated in details by Wang *et al.*, experimental studies for O adsorption on the planar Re(10$\bar{1}$0) have been performed previously by Zehner *et al.* [63] and Lenz *et al.* [64].
In the first experiments, Zehner *et al.* showed the existence of facets parallel to the (10$\bar{1}$1) plane after oxygen exposure (60000 L) at pressures of $1.3\times\ 10^{-7}$ atm or higher and temperatures of $T \geq 888$ K. These facets were replaced by a (1×3) overlayer on the initial (10$\bar{1}$0) surface at $T \geq 1298$ K. Later, Lenz *et al.* could observe the (1×3) pattern after O adsorption for exposures higher than 4 L ($p < 10^{-13}$ atm). They additionally reported a variety of oxygen overlayers at lower coverages: (2×3) for 0.3 L, c(2×4) for 0.7 L, (1×5) for 3.2 L, and (1×4)-2O for 3.7 L. These overlayers were prepared by annealing the system at $520 < T < 650$ K. They indeed observed no (10$\bar{1}$1) facets on this surface.

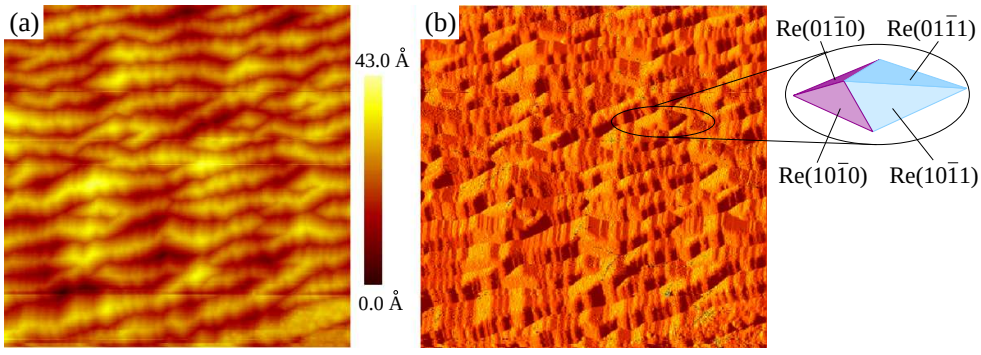

Figure 3.3: STM (a) and x-slope (b) images of the faceted Re(11$\bar{2}$1) surface prepared by oxygen adsorption (exposure of 300 L) at 1000 K. Both figures show a surface area of 1000 Å×1000 Å. From ref. [7].

3.2 N/Re(11$\bar{2}$1)

Regarding nitrogen, which was introduced by exposing the system to ammonia at temperatures above 600 K, where it decomposes to leave only N atoms on the surface, the initially planar Re(11$\bar{2}$1) surface becomes completely faceted at 900 K and a pressure of 5×10^{-10} atm. The facets that appear were characterized as ridge-like structures with faces having (13$\bar{4}$2) and (31$\bar{4}$2) orientations (Fig. 3.4). Therefore, the facets resulting from nitrogen adsorption on Re(11$\bar{2}$1) are substantially different from those induced by oxygen that was discussed in Section 3.1.

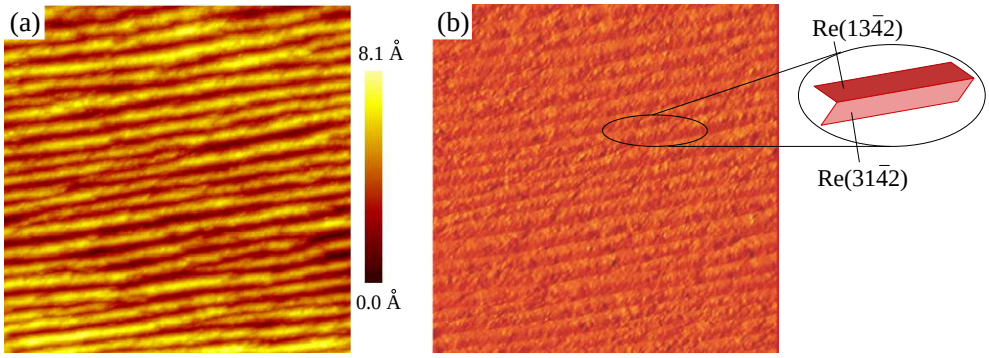

Figure 3.4: STM (a) and x-slope (b) images of the faceted Re(11$\bar{2}$1) surface prepared by ammonia adsorption (exposure of 300 L) at 900 K. Both figures show a surface area of 1000 Å×1000 Å. From ref. [7].

3.3 O/Ir(210)

Similar experimental studies have also been performed on oxygen-induced faceting on Ir(210). When atomically-rough Ir(210) is covered with more than a 0.5 ML of oxygen and annealed to 600 K, nanoscale three-sided pyramidal facets grow and cover the surface [14, 22]. LEED and STM (Fig. 3.5(a)) revealed that these facets, which completely covered the surface, expose faces of Ir(311), Ir(31$\bar{1}$), and Ir(110). Furthermore, the higher resolution STM-image 3.5(b) showed that while the (311) and (31$\bar{1}$) faces are always unreconstructed, some (110) faces are partially reconstructed. This so-called superstructure was proposed to be a "stepped double-missing-row"-(110) surface [65].
After facet formation, oxygen that still remains on the surface can be removed by reaction with H_2 at $T = 400$ K [4]. During this reaction the nanopyramidal surface structure is not affected, since the kinetic barrier of facet destruction is not reached at these low temperatures. The clean nanofacets remain stable up to $\sim$ 600 K, and for higher temperatures the surface reverts to the original

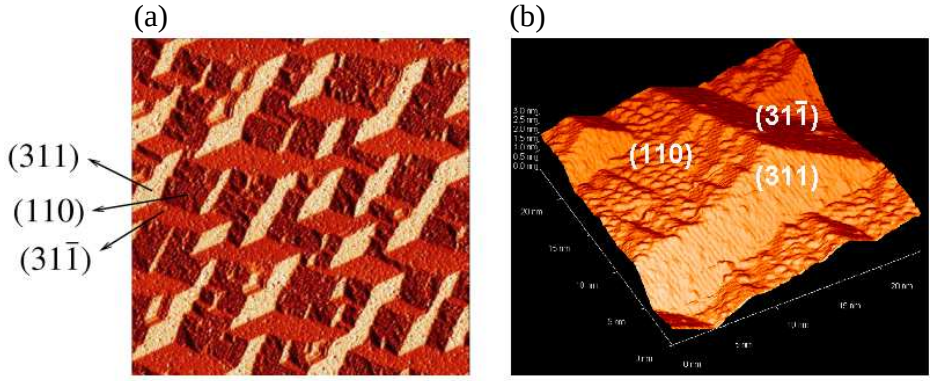

Figure 3.5: (a) STM derivative image (1000 Å×1000 Å) of O-covered faceted Ir(210) prepared by flashing Ir(210) in O_2 (5×10^{-8} Torr) to $T > 1700$ K and subsequent cooling in O_2 to 300 K. Following a flash annealing in O_2, facets form as the crystal cools below ~ 1150 K. (b) STM scan (240 Å×240 Å) of one pyramid of O-covered faceted Ir(210), showing the superstructure on the (110) facet. From ref. [23].

planar Ir(210). By changing the annealing temperature for the formation of oxygen-covered faceted Ir(210), nanopyramids with average sizes ranging from 5 to 14 nm can be generated [5].

3.4 Applications of Faceted Surfaces

The faceted surfaces provide unsupported monometallic substrates with a well-defined structure and controlled size, which can be used in studies of structure sensitive reactions and as templates for growth of metallic nanostructures.

3.4.1 The Use of Faceted Surfaces to Study Structure Sensitivity in Heterogeneous Catalysis

Nanoparticles that are often used to catalyze chemical reactions do not have the same size and shape and show a relatively large distribution. On the other hand, size distribution of facets is narrow and the average facet size is tunable by changing annealing temperature and time. In addition, structurally different surfaces can be prepared from the same single crystal and the results of chemical reactions from these facets and initially planar surface can be compared *in situ*. Therefore, faceted surfaces are attractive model systems for heterogeneous catalysis.
There are many studies to show differences in surface reactions on planar and faceted surfaces. Evidence has been found for structure sensitivity in *n*-butane

hydrogenolysis on planar and faceted Pt/W(111) surfaces [66] as well as acetylene reactions over planar and faceted Pd/W surfaces [67].
Recently, faceted Ir(210) has also been used for studies of surface reactions whose rates are sensitive to atomic structure and/or nanoscale (facet) size: (i) NO decomposition [68], (ii) CO oxidation [6], (iii) decomposition of H_2 and NH_3 [5], and (iv) decomposition of acetylene [4]. The selected results are summarized as follows:

1. Studies on the adsorption and decomposition of NO over planar Ir(210) and nanofaceted Ir(210) with tunable facet sizes (5–14 nm) show structure sensitivity in adsorption sites and thermal decomposition of NO on planar Ir(210) versus those on faceted Ir(210). Significant differences are seen in desorption rates of N_2, NO, and N_2O between the planar and the faceted surfaces toward NO decomposition. On planar Ir(210) NO adsorbs on atop sites for the entire NO coverage range. On faceted Ir(210) that contains (110) and {311} faces, NO adsorbs on bridge and atop sites at low NO coverage while only on atop sites at high NO coverage. No evidence has been found for size effects in the thermal decomposition of NO over faceted Ir(210) for average facet size ranging from 5 to 14 nm [5].

2. Structure sensitivity in CO oxidation on planar *vs.* faceted Ir(210) is evidenced by differences in desorption rates of CO_2 between the planar and the faceted surfaces. Similar to the case of decomposition of NO, CO oxidation over faceted Ir(210) in not sensitive to average facet size.

3. The first observation of size effects in surface chemistry on an unsupported monometallic catalyst with a well-defined structure and tunable size is reported for decomposition of NH_3 on faceted Ir(210).

3.4.2 The Use of Faceted Surfaces as Templates for Nanostructure Growth

The faceted substrates have been used as nanotemplates for the growth of metallic nanostructures and nanowires: Wang *et al.* [7,8] used O-covered faceted Re(12$\bar{3}$1) as a nanotemplate for the growth of Co particles in 1-D arrays and found that Co nanoparticles nucleate preferentially in the troughs (Fig. 3.6), but not atop the ridges. These observations indicate that nanofacets could be promising candidates for producing model supported catalysts with a controlled size. In addition, it has been suggested by Gai *et al.* [69] that an excellent nanotemplate for growing "quantum wires" may be created after annealing certain crystallographic orientations of Si to a sufficiently high temperature. Later on, Ohmori *et al.* [70] showed

that Ge nanowires are grown on an annealed Si surface, which has a "hill-and-valley"-like structure.

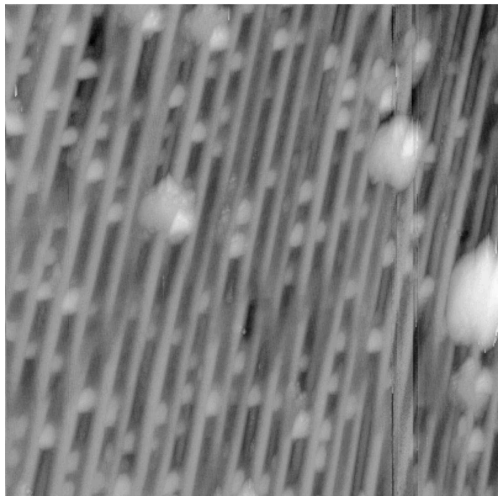

Figure 3.6: STM image (3500 Å×3500 Å) showing 1-D arrays of Co clusters on a faceted O/Re(12$\bar{3}$1) surface. From ref. [7].

Chapter 4

Properties of Bulk and Clean Surfaces

In this work, all first-principles calculations were performed with the CASTEP (CAmbridge Serial Total Energy Package) code [71], which implements density functional theory (DFT) within the plane-wave pseudopotential[1] method as discussed in Chapter 2. The exchange-correlation energies were evaluated with the Perdew-Burke-Ernzerhof (PBE) [44] form of the generalized-gradient approximation (GGA). In order to evaluate the influences coming from choosing the PBE exchange-correlation functional, we repeated some of the calculations using the local-density approximation (LDA) functional. In addition, the geometries of all structures were fully optimized (to $< 0.03\,\mathrm{eV/\AA}$) by using the BFGS (Broyden–Fletcher–Goldfarb–Shanno) [72] method, which has been implemented in the CASTEP code.

4.1 Bulk Properties

To construct the unstrained surfaces within the supercell geometry we need to calculate the equilibrium lattice constants of the bulk crystal. Another important material property is the bulk modulus, which is the curvature of $E(V)$ close to the equilibrium volume and defined by the equation:

$$B(T,V) = V\left(\frac{\partial^2 E}{\partial V^2}\right)_T . \tag{4.1}$$

In theoretical calculations, the equilibrium atomic volume V_0 and, accordingly, the equilibrium lattice constants (a_0, b_0, and c_0), as well as the bulk modulus B_0 are

[1] For all atoms the core electrons were replaced by Vanderbilt ultrasoft pseudopotentials (USPP) [49].

evaluated by fitting a set of energies for different unit cell volumes to an analytical equation of state such as proposed by Murnaghan [73] or Rose [74]. According to the Murnaghan equation of states, the dependence of the total energy E on the unit cell volume V can be represented by the following relationship:

$$E(V) = E(V_0) + \frac{B_0 V_0}{B_0'(B_0' - 1)} \left[B_0' \left(1 - \frac{V_0}{V}\right) \left(\frac{V_0}{V}\right)^{B_0'} - 1 \right], \tag{4.2}$$

where $E(V_0)$ is the energy at the equilibrium atomic volume of V_0 and B_0' is the derivative of the bulk modulus with respect to the pressure at p=0. For hexagonally close-packed (hcp) solids (a=b≠c), the total energy of the bulk $E_{\mathrm{tot}}(V, c/a)$ is a function of both the volume and the ratio between the lattice vectors c and a. In this case the total energy versus volume for several reasonably chosen c/a close to the experimental values are evaluated. The c/a and V corresponding to the minimum energy then determine the equilibrium lattice constants (a_0 and c_0).
The cohesive energy is another basic property of the crystals and is defined as the energy cost to remove an atom from the bulk:

$$E_{\mathrm{coh}} = \frac{E_{\mathrm{tot}}^{\mathrm{bulk}}(a_0, c_0) - N_{\mathrm{atom}} E_{\mathrm{tot}}^{\mathrm{atom}}}{N_{\mathrm{atom}}}. \tag{4.3}$$

Here, $E_{\mathrm{tot}}^{\mathrm{bulk}}(a_0, c_0)$ is the total energy of bulk, which is obtained at the equilibrium lattice parameters (a_0, c_0), $E_{\mathrm{tot}}^{\mathrm{atom}}$ is the total energy of an isolated atom, and N_{atom} is the number of atoms in the bulk unit cell.
Another useful quantity that has been calculated in the present study is the projected density of state (PDOS)

$$D_\alpha(\epsilon) = \sum_{i=1}^{\infty} | \langle \varphi_\alpha \mid \phi_i \rangle |^2 \delta(\epsilon - \epsilon_i). \tag{4.4}$$

Here, φ_α is a chosen localized function upon which the DOS is projected and the sum goes over all eigenstates. In our calculations ϕ_i and ϵ_i are the Kohn-Sham orbitals and eigenvalues. In the ground-state of a metal, the one-electron levels are occupied up to the Fermi level (with energy of E_{F}) [75].

4.1.1 Bulk Rhenium

Rhenium is a $5d$ transition metal of group VII and has a lustrous silvery white color. Its melting point (3180 °C) is the third highest among all elements [76]. The equilibrium crystal structure of Rhenium is hcp with two atoms in the primitive unit cell as shown in Fig. 4.1. The total number of electrons of a Re atom is 75 with a half full $5d$ shell. The lattice parameters at room temperature are a=2.76 Å and c/a=1.61 [77]. The cohesive energy (E_{coh}) at 0 K and 1 atm is –8.03 eV [77].

Method	a_0 (Å)	c_0 (Å)	B_0 (Mbar)	E_{coh} (eV)
USPP (PBE)	2.78	4.48	3.65	–7.63
USPP (LDA)	2.73	4.41	4.05	–9.45
AE (PBE)	2.78	4.48	3.63	–7.70
AE (LDA)	2.74	4.42	4.06	–9.59
Expt. [77]	2.76[1]	4.46[1]	3.72[1]	–8.03[2]

[1] at room temperature

[2] at 0 K and at 1 atm

Table 4.1: Calculated lattice parameters (a_0 and c_0), bulk modulus (B_0), and cohesive energy (E_{coh}) of bulk Re, determined with USPP and AE approaches using the PBE and LDA approximations, as well as comparison with experiment.

The cohesive energy of Re bulk was calculated from eq. (4.3). We first obtained $E_{\mathrm{tot}}^{\mathrm{atom}}$ by performing spin-polarized DFT calculations and using a fully non-symmetric 16 Å×17 Å×20 Å supercell with a single Re atom. The Brillouin zones of the unit cell were sampled with one **k**-point and a plane-wave basis set with an energy cutoff of 380 eV was used. Convergence tests (see Appendix A) showed that using this energy cutoff and Monkhorst–Pack **k**-point mesh of 8×8×5 for Re bulk yield converged results for both PBE and LDA. After calculating $E_{\mathrm{tot}}^{\mathrm{atom}}$, the following quantity was obtained versus V for several c/a ratios with the PBE and LDA functional (Fig. 4.2):

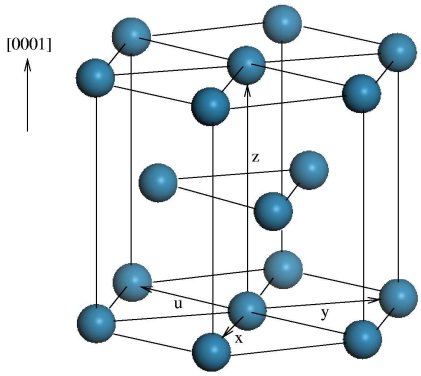

Figure 4.1: Three-dimensional unit cell for Re (hcp).

$$\Delta E(a,c) = \frac{E_{\mathrm{tot}}^{\mathrm{bulk}}(a,c) - N_{\mathrm{atom}} E_{\mathrm{tot}}^{\mathrm{atom}}}{N_{\mathrm{atom}}}. \tag{4.5}$$

It can be seen that a value of c/a=1.61 gives the minimum of $\Delta E(a,c)$ for both functionals. The equilibrium lattice constants (a_0 and c_0) and bulk modulus (B_0), as well as the cohesive energy ($\Delta E(a_0,c_0)$) were determined (at c/a=1.61) by using the Murnaghan equation of state. The results are given in Tab. 4.1, where the experimental values are listed for comparison. For checking the accuracy of the Re pseudopotential, these quantities were also calculated with a full-potential all-electron (AE) approach using the WIEN2K code [78]. Comparison between AE and ultrasoft pseudopotential (USPP) results shows no significant difference

in the calculated Re bulk properties considering both PBE and LDA. In the following we will discuss our results based on the ultrasoft pseudopotential method. The lattice constants of a_0 and c_0 with the GGA(PBE) calculations are about 0.7 and 0.5 % larger than the experimental value, while LDA underestimates these parameters by 1.1 %. The calculated bulk modulus using PBE is only 1.9 % lower than the experimental value, while the LDA result is 8.9 % larger. Therefore, similar to the DFT-GGA results of other transition metals such as Ag, Pd, Rh, and Cu [79–82], we found a slight overestimation of a_0 and an underestimation of B_0 compared to the corresponding experimental values. Furthermore, the cohesive energy determined by PBE is significantly smaller (1.82 eV) than the LDA value and better compares to experiments.

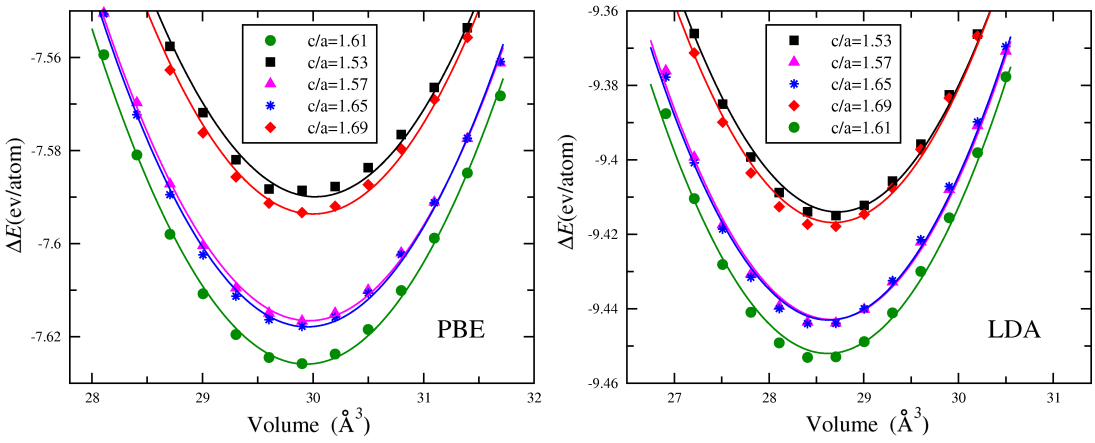

Figure 4.2: $\Delta E(a, c)$ versus volume for five different values of c/a, obtained on the basis of GGA (PBE) (left) and LDA (right) functionals.

4.1.2 Density of States for Re Bulk

For transition metals the d-bands are gradually filled up when moving from left to right of the corresponding series in the periodic table. Therefore, the position of the Fermi level in DOS plots reflects the number of electrons occupying the d-levels.
The calculated PDOSs of Re bulk are shown in Fig. 4.3. From this plot, the following information is obtained:

- the d-band has considerably larger contributions to the total valence DOS compared to s and p-orbitals;
- the d-band is narrower than free-electron-like s- and p-bands;

- the integral of the d-band up to the Fermi energy is almost equal to that above the Fermi energy. This reflects the fact that rhenium has a half-full d-band.

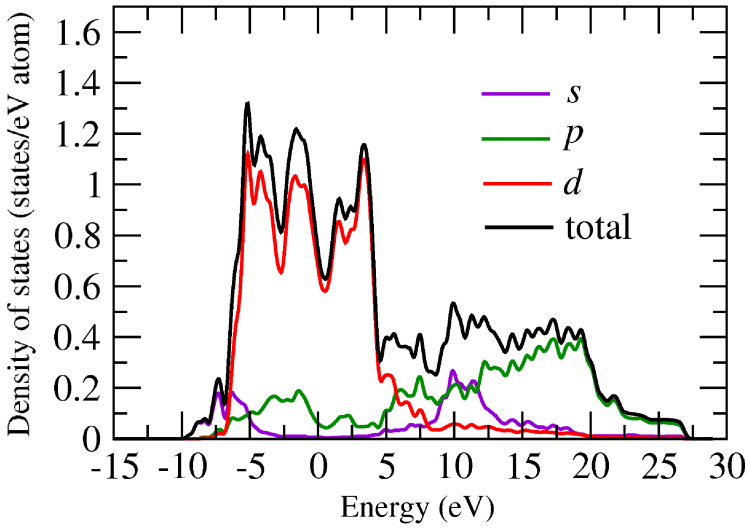

Figure 4.3: Partial density of states (projected onto s, p, and d-orbitals) and total density of states for rhenium bulk. The energy zero shows the Fermi level.

4.1.3 Bulk Rhenium Oxide

As discussed in Chapter 2, in our approach we consider oxygen adsorption on single-crystal surfaces, which are in thermodynamic equilibrium with two reservoirs: crystal bulk and an O_2 atmosphere. There is experimental evidence that under specific conditions (*i.e.*, gas exposure, temperature, and pressure conditions) bulk oxides are formed [83]. In this case, the surface is in equilibrium with the bulk oxide and our approach is not valid anymore. In order to determine the thermodynamic conditions under which transition from on-surface adsorption to bulk oxide formation occurs, we need to characterize the properties of the bulk oxide structures.
The thermodynamic condition for formation of a bulk rhenium oxide (Re_xO_y) with the Gibbs free energy per formula unit of $g^{\text{bulk}}_{\text{Re}_x\text{O}_y}$ is

$$g^{\text{bulk}}_{\text{Re}_x\text{O}_y} < x g^{\text{bulk}}_{\text{Re}} + y\mu^{\text{gas}}_{\text{O}}, \tag{4.6}$$

where $g^{\text{bulk}}_{\text{Re}}$ is the Gibbs free energy per Re atom of the rhenium bulk and $\mu^{\text{gas}}_{\text{O}}$ is the oxygen chemical potential. To obtain the (T, p)-dependent terms of $\mu^{\text{gas}}_{\text{O}}$ (see eq. (2.52)) we choose $\frac{1}{2}E^{\text{tot}}_{\text{O}_2}$ as reference

$$\Delta\mu_{\text{O}}(T,p) = \mu_{\text{O}}(T,p) - \frac{1}{2}E^{\text{tot}}_{\text{O}_2}. \tag{4.7}$$

Substituting eq. (4.7) into eq. (4.6) results in the following condition for the formation of Re_xO_y

$$\frac{1}{y}\left[g^{\text{bulk}}_{\text{Re}_x\text{O}_y} - x g^{\text{bulk}}_{\text{Re}} - \frac{y}{2}E^{\text{tot}}_{\text{O}_2}\right] < \Delta\mu_{\text{O}}, \tag{4.8}$$

where the term in the square bracket equals the heat of formation[2] of the bulk oxide at zero temperature $\Delta H_f(T = 0\,\text{K})$. The (T, p) dependence of the Gibbs free energies of pure bulk and bulk oxide (solid phases) is insignificant compared to that of the chemical potential of oxygen. Therefore the stability condition can be rewritten as

$$\frac{1}{y}\Delta H_f(T = 0\,\text{K}, p = 0\,\text{atm}) < \Delta\mu_{\text{O}}, \tag{4.9}$$

where $\Delta H_f(T = 0\,\text{K}, p = 0\,\text{atm})$ can be obtained from DFT calculations.
The most common Re-oxides include: (i) ReO_2, (ii) ReO_3, and (iii) Re_2O_7. Experimental studies show that ReO_2 is the only stable oxide phase at higher temperatures [84] and crystallizes to monoclinic (α-ReO_2) and orthorhombic (β-ReO_2) structures. The former system is stable only at $T \leq 573$ K and transforms into the latter at higher temperatures [85]. Fig. 4.4 shows the 3D view of the β-ReO_2 structure proposed from X-ray data [85]. This structure has the space group of *Pbcn*. We optimized the lattice parameters and internal coordinates of atoms for β-ReO_2 using the BFGS algorithm. The calculated properties of β-ReO_2 obtained with the PBE and LDA approximations as well as the corresponding experimental values are summarized in Tab. 4.2. Here, we focused on the lattice constants and the shortest bond lengths of Re–Re, O–O, and Re–O as well as the heat of formation. Both PBE and LDA calculations were performed using the converged Monkhorst-Pack grid of 5×4×5 **k**-points and an energy cutoff of 380 eV (see Appendix A). Compared to the experimental values, DFT-PBE overestimates a_0, b_0, and c_0 by 1.3, 0.5, and 0.2 %, while DFT-LDA underestimates these parameters by 0.6, 1.3, and 1.5 %. Not only the lattice constants but also the

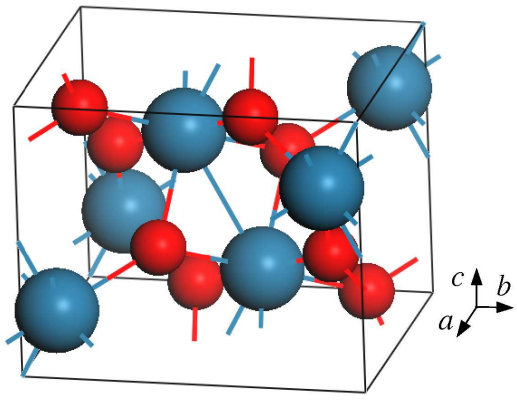

Figure 4.4: Structure model of β-ReO_2. The Re and O atoms are represented by blue and red spheres, respectively.

[2]Heat of formation is defined as the energy released during the formation of a compound from its constituents.

theoretical bond lengths calculated with both functionals are in good agreement with experiments. The heat of formation of 4.48 eV calculated using PBE agrees well with the measured values (4.613 [84] and 4.68 [86] eV), while this quantity is significantly overestimated by the LDA (5.90 eV). Therefore we expect that PBE provides a better description for the binding energies, while both PBE and LDA give reasonable results for bond lengths.

	a_0	b_0	c_0	$d_{\mathrm{Re-Re}}$	$d_{\mathrm{O-O}}$	$d_{\mathrm{Re-O}}$	ΔH_f
DFT-PBE	4.87	5.67	4.61	2.61	2.62	1.99	4.48
DFT-LDA	4.78	5.57	4.53	2.56	2.57	1.95	5.90
Experiment [85]	4.809[1]	5.643[1]	4.601[1]	2.61[1]	2.60[1]	1.95[1]	–
Experiment [84]	–	–	–	–	–	–	4.613±0.002[2]
Experiment [86]	–	–	–	–	–	–	4.68±0.04[2]

[1] at 293.15 K

[2] at 298.15 K

Table 4.2: Calculated properties of bulk β-ReO_2, determined with PBE and LDA, as well as comparison with experiment. The lattice constants a_0, b_0, c_0, the nearest distance between Rhenium atoms $d_{\mathrm{Re-Re}}$ and oxygen atoms $d_{\mathrm{O-O}}$, as well as the Re-O bond length $d_{\mathrm{Re-O}}$ are given in Å , while the heat of formation ΔH_f is in eV.

4.1.4 Bulk Rhenium Nitride

When a metal surface is in contact with a nitrogen atmosphere, bulk nitride might be formed under specific nitrogen gas-phase conditions. Similar to the bulk rhenium oxide, a bulk nitride structure (Re_xN_y) is stabilized when the nitrogen chemical potential $\Delta\mu_{\mathrm{N}}$ is larger than $\Delta H_f\,/y$, where ΔH_f is the heat of formation of bulk nitride per unit. There is experimental evidence that a stable Re-nitride cannot be obtained directly from the elements [87].

4.2 Properties of the Clean Surfaces

The hexagonally close-packed (hcp) structures such as adopted by metallic rhenium involve two interpenetrating Bravais lattices. In this kind of material, we have two classes of atoms, which are distinguishable in their environment. As can be seen from Fig. 4.1, the arrangement of atoms in the middle layer is different from that in the bottom and top layers. Therefore, in most cases cleaving the hcp crystal along a particular direction creates two different surface structures depending on which kind of atoms are exposed (by displacing dividing plane).

The four-index notation (*ijkl*) is usually used to denote a hcp surface plane. Each index indicates the intersection of the considered plane with the *x, y, u*, and *z* axes as represented in Fig. 4.1. Using this notation we label two different possible terminations of Re surfaces by (*ijkl*)A and (*ijkl*)B.
In the simplest assumption, which is called the *truncated* bulk or *ideal* model, the position of atoms after cleavage of any structure are exactly the same as in the bulk. In this model, effects due to the reduction of the coordination number of atoms at the surface is neglected. Usually two kinds of reconfigurations happen after creating a surface: *relaxations* and/or *reconstructions*. Relaxation, which occurs on most surfaces, involves changes in the separation between two layers in the surface with respect to the bulk truncated structure. One simple model to explain this effect was introduced by Finnis and Heine [88]. For the metal surface, they proposed a small contraction for the first layer separation (d_{12}) relative to the bulk termination. When a surface is formed by cleaving a crystal, the electrons have a tendency to distribute more uniformly and reduce their kinetic energy. This causes an inward electrostatic force on first layer ions, leading to a surface contraction. This effect is more significant for rather open surfaces. Although this model is most widely used to describe the top layer relaxation effect, some surfaces show a deviating behavior. For example, both DFT calculations and LEED analysis showed an expansion of d_{12} for Al(111) and Pt(111) [89].
On the other hand, reconstruction is referred to more pronounced changes in the geometry of a surface and can lead to the following changes in the surface structure of materials [75]:

1. Reducing the layer symmetry at a fixed layer atomic density. An example is the $c(2\times2)$ reconstruction of W(100) [90–93].

2. Changing both the layer symmetry and layer atomic density. Examples are hexagonal-reconstructions of fcc(100) surfaces of $5d$ metals (Ir, Pt, Au) [94].

3. Missing of atom-rows, leading to changes in the layer atomic density. An example is the (1×2)-missing-row (MR) reconstruction of the fcc(110) surface of $5d$ metals (Ir, Pt, Au) [95–101].

Reconstruction of transition metals is believed to be stabilized by the overlapping of d electrons, which leads to formation of local bonds [102].
Experimental and theoretical studies show that on most transition metal surfaces relaxation occurs, but reconstruction is observed quite rarely.
In some cases, missing-row reconstruction of a surface leads to the formation of well-ordered nanostructures composing of narrow facets. Here, the strong tendency towards stable microfacets and nanofacets seems to be the driving force for such surface reconstruction: An example is reconstruction of Ir(110) surface [103, 104]. Under specific conditions a massive reconstruction occurs and an initially planar surface converts to a "hill-and-valley" structure, exposing new

crystal faces of nanometer scale dimensions. This kind of faceting is driven by surface thermodynamics (anisotropy of surface free energy), but controlled by kinetics (diffusion and nucleation). Surfaces can spontaneously rearrange to minimize their total surface energy (by developing facets), even if this involves an increase in surface area. The spontaneous faceting of clean planar metal surfaces is not commonly observed, because the anisotropy in surface free energy is generally too small for a surface to form facets. However, when the surface is covered by gaseous or metallic impurities, the anisotropy in surface free energy can be enhanced considerably [23].

Motivated by experimentally observed facets on Re(11$\bar{2}$1), we focused on different surfaces that are involved in the facet formation. Figs 4.6–4.8 present 3D, top, and side views of the two different possible terminations of surfaces studied in the present work: Re(10$\bar{1}$0), Re(10$\bar{1}$1), Re(11$\bar{2}$1), and Re(13$\bar{4}$2). For more close-packed surfaces, (10$\bar{1}$0) and (10$\bar{1}$1), the probable missing-row reconstructed configurations, which have been observed on surfaces of $5d$ metals, are also considered.

While for the (10$\bar{1}$0), (10$\bar{1}$1), and (13$\bar{4}$2) surfaces of a hcp crystal the interlayer separations are alternatingly long and short, for the (11$\bar{2}$1) orientation, all layer distances are equal. As mentioned above, after a surface is created topmost atom layers are usually displaced in the direction normal to the plane. Here, the change in the separation of layers i and j (d_{ij}) due to relaxation is given by:

$$\Delta d_{ij} = \frac{(d_{ij} - d_{ij}^{\mathrm{bulk}})}{d_{ij}^{\mathrm{bulk}}} \times 100, \tag{4.10}$$

where d_{ij}^{bulk} is the corresponding bulk truncated value of d_{ij}. Note that a positive (negative) value of Δd_{ij} represents expansion (contraction) of the interlayer distance.

Low energy-electron diffraction (LEED) is a valuable experimental tool to study the surface structure of materials. LEED is a widely used method for analyzing the size and symmetry of the unit cell as well as interlayer distances. Among the Re surfaces discussed in this work, only clean Re(10$\bar{1}$0) and (11$\bar{2}$1) have been studied by LEED [23, 105]. We are also not aware of any previous theoretical studies on the clean Re surfaces.

In the next section, the energetics and geometries of different surfaces involved in facet formation of Re(11$\bar{2}$1) are discussed. The stabilities are evaluated with respect to the surface free energy (γ) defined in eq. (2.51) with $N_{\mathrm{ads}} = 0$. The calculated γ of the different structures are given in Tab. 4.3. All slab geometries were generated on the basis of the calculated lattice constants of a_0=2.78 Å and c_0=4.48 Å. All the results discussed in the following are based on the optimum parameters (see Appendix A): A plane-wave basis set with an energy cutoff of 380 eV was used for all surfaces. The Brillouin zones of the (1×1)-surface unit cells of Re(11$\bar{2}$1), (10$\bar{1}$0), (10$\bar{1}$1), and (13$\bar{4}$2) were sampled with (4×4), (5×8),

Structure	PBE	LDA
Re(11$\bar{2}$1)A	220	255
Re(11$\bar{2}$1)B	220	–
Re(10$\bar{1}$0)A	183	215
Re(10$\bar{1}$0)B	251	–
Re(10$\bar{1}$0)A-(1×2)	236	–
Re(10$\bar{1}$0)A-(1×3) single MR	216	–
Re(10$\bar{1}$0)A-(1×3) double MR	240	–
Re(10$\bar{1}$0)A-(1×3) triple MR	221	–
Re(10$\bar{1}$1)A	213	245
Re(10$\bar{1}$1)B	243	–
Re(10$\bar{1}$1)A-(1×2)	226	–
Re(13$\bar{4}$2)A	217	251
Re(13$\bar{4}$2)B	217	–
pyramids (Fig. 4.10 (a))	234	272
ridges (Fig. 4.10 (b))	225	261

Table 4.3: Surface free energies (in meV/Å^2) for Re surfaces obtained using the PBE and LDA functional.

(4×8), and (3×3) Monkhorst–Pack **k**-point meshes. These surfaces were represented by 19-layer, 11-layer, 14-layer, and 30-layer slabs, respectively, separated by at least 13 Å vacuum. For Re(11$\bar{2}$1), (10$\bar{1}$0), and (10$\bar{1}$1), the bottom four layers and, for (13$\bar{4}$2), the bottom fourteen layers were fixed at the calculated bulk structure, and the geometry of the remaining layers was fully optimized.

4.2.1 Re(11$\bar{2}$1)

Experimentally, no reconstruction has been observed on clean Re(11$\bar{2}$1) [23]. LEED studies on clean Ru(11$\bar{2}$1) [106] also showed the same behavior of an unreconstructed surface.
It can be seen from Fig. 4.5 that Re(11$\bar{2}$1)A and Re(11$\bar{2}$1)B are mirror symmetric of each other and have the same surface termination. Therefore, we continue our calculations focusing on Re(11$\bar{2}$1)A only. As expected, the calculated surface free energy for Re(11$\bar{2}$1)A is larger with LDA than with PBE (see Tab. 4.3). Our PBE calculation shows that the outermost layers are strongly contracted (Δd_{12}=–14.8 %, Δd_{23}=–20.6 %, and Δd_{34}=–15.7 %). These contractions are compensated by a very large expansion in the fourth interlayer separation (28.4 %).

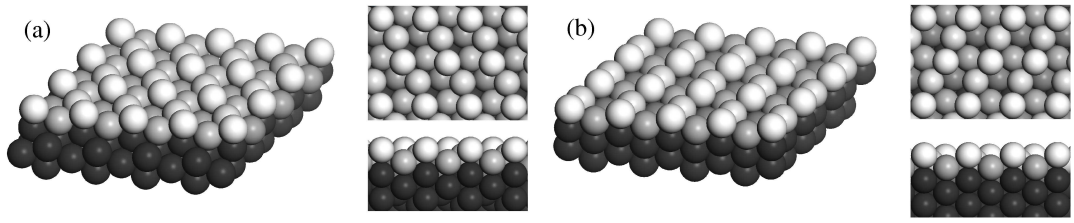

Figure 4.5: 3D, top, and side views of (a) Re(11$\bar{2}$1)A-(1×1) and (b) Re(11$\bar{2}$1)B-(1×1). The layers become darker with increasing depth.

4.2.2 Re(10$\bar{1}$0)/Re(01$\bar{1}$0)

The LEED patterns of clean Re(10$\bar{1}$0) show an unreconstructed (1×1) structure [105, 107]. On the other hand, as we had already discussed in Section 3.1, different experiments indicated that the O/Re(10$\bar{1}$0) structure has a (1×3) periodicity [63, 64].
The different surface structures considered for clean Re(10$\bar{1}$0) are shown in Fig. 4.6. Besides the unreconstructed surfaces (Fig. 4.6(a) and (b)), we also studied reconstructed Re(10$\bar{1}$0)A-(1×2) (Fig. 4.6(c)). This type of reconstruction is observed on several $5d$ fcc(110) metals (see previous section). Since the experimentally found (1×3) periodicity for O/Re(10$\bar{1}$0) could also be due to a corresponding reconstruction of the surface, we also studied three differently reconstructed Re(10$\bar{1}$0)A-(1×3) surfaces shown in Fig. 4.6(d)–(f): (i) every third top-layer row was removed, (ii) every second and third top-layer rows were removed, and (iii) every second and third top-layer rows as well as the second-layer row in the center of each trough were removed. Interestingly, structure (iii) can be viewed as {10$\bar{1}$1} microfacets at the (10$\bar{1}$0) surface. In the following these structures are denoted as single, double, and triple MR (missing-row).
The calculated surface free energies for the clean surfaces are listed in Tab. 4.3. Regarding the unreconstructed surface we find that Re(10$\bar{1}$0)A, which is more closely-packed than Re(10$\bar{1}$0)B, is more stable by 68 meV/Å^2. This observation is in agreement with experiment [105]. DFT calculations with the LDA functional for Re(10$\bar{1}$0)A give a surface free energy of 215 meV/Å^2, which is 32 meV/Å^2 higher than the PBE value. As we had mentioned in Section 2.4.4, in general, cohesive energy is larger with the LDA than the GGA and thus higher free energy is expected for surfaces with the former functional.
According to our PBE calculation, the separation between the outermost layers of Re(10$\bar{1}$0)A is contracted by –16.1 % (compared to the bulk layer spacing). This is also in good agreement with the experimental value of Δd_{12}=–17 % from the LEED data by Davis *et al.* [105]. They also proposed that the separation between the second and third layer may be expanded by 1–2 %. However there still remains uncertainty on this conclusion. Our calculations show an insignificant

contraction of 0.1% for d_{23}.
It can be seen from Tab. 4.3 that clean unreconstructed Re(10$\bar{1}$0)A-(1×1) is considerably more stable than all reconstructed surfaces. Thus, our results indicate no preference for such kind of reconstruction of clean Re(10$\bar{1}$0). As we mentioned above, the experimental studies also demonstrated that clean Re(10$\bar{1}$0) has an unreconstructed structure, which is in line with the results for other $3d$ and $4d$ hcp(10$\bar{1}$0) metal surfaces [108, 109].

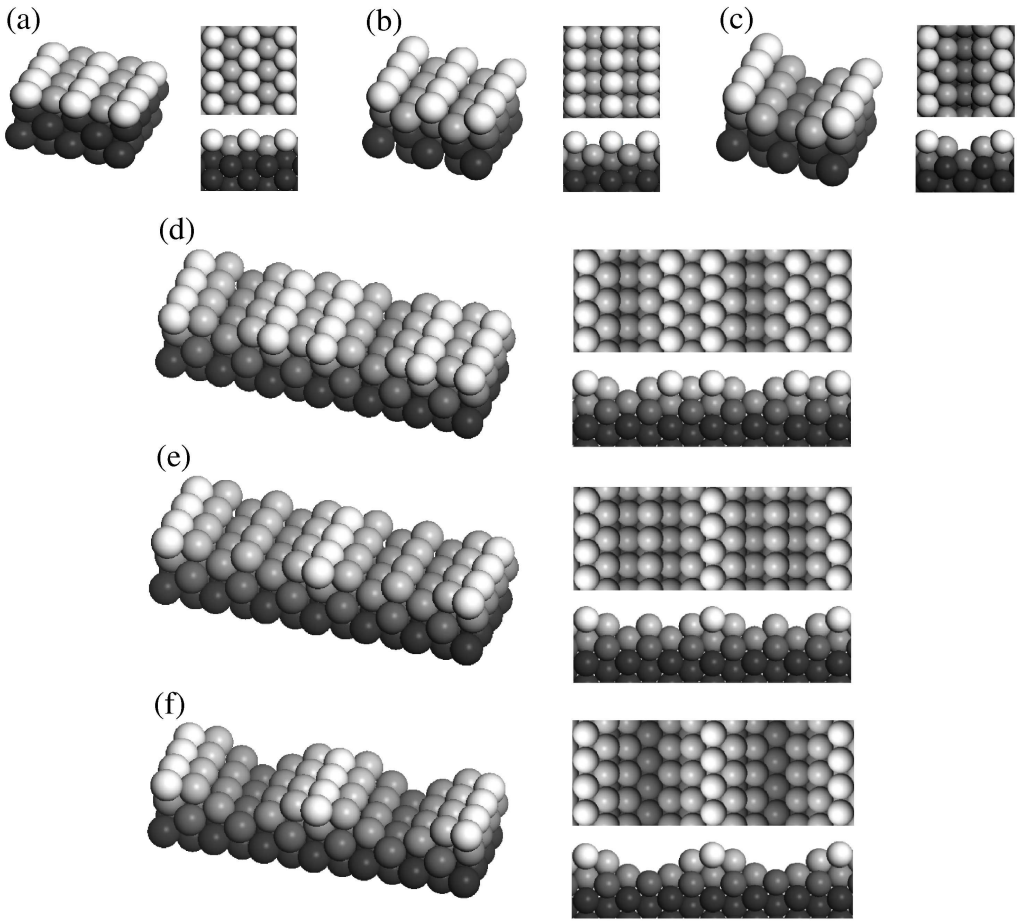

Figure 4.6: 3D, top, and side views of (a) Re(10$\bar{1}$0)A-(1×1), (b) Re(10$\bar{1}$0)B-(1×1), (c) Re(10$\bar{1}$0)A-(1×2), (d) Re(10$\bar{1}$0)A-(1×3) single missing-row, (e) Re(10$\bar{1}$0)A-(1×3) double missing-row, and (f) Re(10$\bar{1}$0)A-(1×3) triple missing-row surfaces. The layers become darker with increasing depth.

4.2.3 Re(10$\bar{1}$1)/Re(01$\bar{1}$1)

A (1×2) reconstruction of the missing-row type (see Section 3.1) has been proposed by Wang [7] for the O/Re(10$\bar{1}$1) facets, which are formed on oxygen-covered

Re(11$\bar{2}$1). To determine whether Re(10$\bar{1}$1) reconstructs in its clean state we considered Re(10$\bar{1}$1)-(1×2) in addition to two different configurations of Re(10$\bar{1}$1)-(1×1) (see Fig 4.7).
The surface corrugation of Re(10$\bar{1}$1)A-(1×1) is smaller than that of Re(10$\bar{1}$1)B-(1×1). Therefore, the surface free energy of the former (213 meV/Å^2) turned out to be 30 meV/Å^2 lower. Using the LDA exchange–correlation functional gives a surface free energy of 245 meV/Å^2 for Re(10$\bar{1}$1)A-(1×1), which is again higher than the PBE value.
Regarding the surface structure of unreconstructed Re(10$\bar{1}$1)A, we calculated (using the PBE functional) a relatively strong contraction of the outermost layer separation (Δd_{12}=–9.8 %). In addition, a small contraction of 1.8 % was obtained for Δd_{23}. Unfortunately, there is no experimental data on the clean Re(10$\bar{1}$1) surfaces to make comparison with our results.
DFT-PBE calculations yield a surface free energy of 226 meV/Å^2 for the (1×2)-MR structure, which is only 13 meV/Å^2 larger than the value obtained for the corresponding unreconstructed structure.

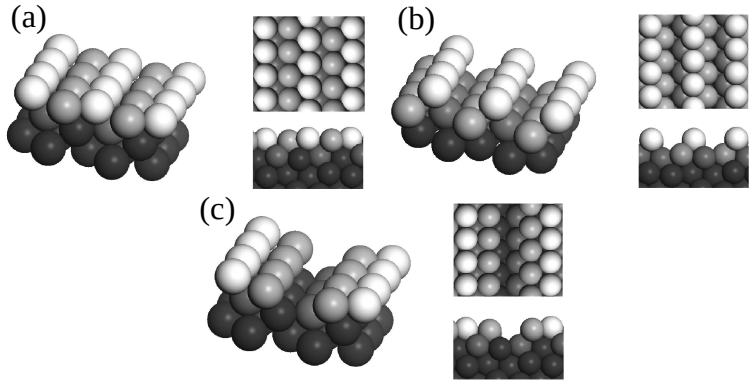

Figure 4.7: 3D, top, and side views of (a) Re(10$\bar{1}$1)A-(1×1), (b) Re(10$\bar{1}$1)B-(1×1), and (c) Re(10$\bar{1}$1)A-(1×2). The layers become darker with increasing depth.

4.2.4 Re(13$\bar{4}$2)/Re(31$\bar{4}$2)

Two configurations of this surface orientation are very open and have eight layers of atoms exposed. It was found that with the PBE functional both configurations have the same surface free energy of 217 meV/Å^2. Interestingly, this value is slightly lower than that obtained for Re(11$\bar{2}$1). The Re(13$\bar{4}$2) surface is much more open than Re(11$\bar{2}$1) and one might expect the former structure to be less stable. This result is probably due to the unique structure of Re(13$\bar{4}$2): The (13$\bar{4}$2) surface is a vicinal (01$\bar{1}$1) surface with kinked steps and (01$\bar{1}$1) terraces that are more close-packed than (11$\bar{2}$1) [7]. This picture is also supported by our

DFT results (see Tab. 4.3), which show that the surface free energy of Re(13$\bar{4}$2) is only slightly higher than that of Re(01$\bar{1}$1).
With the LDA functional the calculated γ for Re(13$\bar{4}$2)A is 34 meV/Å^2 larger than the corresponding PBE value. The changes in the interlayer spacings are Δd_{12}=–31.2 %, Δd_{23}=–4.4 %, Δd_{34}=–35.6 %, and Δd_{45}=13.2 %. Unfortunately, again there is no experimental data on this surface to compare our values with.

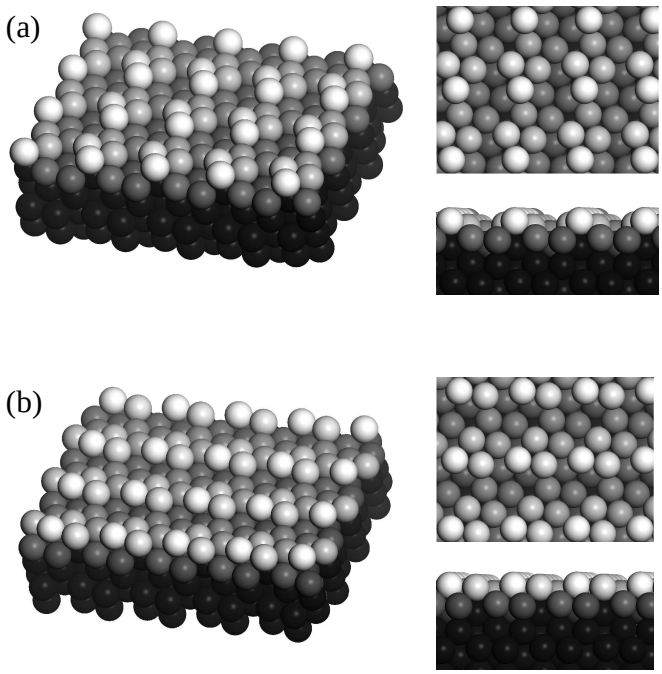

Figure 4.8: 3D, top, and side views of (a) Re(13$\bar{4}$2)A-(1×1) and (b) Re(13$\bar{4}$2)B-(1×1). The layers become darker with increasing depth.

4.2.5 Density of States for Re Surfaces

In Fig. 4.9 we show the density of states projected onto the d orbitals (d-PDOS)[3] of the topmost surface atoms of Re(10$\bar{1}$0), (10$\bar{1}$1), (11$\bar{2}$1), and (13$\bar{4}$2), calculated with the PBE functional. According to a simple tight-binding model, the band width decreases with decrease in the coordination number of the atoms at the surface. Therefore, as can be seen in Fig. 4.9, the d-band of the topmost surface atoms is narrower compared to that of the bulk atoms. This narrowing of the d orbital is more pronounced for more open surafces of Re(11$\bar{2}$1) and (13$\bar{4}$2).

[3]In Section 4.1.2 we have seen that DOS of Re system is comprised mainly of d-states.

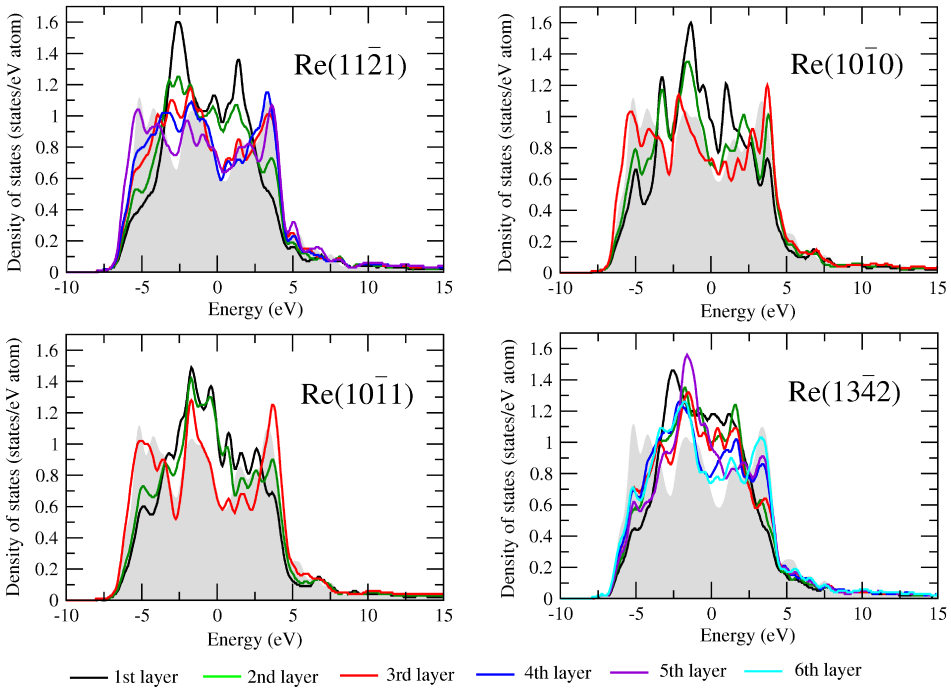

Figure 4.9: Partial density of states projected onto the d orbitals for different Re surfaces. The grey shaded area corresponds to the the d-states of a rhenium bulk. The energy zero shows the Fermi level.

4.2.6 Clean Rhenium Facets

The experimentally observed adsorbate-induced facets on Re(11$\bar{2}$1) (Fig. 4.10) are thermodynamically stable in the clean state if the surface free energies of the substrate as well as those of the faces after facet formation fulfill the condition of eq. (2.64). The facet tilt angles (ϑ_f) and partial contributions to each nano-shaped structure (S_f), given in Tab. 4.4, were used to obtain the overall γ of four-sided pyramids and two-sided ridges listed in Tab. 4.3. Both ϑ_f and S_f can be measured experimentally or derived geometrically (assuming bulk-truncated unrelaxed pyramids). The ϑ^{exp} values are not listed in Tab. 4.4 because of the experimental difficulties to determine this parameter [110]. The calculations show that clean planar Re(11$\bar{2}$1) is more stable than two-sided ridge-like structures and nanopyramids by 5 and 14 meV/Å^2. As already mentioned in Chapter 2, since the facets were observed

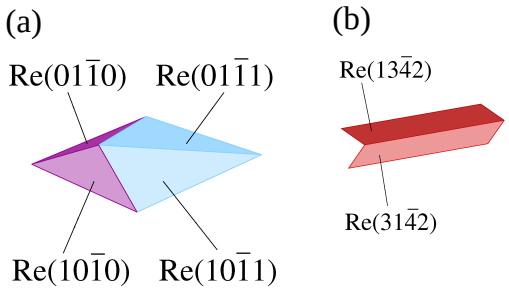

Figure 4.10: Schematic illustration of (a) four-sided pyramids and (b) two-sided ridges.

to be rather extended we neglect the presence of edges and kinks, which act as destabilization. Since these contributions are only relevant for the faceted surfaces, we would predict that two-sided ridge-like structures and nanopyramids are even less stable and the most stable clean surface to be most likely planar. This is also in agreement with experiment observations, finding planar Re($11\bar{2}1$) without adsorption of an adsorbate. Using the LDA functional, the two-sided ridge-like structures and nanopyramids are 6 and 17 meV/Å^2 less favorable than the planar Re($11\bar{2}1$) surface. Therefore, we can conclude that these results are not influenced by including the gradient corrections to LDA as it is the case for the PBE functional.

Surface	A [Å^2]	S^{exp}	S^{geo}	ϑ^{geo} [°]
Re($11\bar{2}1$)	22.54	–	–	–
Re($10\bar{1}0$)/($01\bar{1}0$)	12.43	0.44±0.02	0.456	34.18
Re($10\bar{1}1$)/($01\bar{1}1$)	14.11	0.56±0.02	0.544	29.68
Re($13\bar{4}2$)/($31\bar{4}2$)	46.77	1.0	1.0	15.42

Table 4.4: Surface area A (per 1×1-unit cell (calculated)), partial surface contributions (S), and tilt angles (ϑ) for the initial substrate and two types of nano-facets: two-sided ridges consisting of ($13\bar{4}2$) and ($31\bar{4}2$) faces and four-sided pyramids consisting of ($10\bar{1}0$), ($01\bar{1}0$), ($10\bar{1}1$), and ($01\bar{1}1$) faces. For S the experimentally measured and geometrically derived values are given [111].

Chapter 5

Oxygen and Nitrogen-covered Re Surfaces

In this chapter we discuss the oxygen and nitrogen-covered surfaces of Re(11$\bar{2}$1) as well as those of Re(10$\bar{1}$0), (10$\bar{1}$1), and (13$\bar{4}$2) which constitute the four-sided pyramidal and two-sided ridge-like facets (see Fig. 4.10) formed after the faceting. The energetics for different overlayers and coverages on these surfaces are studied to gain insights into the stability of the adsorbate structures as a function of coverage.

In our calculations, we used geometrical coverages Θ in GML, which are defined as the number of adsorbate atoms per (1×1) substrate atom unit cell, thus varying with surface orientation. For reconstructed surfaces, we also define Θ as the number of adsorbate atoms per (1×1)-unit cell of the corresponding unreconstructed surface. In comparison, experiments usually use physical coverages (PML), where surface saturation is achieved with 1 ML. Unfortunately, there are no direct measurements of saturation coverages on Re surfaces studied in the present work. However, in Section 6.2 we estimate relations between geometrical and physical monolayers.

For the close-packed surfaces Re(10$\bar{1}$0), (10$\bar{1}$1), and (11$\bar{2}$1) coverages smaller than 1 GML were studied, while for the Re(13$\bar{4}$2) surface orientation, which has rather extended surface unit cells, we only investigated coverages larger than 1 GML, since interactions between adsorbates in adjacent unit cells are expected in this case to be negligible. For systems with more than one adsorbate per (1×1)-unit cell, several combinations of adsorption sites have been studied. These configurations have been chosen by considering the calculated energies for lower coverages, and then trying to find the lowest destabilization due to adsorbate–adsorbate repulsion at higher coverages. All structures studied in this work are relaxed with no surface symmetry constraints in order to find the lowest energy configuration. The binding energies for all investigated oxygen or nitrogen adlayer configurations on Re surfaces are reported in Tabs. B.1–B.24 (see Appendix B).

In addition, for each surface we used the calculated binding energies of oxygen or nitrogen at the various surface sites together with a cubic spline interpolation to construct the full potential energy surfaces (PES). These PESs allow us to gain insights into the trends of adsorbate diffusion.
The most stable structure at a given coverage of an adsorbate on a surface (here assumed to be oxygen on the Re surface) is the one with the largest average binding energy as defined by

$$E_{\mathrm{bind}} = -\frac{1}{N_{\mathrm{O}}}\left[E_{\mathrm{O/Re-slab}} - E_{\mathrm{Re-slab}} - N_{\mathrm{O}}\left(\frac{1}{2}E_{\mathrm{O_2}}\right)\right], \tag{5.1}$$

where N_{O} is the number of oxygen atoms in the considered unit cell, $E_{\mathrm{O/Re-slab}}$, $E_{\mathrm{Re-slab}}$, and $E_{\mathrm{O_2}}$ are the total energies of the oxygen-covered Re surface slab, the clean Re surface slab, and the isolated oxygen molecule. According to this definition a positive number indicates that the dissociative adsorption of oxygen from gas-phase O_2 is exothermic. In this chapter, we only show tables that present the binding energies of O and N on the most stable structures.
Here, the notation $\bar{E}_{\mathrm{bind}}$ is used to denote the averaged E_{bind} value of combinations of single-adsorbate systems

$$\bar{E}_{\mathrm{bind}} = \frac{1}{N_{\mathrm{O}}}\sum_{i=1}^{N_{\mathrm{O}}} E^{i}_{\mathrm{bind}}(\Theta = 1\,\mathrm{GML}). \tag{5.2}$$

From this value we can roughly estimate the adsorbate–adsorbate interaction energy by evaluating $\bar{E}_{\mathrm{bind}} - E_{\mathrm{bind}}$.
In addition, it is interesting to study the differences in the density of states for different adsorbate-covered surfaces. This is the aim of Section 5.5 of this chapter, within which we will compare qualitatively the strength of O or N binding on Re(11$\bar{2}$1), (10$\bar{1}$0), (10$\bar{1}$1), and (13$\bar{4}$2).

5.1 Re(11$\bar{2}$1)

As we had already discussed in Sections 3.1 and 3.2, Re(11$\bar{2}$1) is the substrate orientation onto which faceting occurs after adsorption of strongly interacting adsorbates (oxygen or nitrogen). Therefore, before investigating the faces of the different experimentally observed facets, we will discuss the adsorption of oxygen and nitrogen on Re(11$\bar{2}$1)[1]. This will also allow us to clearly compare the changes in surface stability introduced by the adsorbates, that finally lead to the observed morphology changes. Fig. 5.1 displays thirteen probable

[1] In Chapter 4 we have seen that Re(11$\bar{2}$1)A and Re(11$\bar{2}$1)B have the same stability. Therefore, here we continue our studies by considering one of these configurations (Re(11$\bar{2}$1)A) and for simplicity we refer to it as Re(11$\bar{2}$1).

binding sites that were considered in the present work. We studied the atomic adsorption of oxygen and nitrogen for coverages of 0.5, having either (1×2) or (2×1) periodicity, as well as 1.0, 2.0, and 3.0 GML with (1×1) periodicity. Figs. 5.2 and 5.4 present the most stable configurations, for which the binding energies are summarized in Tabs. 5.1 and 5.2. All adsorption energies reported here are calculated by eq. (5.1) (referenced to half a gas-phase adsorbate molecule).

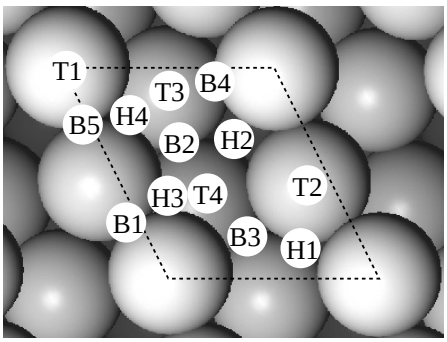

Figure 5.1: Top view of Re(11$\bar{2}$1) showing all binding sites at which O and N adsorption has been studied.

5.1.1 O/Re(11$\bar{2}$1)

For coverages of 0.5 and 1.0 GML, oxygen prefers binding at two-fold bridge sites (B5). The calculated binding energies for these structures are very similar (0.5 GML: 3.82 eV in the (1×2)-1O adlayer and 3.81 eV in the (2×1)-1O adlayer, 1.0 GML: 3.85 eV) and since Re(11$\bar{2}$1) is a rather open surface there are still only weak adatom interactions. The PES for the system with a single oxygen atom per (1×1)-unit cell (Fig. 5.3) makes apparent that the adsorption sites on the zig-zag rows are significantly more stable than those in the trough. In addition, we find that while an energy barrier of ∼0.7 eV is connected with adatom diffusion along the zig-zag rows (path (a)), there is a very high barrier of ∼1.4 eV for inter-row diffusion (path (b)).

coverage (GML)		E_{bind} (eV)
0.5	Fig. 5.2(1a)	3.82
	Fig. 5.2(1b)	3.81
1.0		3.85
2.0		3.48
3.0		2.98

Table 5.1: Binding energies (referenced to $^1/_2\,O_2$) for oxygen on Re(11$\bar{2}$1) at different coverages; only the most stable structure for each coverage is listed.

When the coverage is increased to 2.0 GML, O–O interactions become more pronounced. For the most stable structure (Fig. 5.2(3)) the binding energy is 3.48 eV, which is 0.19 eV smaller than the $\bar{E}_{\mathrm{bind}}$ value (see eq. (5.2)), approximating the model system without O–O repulsion. At 3.0 GML, as a consequence of repulsion between adsorbates, the third added O atom per unit cell is moved into the H3-position that was an unstable binding site at 1.0 GML.

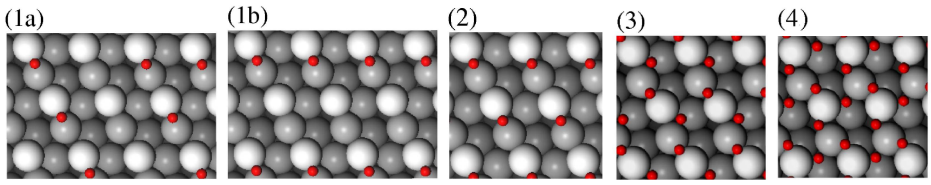

Figure 5.2: Top views of the most stable structures of oxygen-covered Re(11$\bar{2}$1) with different overlayers and coverages: (1a) (1×2)- and (1b) (2×1)-1O overlayer at 0.5 GML, (2) (1×1)-1O overlayer at 1.0 GML, (3) (1×1)-2O overlayer at 2.0 GML, (4) (1×1)-3O overlayer at 3.0 GML.

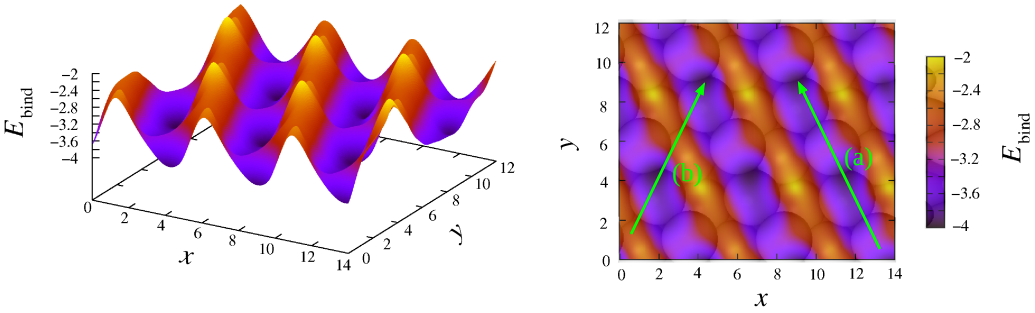

Figure 5.3: Adsorption energy distribution (in eV and referenced to $^1/_2\,O_2$) for binding 1 GML of atomic oxygen onto Re(11$\bar{2}$1). X and y are given in Å. The arrows indicate different paths for O diffusion on the surface.

5.1.2 N/Re(11$\bar{2}$1)

coverage (GML)		E_{bind} (eV)
0.5	Fig. 5.4(1a)	1.68
	Fig. 5.4(1b)	1.83
1.0		1.66
2.0		1.21
3.0		0.81

Table 5.2: Binding energies (referenced to $^1/_2\,N_2$) for nitrogen on Re(11$\bar{2}$1) at different coverages; only the most stable structure for each coverage is listed.

The most favorable adsorption site for N at 0.5 and 1.0 GML is not the same as for O adsorbate and found to be the H4-site, where adsorbates bind to one top-layer, the nearby second-layer, and third-layer Re atoms finally resulting in a three-fold binding. Although one might expect that similar to O adsorbate the binding energy of N will not change when going from 0.5 to 1.0 GML, our calculations reveal a different behavior: the binding energy is higher for 0.5 GML (Fig. 5.4(1b)) than for 1.0 GML (Fig. 5.4(2)) by 0.18 eV. At 0.5 GML, (2×1)-1N is more favorable than (1×2)-1N adlayer by 0.15 eV, while in case of O we found a very similar energy for these structures. After comparing the geometry of these structures with that of the clean surface, we observed an interesting effect. In the (2×1)-1N structure, some Re atoms on the zig-zag ridges

(connected by arrows in Fig. 5.4(1b)), which are not bound to the adatom, reduce their interatomic distance significantly by $\sim$0.13Å. This behavior, which will be discussed for Re(10$\bar{1}$0), Re(10$\bar{1}$1), Ir(311), and Ir(110) surfaces and which seems to be more general for the late 5*d* elements, is known as *row-pairing*. On Re(11$\bar{2}$1) lower binding energies are obtained for the (1×1)-1N and (1×2)-1N adlayers in which the row-pairing is absent. In case of O, this effect is insignificant in (2×1)-1O and thus the increase in adsorption energy on forming this configuration is not observed.

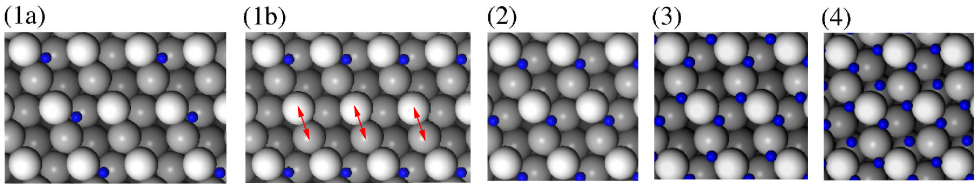

Figure 5.4: Top views of the most stable structures of nitrogen-covered Re(11$\bar{2}$1) with different overlayers and coverages: (1a) (1×2)-1N and (1b) (2×1)-1N overlayer at 0.5 GML, (2) (1×1)-1N overlayer at 1.0 GML, (3) (1×1)-2N overlayer at 2.0 GML, (4) (1×1)-3N overlayer at 3.0 GML. The arrows indicate the Re atoms that move toward each other upon relaxation.

The PES in Fig. 5.5 shows that the largest energy barrier for diffusion along the –H4–B3–B5–H4– direction (path (a)) is $\sim$0.8 eV. In addition, unlike the oxygen adsorbate, diffusion of nitrogen along the zig-zag rows (path (b)) is hindered by a very high barrier ($\sim$1.6 eV).
At 2.0 GML, occupation of H4-sites is still preferred, while the second atom binds at three-fold H1-sites (see Fig. 5.4(3)). Increasing the nitrogen coverage to 3.0 GML, we find the most stable structure (Fig. 5.4(4)) to be similar to the one obtained for 2.0 GML with the third N atom at T4, which again was an unstable site for N at lower coverages.

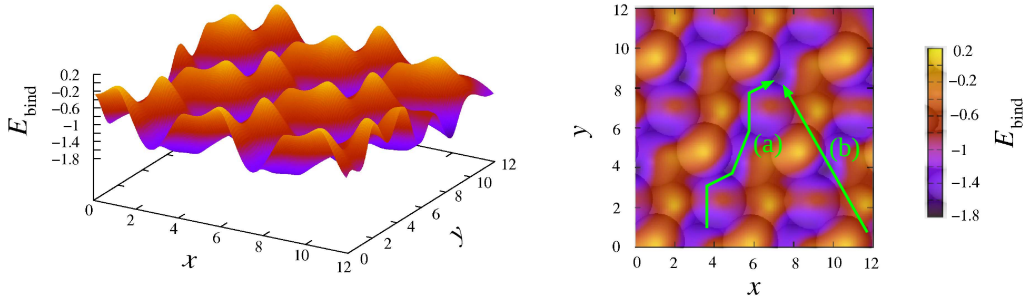

Figure 5.5: Adsorption energy distribution (in eV and referenced to $^1/_2\,N_2$) for binding 1.0 GML of atomic nitrogen onto Re(11$\bar{2}$1). *X* and *y* are given in Å. The arrows indicate different paths for N diffusion on the surface.

We will briefly compare the binding energies versus coverages for N with O adsorption on Re(11$\bar{2}$1). As Fig. 5.6 shows, at 1.0 GML, there is a difference in the absolute adsorption energy decrease compared to 0.5 GML in the two systems, which originates from the row-pairing effect as discussed above. In addition, a rather similar decrease in the binding energy is observed for O and N in the range 1.0 GML $\leq \Theta \leq$ 3.0 GML. This is due to the fact that adsorbate–adsorbate repulsions for O and N seem to be qualitatively similar at these coverages.

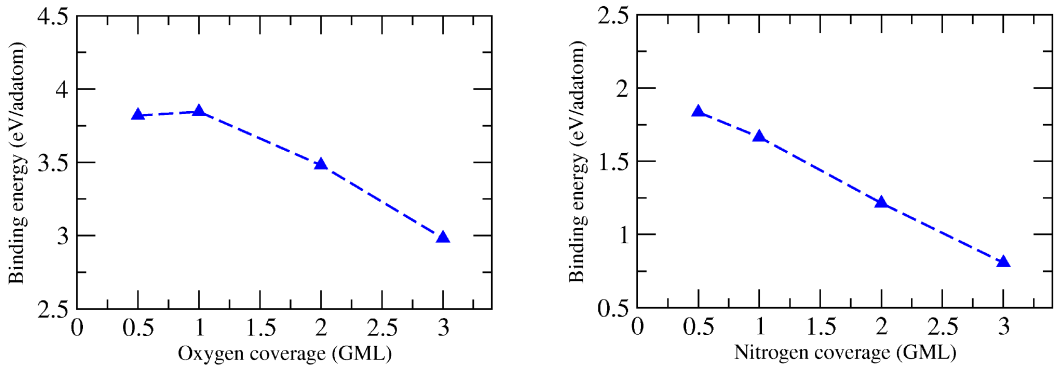

Figure 5.6: Binding energy (referenced to $^1/_2\,O_2$ and $^1/_2\,N_2$) as a function of oxygen (left) and nitrogen (right) coverage on Re(11$\bar{2}$1).

5.2 Re(10$\bar{1}$0)

As mentioned in Section 3.1, annealing O-covered Re(11$\bar{2}$1) generates nanoscale pyramids with {10$\bar{1}$0} and {10$\bar{1}$1} facet orientations. Here, we focus on the details of the atomic oxygen and nitrogen adsorption on Re(10$\bar{1}$0).[2]
Despite the similarities between hcp(10$\bar{1}$0) and fcc(110) surfaces, the former orientation has been studied to a much lesser extent. On the Re(10$\bar{1}$0) surface only few experimental studies have been performed [63, 64], while so far no first-principles calculation on this structure has been reported. Experimental studies on O/Re(10$\bar{1}$0) (see Section 3.1) agree that a (1×3) structure is formed upon oxygen adsorption on Re(10$\bar{1}$0). Since the experimentally found (1×3) periodicity could also be due to the oxygen-induced (1×3) reconstruction of the Re(10$\bar{1}$0) surface, we studied O adsorption on Re(10$\bar{1}$0)-(1×3), besides Re(10$\bar{1}$0)-(1×1). In addition, reconstructed Re(10$\bar{1}$0)-(1×2) was considered for comparison as well. We focused on the following coverages, which were defined with respect to the unreconstructed Re(10$\bar{1}$0)-(1×1) surface area:

[2] In Chapter 4 we have seen that Re(10$\bar{1}$0)A is more stable than Re(10$\bar{1}$0)B. Therefore, here we continue our studies by considering the former structure and for simplicity we refer to it as Re(10$\bar{1}$0).

- Θ=0.25, 0.33, 0.50, 0.66, 1.00, 1.33, 1.66, and 2.00 GML on O/Re(10$\bar{1}$0)-(1×1);
- Θ=0.50, 1.00, 1.50, and 2.00 GML on O/Re(10$\bar{1}$0)-(1×2);
- Θ=0.33, 0.66, 1.00, 1.33, 1.66, and 2.00 GML on O/Re(10$\bar{1}$0)-(1×3).

For nitrogen adsorption we considered the unreconstructed N/Re(10$\bar{1}$0)-(1×1) surface for different coverages.

5.2.1 Unreconstructed O/Re(10$\bar{1}$0)-(1×1)

In order to determine the preferred binding sites for oxygen adatoms on this surface, we started our calculations considering one adsorbate per (1×1)-unit cell. Fig. 5.7 shows several different binding sites at which oxygen binding has been studied. To check if the favorable adsorption site is changed with coverage we additionally evaluated the energies of adsorbates in these binding sites at 0.50 and 0.25 GML. These results show that the preferred binding site for O is a three-fold hcp H1-site (see Fig. 5.7), where adatoms are bound to two top Re atoms and to one Re atom in the second layer. Such adsorption site was also found for O on Co(10$\bar{1}$0) from LEED analysis [108] and on Ru(10$\bar{1}$0) by DFT calculations [109].

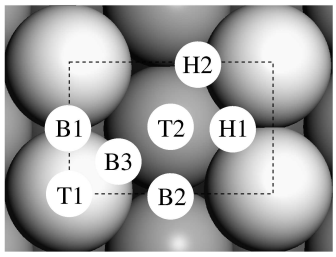

Figure 5.7: Top view of Re(10$\bar{1}$0) showing all binding sites at which O and N adsorption has been studied.

The structures of the overlayers considered for different coverages of O at the H1-site are presented in Fig. 5.8, for which the binding energies are summarized in Tab. 5.3. Reducing the coverage to 0.25 GML, we focused on the (2×2)-1O and c(2×4)-1O overlayers as shown in Figs. 5.8(1a) and (1b). In this case only weak lateral adatom interactions can be expected. The binding energies of 3.76 and 3.75 eV we calculated for the (2×2)-1O and c(2×4)-1O oxygen adlayers at the H1 sites are thus taken to represent the zero coverage limit.
Considering a coverage of 0.33 GML, besides (1×3)-1O (Fig. 5.8(2a)), we have checked a (3×1)-1O overlayer (Fig. 5.8(2b)). It turns out that the latter configuration, with a binding energy of 3.66 eV, is 0.07 eV more stable than the former. This preference might be explained by one of the following reasons: (i) the strong O–O repulsion along each substrate row or (ii) the tendency of O atoms to not share Re atoms along each substrate row.

structure	coverage (GML)	E_{bind} (eV)
(2×2)-1O	0.25	3.76
c(2×4)-1O	0.25	3.75
(1×3)-1O	0.33	3.59
(3×1)-1O	0.33	3.66
(2×1)-1O	0.50	3.73
(1×2)-1O	0.50	3.60
c(2×2)-1O	0.50	3.77
c(2×4)-2O	0.50	3.79
(1×3)-2O	0.66	3.60
(3×1)a-2O	0.66	3.61
(3×1)b-2O	0.66	3.57
(1×1)-1O	1.00	3.60
(2×1)$p2mg$-2O	1.00	3.41
(1×3)-4O	1.33	3.28
(1×2)-3O	1.50	3.17
(1×3)-5O	1.66	3.01
(1×1)-2O	2.00	2.76

Table 5.3: Binding energies (referenced to $^1/_2\,O_2$) for oxygen adsorbed at three-fold hollow H1-sites of the unreconstructed Re(10$\bar{1}$0)-(1×1) surfaces with different overlayers and coverages.

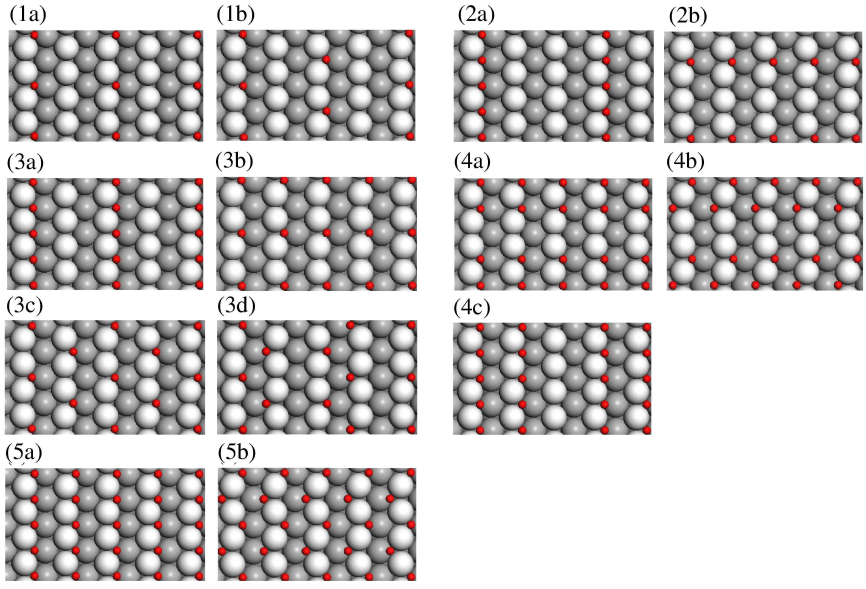

Figure 5.8: Top views of studied O/Re(10$\bar{1}$0) configurations for different coverages: (1a) (2×2)- and (1b) c(2×4)-1O at 0.25 GML, (2a) (1×3)- and (2b) (3×1)-1O at 0.33 GML, (3a) (1×2)-, (3b) (2×1)-, (3c) c(2×2)-1O, and (3d) c(2×4)-2O at 0.50 GML, (4a) (3×1)a-, (4b) (3×1)b-, and (4c) (1×3)-2O at 0.66 GML, (5a) (1×1)-1O and (5b) (2×1)$p2mg$-2O at 1 GML.

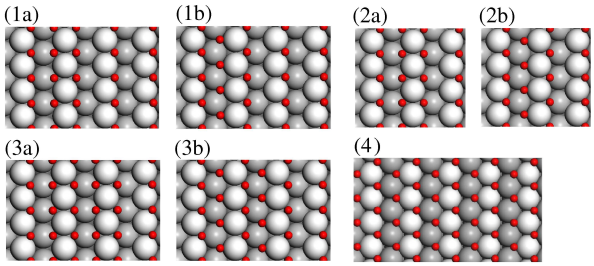

Figure 5.9: Top views of studied O/Re(10$\bar{1}$0) configurations for (1a and 1b) 1.33 GML in a (1×3)-4O overlayer, (2a and 2b) 1.5 GML in a (1×2)-3O overlayer, (3a and 3b) 1.66 GML in a (1×3)-5O overlayer. (4) is the most stable structure for 2 GML in a (1×1)-2O overlayer.

Among the different adsorbate structure possible with 0.50 GML we studied: (1×2)-1O, (2×1)-1O, c(2×2)-1O, and c(2×4)-2O. Top views of these configurations are shown in Figs. 5.8(3a)–(3d). The c(2×4)-2O structure is found to be most stable, having a binding energy of 3.79 eV. This is in good agreement with the results obtained by other groups for the O/Co(10$\bar{1}$0) (experiment) [112] and O/Ru(10$\bar{1}$0) (theory and experiment) [109] systems. Oxygen adsorption on Co(10$\bar{1}$0) at low coverages leads to a metastable c(2×4)-2O phase, which forms a (2×1)-1O upon heating. LEED experiments and DFT calculations on Ru(10$\bar{1}$0) also showed the existence of a c(2×4)-2O adlayer. It seems that with 0.50 GML the interaction between oxygen and Re(10$\bar{1}$0) is significantly stronger than that between oxygen and Ru(10$\bar{1}$0) [109] by 0.98 eV.
For 0.66 GML we modeled (1×3)-2O and (3×1)-2O overlayers as shown in Figs. 5.8(4a)–(4c). In the (3×1) surface unit cell, we considered two different structures, namely (3×1)a- and (3×1)b-2O. It was found that the (3×1)a-2O configuration (E_{bind} = 3.61 eV) is most stable. Since the difference between the binding energies of (1×3)-2O, proposed by experiments, and (3×1)a-2O is very small, we suggest that both might be present on the surface.
At a coverage of 1.00 GML, we considered the (1×1)-1O and (2×1)$p2mg$-2O structures shown in Figs. 5.8(5a) and (5b). Our calculations indicate that the former is more stable by 0.19 eV. The calculated binding energy of 3.60 eV for (1×1)-1O is similar to the value obtained for the (1×2)-1O, (1×3)-1O, and (1×3)-2O adlayers, showing minor impact of interactions between adatoms bound to adjacent rows.
For coverages above 1.00 GML, we focused first on structures with two O atoms per unit cell (Θ=2.00 GML) to obtain more knowledge about the interaction between adsorbates. This information was then used to predict stable adlayer configurations for the following coverages: 1.33 ((1×3)-4O), 1.50 ((1×2)-3O), and 1.66 ((1×3)-5O) GML. At 2.00 GML, a variety of adsorbate overlayers could form. Using the position labeling of Fig. 5.7, several possible combinations of distinguishable surface sites have been studied. Among these configurations

occupying three-fold hollow H1- and H2-sites (Fig 5.9(4)) leads to the highest adsorption energy of 2.76 eV. After that, we checked two most probable configurations for 1.33, 1.50, and 1.66 GML as shown in Fig. 5.9(1a)–(3b). It turned out that structures in which all adsorbates occupy H1-sites (Figs. 5.9(1a), (2a) and (3a)) are energetically more favorable than those with adatoms at H2-sites (Figs. 5.9(1b), (2b) and (3b)).

5.2.2 Reconstructed O/Re(10$\bar{1}$0)-(1×2) and -(1×3)

In order to find the most favorable structures for O on reconstructed Re(10$\bar{1}$0), we studied oxygen binding at several possible adsorption sites as shown in Fig. 5.10 for single, double, and triple missing-row (MR) structures as described in Chapter 4. The single MR structure is a combination of the Re(10$\bar{1}$0)-(1×1) and the Re(10$\bar{1}$0)-(1×2) surfaces. This allows us to reduce the computational effort for reconstructed Re(10$\bar{1}$0)-(1×2) by studying only the most favorable arrangements of oxygen atoms in the (1×2) part of the single MR surface. The binding sites on Re(10$\bar{1}$0)-(1×2) are as labeled for single MR in Fig. 5.10.

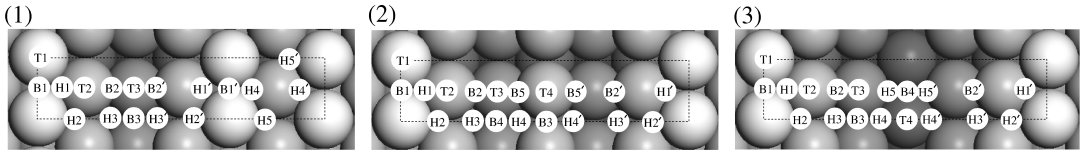

Figure 5.10: Top views of (1) Re(10$\bar{1}$0)-(1×3) single MR, (2) Re(10$\bar{1}$0)-(1×3) double MR, and (3) Re(10$\bar{1}$0)-(1×3) triple MR showing all binding sites at which O adsorption has been studied.

We started our studies with one O per unit cell and found three-fold hollow H1-sites to be most stable for all the considered reconstructed surfaces. A similar preference was also observed for the Re(10$\bar{1}$0)-(1×1) surface. While the calculated binding energies at H1 are very similar for single MR (E_{bind} =3.81 eV), double MR (E_{bind} =3.84 eV), and triple MR (E_{bind} =3.83 eV), slightly stronger binding (E_{bind} =3.89 eV) is obtained at this site on Re(10$\bar{1}$0)-(1×2). Interestingly, the energy differences between different sites on each of the reconstructed

coverage (GML)	E_{bind} (eV)
0.5	3.89
1.0	3.58
1.5	3.26
2.0	2.98

Table 5.4: Binding energies (referenced to $^1/_2\,O_2$) for oxygen on the reconstructed Re(10$\bar{1}$0)-(1×2) surface at different coverages; only the most stable structure for each coverage is listed.

coverage (GML)	single MR E_{bind} (eV)	double MR E_{bind} (eV)	triple MR E_{bind} (eV)	
0.33	3.81	3.84	3.83	
0.66	3.78	3.67	3.66	
1.00	3.50	3.53	3.50	(Fig. 5.14(3a))
			3.50	(Fig. 5.14(3b))
1.33	3.30	3.36	3.30	
1.66	3.21	3.20	3.19	(Fig. 5.14(5a))
			3.19	(Fig. 5.14(5b))
2.00	2.99	2.97	3.04	(Fig. 5.14(6a))
			3.04	(Fig. 5.14(6b))

Table 5.5: Binding energies (referenced to $^1/_2\,O_2$) for oxygen on the reconstructed Re(10$\bar{1}$0)-(1×3) surfaces at different coverages; only the most stable structure for each coverage is listed.

surfaces are much smaller than those on Re(10$\bar{1}$0)-(1×1) for low coverages.
In order to explore the preferred overlayers with more than one O adatom per surface unit cell, we considered several possible combinations of distinguishable surface sites (as labeled in Fig. 5.10) at each of these coverages. Figs. 5.11–5.14 summarize the most favorable structures obtained in our calculations for different coverages of oxygen on the Re(10$\bar{1}$0)-(1×2) and -(1×3) surfaces. The corresponding binding energies are plotted in Fig. 5.15 and are listed in Tabs. 5.4 and 5.5. In Fig. 5.15 we also include the results obtained for O/Re(10$\bar{1}$0)-(1×1). It can be seen from this figure that there are some wiggles for coverages lower than 1.00 GML on the unreconstructed surface. This is related to the existence of row-pairing of Re atoms, which causes the binding energies to increase by $\sim$0.1 eV at 0.25 and 0.50 GML. Interestingly, Fig. 5.15 indicates that the adsorption energy of O is higher on the reconstructed surfaces than on Re(10$\bar{1}$0)-(1×1) in most considered coverages (except at 1.00 GML). The advantage of the missing-row reconstruction is more significant at higher coverages, indicating that additional O atoms prefer positions in the MR trough. Therefore, at the highest coverage examined (2.00 GML), the strongest binding energy is obtained on the triple MR structure that has the deepest trough among the studied structures.
A potential energy surface (PES) (Fig. 5.16) has been constructed with the binding energies obtained for one oxygen per unit cell of the triple MR surface. This plot makes apparent that O is more stable in the trough than on the ridges. However, this preference is weaker for those sites in the bottom of the trough. Since the energetic difference between H1 (the preferred position)

and the B1 site on the ridges is large, we find that diffusion along path (a) is unfavorable with a largest barrier of $\sim 0.8\,\text{eV}$. Interestingly, this plot also shows that oxygen-diffusion along the –H1–H2–H1– direction (path (b)) is hindered by a relatively low barrier of $\sim 0.45\,\text{eV}$. Therefore, diffusion is expected to occur predominantly along the ridges, rather than across the troughs.

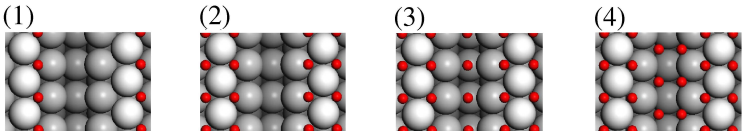

Figure 5.11: Top views of the most stable O/Re(10$\bar{1}$1)-(1×2) structures for different coverages: (1) 0.50, (2) 1.00, (3) 1.50, (4) 2.00 GML.

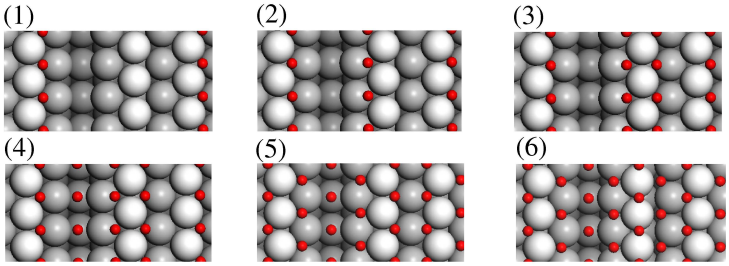

Figure 5.12: Top views of the most stable O/Re(10$\bar{1}$1)-(1×3) single MR structures for different coverages: (1) 0.33, (2) 0.66, (3) 1.00, (4) 1.33, (5) 1.66, (6) 2.00 GML.

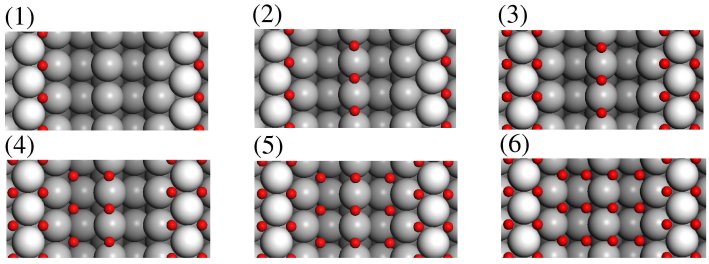

Figure 5.13: Top views of the most stable O/Re(10$\bar{1}$1)-(1×3) double MR structures for different coverages: (1) 0.33, (2) 0.66, (3) 1.00, (4) 1.33, (5) 1.66, (6) 2.00 GML.

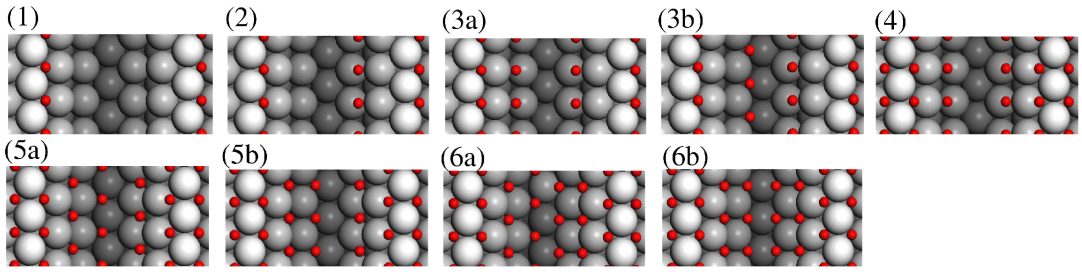

Figure 5.14: Top views of the most stable O/Re(10$\bar{1}$1)-(1×3) triple MR structures for different coverages: (1) 0.33, (2) 0.66, (3a and 3b) 1.00, (4) 1.33, (5a and 5b) 1.66, (6a and 6b) 2.00 GML.

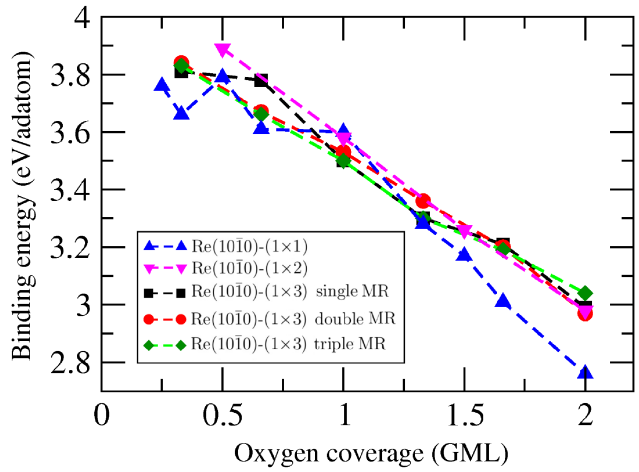

Figure 5.15: Binding energy (referenced to $^1/_2\,O_2$) as a function of oxygen coverage on Re(10$\bar{1}$0).

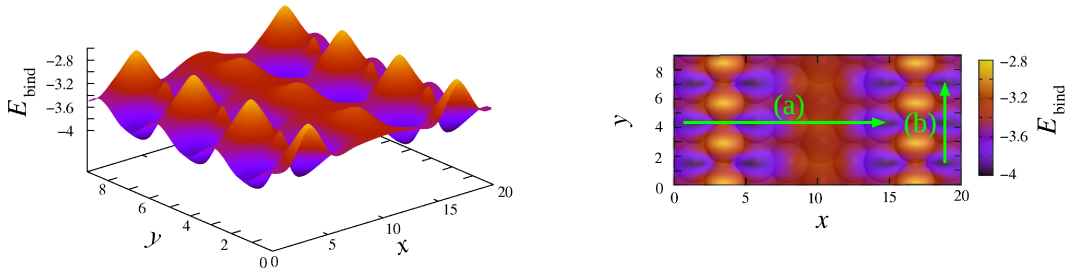

Figure 5.16: Adsorption energy distribution (in eV and referenced to $^1/_2\,O_2$) for binding 1 GML of atomic oxygen onto the Re(10$\bar{1}$0)-(1×3) triple MR surface. X and y are given in Å. The arrows indicate different paths for O diffusion on the surface.

5.2.3 Unreconstructed N/Re(10$\bar{1}$0)-(1×1)

We studied the adsorption of atomic nitrogen on Re(10$\bar{1}$0)-(1×1) with coverages of Θ=0.25, 0.33, 0.50, 0.66, 1.00, 1.33, 1.66, and 2.00 GML. Similar configurations as for O adsorption were considered (see Figs. 5.8 and 5.9). The binding energies of N on these structures are listed in Tab. 5.6.

structure	coverage (GML)	E_{bind} (eV)
(2×2)-1N	0.25	1.77
c(2×4)-1N	0.25	1.74
(1×3)-1N	0.33	1.34
(3×1)-1N	0.33	1.67
(2×1)-1N	0.50	1.69
(1×2)-1N	0.50	1.37
c(2×2)-1N	0.50	1.74
c(2×4)-2N	0.50	1.79
(1×3)-2N	0.66	1.27
(3×1)a-2N	0.66	1.51
(3×1)b-2N	0.66	1.69
(1×1)-1N	1.00	1.27
(2×1)$p2mg$-2N	1.00	1.61
(1×3)-4N	1.33	0.93
(1×2)-3N	1.50	0.82
(1×3)-5N	1.66	0.60
(1×1)-2N	2.00	0.23

Table 5.6: Calculated binding energies (referenced to $^1/_2\,N_2$) for nitrogen adsorbed at three-fold hollow H1-sites of the unreconstructed Re(10$\bar{1}$0)-(1×1) surfaces with different overlayers and coverages.

As observed in the case of O adsorbate, the preferred binding site for N is also the three-fold hcp H1-site. Furthermore, for all coverages except for 0.66, 1.00, and 2.00 GML our calculations show similar results to those obtained before for O.

At 0.66 GML (see Fig. 5.8), the binding energy of nitrogen in the (3×1)b-2N configuration (E_{bind} = 1.69 eV) is more stable over (3×1)a-2N by 0.1 eV, showing a strong N–N repulsion in the direction along the close-packed Re rows, which can be further confirmed by a significantly smaller binding energy (E_{bind} = 1.27 eV) for (1×3) than for (3×1)a-2N.

For 1.00 GML the (2×1)$p2mg$-2N is preferred with a binding energy of 1.61 eV. The (1×1)-1N structure is less stable by 0.34 eV, showing a strong adsorbate–adsorbate repulsion between nitrogen atoms within the troughs. Our results for N/Re(10$\bar{1}$0) at 1.00 GML are similar to those obtained for the O/Ru(10$\bar{1}$0) system, where DFT calculations by Schwegmann *et al.* showed that the binding energy in a (2×1)$p2mg$-2O configuration is higher than in a (1×1)-O [109].

Fig 5.18 shows PES for one nitrogen per unit cell (Θ=1.00 GML). It can be seen that diffusion of nitrogen along path (a) is hindered by a relatively high barrier of ∼0.9 eV. In addition, the largest energy barrier for path (b) is ∼1.1 eV. Therefore, N atoms would be strongly localized at H1-positions.

At 2.00 GML, we found that the configuration where both nitrogen atoms occupy H1-sites (Fig. 5.17) is most stable. The corresponding binding energy is only slightly exothermic (E_{bind}=0.23 eV).

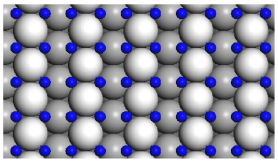

Figure 5.17: Top view of the most stable structure of N/Re(10$\bar{1}$0) in a (1×1)-2N overlayer at a coverage of 2 GML.

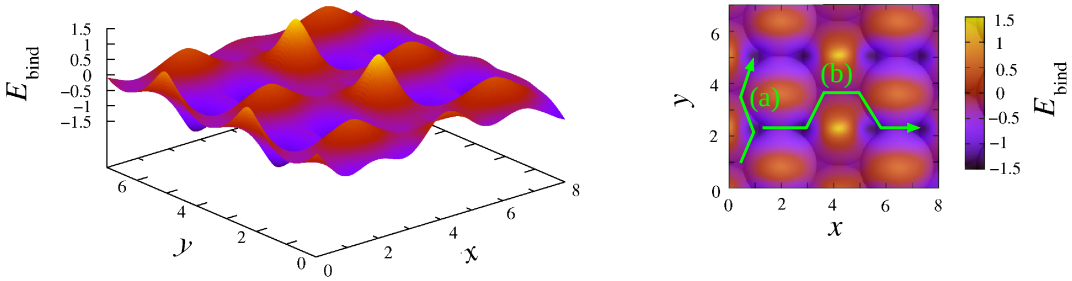

Figure 5.18: Adsorption energy distribution (in eV and referenced to $^1/_2\,N_2$) for binding 1 GML of atomic nitrogen onto Re(10$\bar{1}$0). X and y are given in Å. The arrows indicate different paths for N diffusion on the surface.

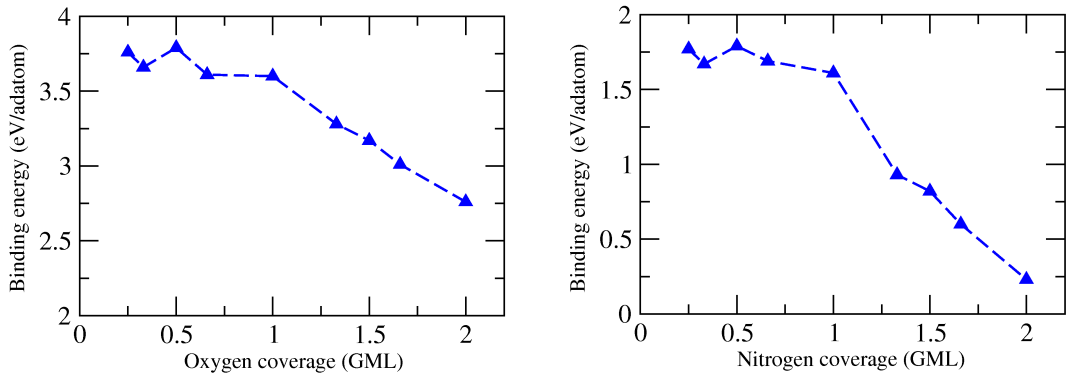

Figure 5.19: Binding energy (referenced to $^1/_2\,O_2$ and $^1/_2\,N_2$) as a function of oxygen (left) and nitrogen (right) coverage on the unreconstructed Re(10$\bar{1}$0)-(1×1) surface.

We now compare (see Fig. 5.19) the adsorption energies versus coverages for N with O adsorption on unreconstructed Re(10$\bar{1}$0)-(1×1). It can be seen that there are again wiggles for nitrogen coverages lower than 1 GML due to the row-pairing of Re atoms (at 0.25 and 0.5 GML). A decrease in binding energy with increasing oxygen and nitrogen coverage is observed between 1 and 2 GML. The drop in the binding energy is because of the repulsive lateral interactions between adsorbates. We find these interactions to be more pronounced for N than for O adlayers at high coverages.

5.3 Re(10$\bar{1}$1)

From LEED experiments, Wang *et al.* proposed that the Re(10$\bar{1}$1) facets, which are formed in addition to the Re(10$\bar{1}$0) facets on oxygen-covered Re(11$\bar{2}$1) (see Chapter 3), are reconstructed and have a (1×2) missing-row structure [7].
In this section we discuss our results for oxygen and nitrogen adsorption on unreconstructed Re(10$\bar{1}$1)-(1×1)[3] and reconstructed Re(10$\bar{1}$1)-(1×2) for different coverages: 0.25, 0.50, 1.00, and 2.00 GML. The probable binding sites at which O and N adsorptions have been considered are displayed in Fig. 5.20. The optimized structures of the most stable configurations for the different coverages are shown in Figs. 5.21, 5.22, 5.25, and 5.26. Tabs. 5.7–5.10 summarize the corresponding adsorption energies. To study the stability of different sites we started our calculations with 0.5 GML on the unreconstructed and reconstructed surfaces. At 0.25 ML, we only considered the adsorption sites with higher binding energies.

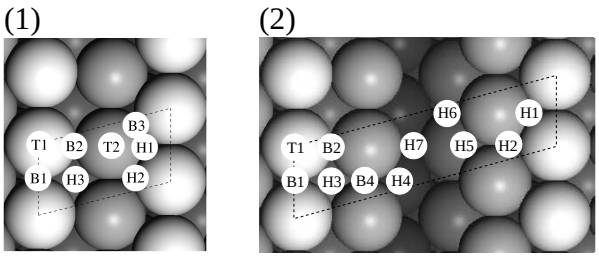

Figure 5.20: Top views of (1) Re(10$\bar{1}$1)-(1×1) and (2) Re(10$\bar{1}$1)-(1×2) showing all binding sites at which O and N adsorption has been studied.

5.3.1 Unreconstructed O/Re(10$\bar{1}$1)-(1×1)

For (2×2)-1O overlayers with coverage Θ=0.25 GML, the three-fold hollow H1 (E_{bind}=3.79 eV) sites are energetically preferred (see Fig. 5.21(1)).

[3] In Chapter 4 we have seen that Re(10$\bar{1}$1)A is more stable than Re(10$\bar{1}$1)B. Therefore, here we continue our studies by considering the former structure and for simplicity we refer to it as Re(10$\bar{1}$1).

At a coverage of 0.5 GML, we focused on the (2×1)- and (1×2)-1O adlayers and found the former structure to be more stable. In this configuration oxygen binds most strongly again at the H1-site (Fig. 5.21(2a)) for which we calculated a binding energy of 3.80 eV. This value is very close to that already found for 0.25 GML, which is related to a similar row-pairing of substrate atoms in (2×2)-1O and (2×1)-1O and also a negligible interaction between oxygen adatoms of different rows.
Interestingly, in case of the (1×2)-1O structure the H2-site (Fig. 5.21(2b)) becomes the most stable (E_{bind}=3.65 eV). In the (2×1)-O configuration with O adatoms occupying the H2-positions adsorbate–adsorbate separation along the same row is larger, but adsorption energy is 0.15 eV lower. We will address this point later in the text when we discuss unreconstructed surfaces at higher coverages and reconstructed surfaces.
At 1 GML, the most favorable binding site for oxygen in the (1×1)-1O adlayer is a two-fold B2-site (see Fig. 5.21(3a)), where oxygen binds to one top-layer and one second-layer Re atoms, with a binding energy of 3.55 eV. This value is only 0.02 and 0.04 eV larger than that for a structure with oxygen at H2 or H1 shown in Figs. 5.21(3b) and (3c). Already for the (1×2)-1O and (2×1)-1O adlayers we have seen that H2 and H1 are the most stable adsorption sites, respectively. In the following we compare our results for 1 GML with those obtained for 0.5 GML.

coverage (GML)		E_{bind} (eV)
0.25		3.79
0.50	Fig. 5.21(2a)	3.80
	Fig. 5.21(2b)	3.65
1.00	Fig. 5.21(3a)	3.55
	Fig. 5.21(3b)	3.53
	Fig. 5.21(3c)	3.51
2.00	Fig. 5.21(4a)	3.12
	Fig. 5.21(4b)	3.10

Table 5.7: Binding energies (referenced to $^1/_2\,O_2$) for oxygen on Re(10$\bar{1}$1)-(1×1) at different coverages; only the most stable structure for each coverage is listed (see Fig. 5.21).

Due to the reduction in the O–O separation along the close-packed Re rows, the binding energy at the H1-site is lower in the (1×1) structure than in the (2×1) periodicity. This can also be concluded from a comparison of adsorption energies for (1×2) and (2×1) adlayers. The similar binding energy of O in the (1×1) and (1×2) at H1-site shows that adsorbates along each substrate row have very weak interaction with those along neighboring substrate row. This is not the case for the H2-site and we have stronger binding energy at this position in (1×2) than in both (1×1) and (2×1). This might be attributed to the presence of neighboring substrate rows on which adsorption of oxygen leads to a reduction in the overall adsorption energy.
Using the position labeling of Fig. 5.20(1), five possible combinations of distinguishable surface sites have been studied at 2 GML (see Tab. B.15). It was found

that a configuration in which O atoms occupy the first and second favorable sites (found at 1 GML), B2 and H2, has the highest binding energy of 3.11 eV (see Fig. 5.21(4a)). A structure with adsorbed O at the first and third most stable sites (see Fig. 5.21(4b)) is only 0.01 meV less stable.

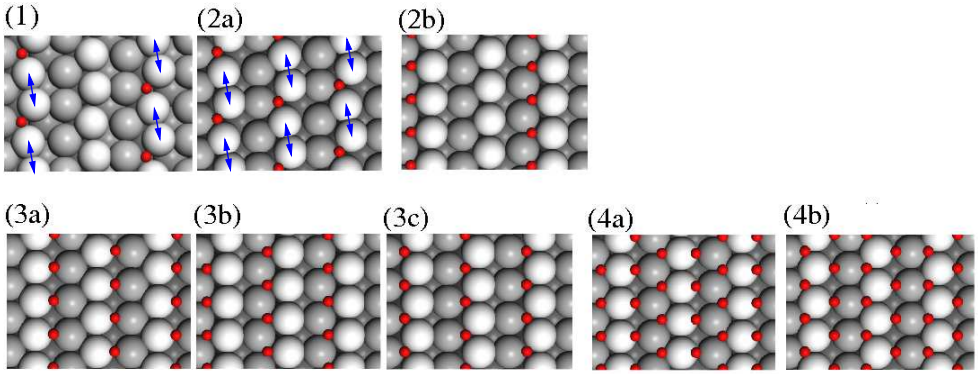

Figure 5.21: Top views of the most stable structures of oxygen-covered unreconstructed Re(10$\bar{1}$1)-(1×1) in different overlayers and coverages: (1a and 1b) (2×2) overlayer at 0.25 GML, (2a) (2×1) and (2b) (1×2) overlayer at 0.5 GML, (3a-3c) (1×1) overlayer at 1 GML, (4a and 4b) (1×1) overlayer at 2 GML. The arrows indicate the Re atoms that move toward each other upon relaxation.

5.3.2 Reconstructed O/Re(10$\bar{1}$1)-(1×2)

On this surafce we began our investigation with the adsorption of one O per unit cell (Θ=0.5 GML in a (1×2)-O structure) and found that the three-fold H2-site (Fig. 5.22(1)) is again the preferred site (E_{bind} =3.87 eV). The adsorption energy of O at the H2-site in a (2×2)-O adlayer (Θ=0.25 GML) is only 0.03 eV lower, indicating a weak lateral O–O repulsion along the closely-packed rows. The row-pairing of the Re atoms in the topmost surface layer of (2×2)-O is also negligible.

The binding energy at the H2-site in the (1×2)-1O adlayer on Re(10$\bar{1}$1)-(1×2) is 0.22 eV larger than that in the same overlayer on the unreconstructed surface. This suggests that removing every second row of topmost Re atoms has a significant effect on the

coverage (GML)		E_{bind} (eV)
0.25	Fig. 5.22(1)	3.90
0.50	Fig. 5.22(2)	3.87
1.00	Fig. 5.22(3)	3.60
2.00	Fig. 5.22(4)	3.19

Table 5.8: Binding energies (referenced to $^1/_2\,O_2$) for oxygen on Re(10$\bar{1}$1)-(1×2) at different coverages; only the most stable structure for each coverage is listed (see Fig. 5.22).

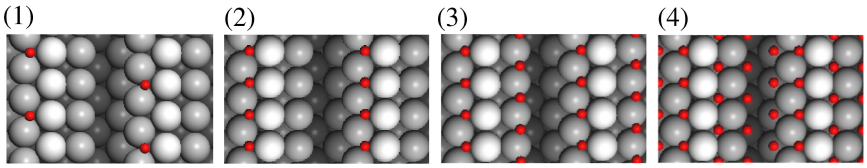

Figure 5.22: Top views of the most stable structures of oxygen-covered reconstructed Re(10$\bar{1}$1)-(1×2) in different overlayers and coverages: (1) (2×1) overlayer at 0.25 GML, (2) (1×1) overlayer at 0.5 GML, (3) (1×1) overlayer at 1 GML, (4) (1×1) unit cell with 2 GML.

oxygen binding energy at this site. This is in line with our results on the corresponding unreconstructed surface, where we also found that the absence of the binding to every second rows is more favorable for O atoms at H2 sites.
Regarding 1 GML, among the studied systems (Tab. B.17) we find the structure with oxygens at H2 and B4 (see Fig. 5.22(3)) to be most stable, giving a binding energy of 3.60 eV. The corresponding $\bar{E}_{\text{bind}}$ value is only 0.02 eV larger, which shows that both oxygen atoms behave as almost independent adsorbates at this coverage.

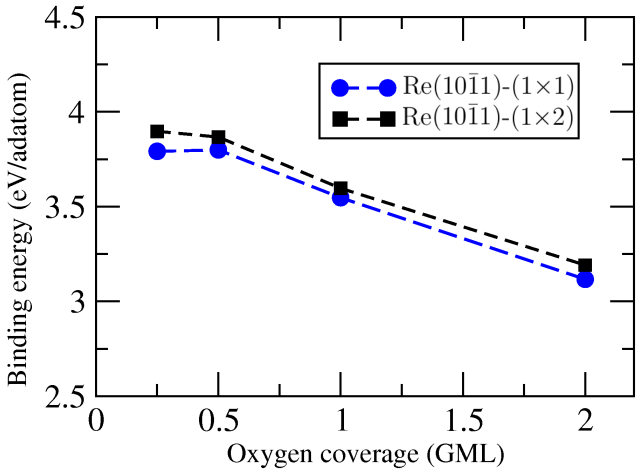

Figure 5.23: Binding energy (referenced to $^1/_2\,O_2$) as a function of oxygen coverage on Re(10$\bar{1}$1)-(1×1) and -(1×2).

Finally, the preferred structure at Θ=2 GML (Fig. 5.22(4)) with an adsorption energy of 3.19 eV and $\bar{E}_{\text{bind}}$=3.52 eV shows much stronger interactions between adatoms compared to the lower coverages (Θ=0.5 and 1 GML).
The change in binding energy upon increasing oxygen coverage on Re(10$\bar{1}$1)-(1×1) and -(1×2) is displayed in Fig. 5.23. Our calculations show influence of removing entire atomic rows (going from the unreconstructed to the (1×2)-

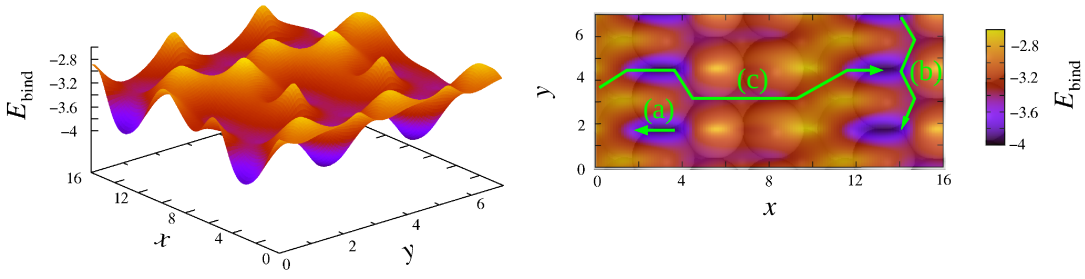

Figure 5.24: Adsorption energy distribution (in eV and referenced to $^1/_2\,O_2$) for binding 1 GML of atomic oxygen onto Re(10$\bar{1}$1)-(1×2). X and y are given in Å. The arrows indicate different paths for O diffusion on the surface.

reconstructed surfaces): The adsorption energy of oxygen atoms on the reconstructed structure is higher for all coverages. This preference remains almost constant between 0.25 and 2.00 GML. Therefore, our calculations qualitatively support the experimental observation of a (1×2) reconstruction on the O-covered {10$\bar{1}$1} facets.
Finally, a potential energy surface has been constructed with the adsorption energies obtained for one oxygen per (1×1)-unit cell of Re(10$\bar{1}$1)-(1×2) (see Fig. 5.24). This plot shows that the energy barrier for diffusion between H2- and H5-sites (path (a)) is only 0.25 eV, indicating that O atoms might diffuse between these sites with a certain rate at elevated temperatures. Diffusion of O along the –H2–H1–H2– direction (path (b)) shows an energy barrier of ∼0.45 eV, approximately 2.7 times lower than the largest energy barrier for the –H2–H5–H6–H5–H2– pathway (path (c)). Therefore, at finite temperature O diffuses preferentially along the ridges but not across the MR troughs.

5.3.3 Unreconstructed N/Re(10$\bar{1}$1)-(1×1)

For 0.25–1.00 GML, nitrogen binds most strongly at four-fold hollow H3-sites (Figs. 5.25(1)–(3)). Three-fold hollow H1- and H2-sites are found to be significantly less favorable than the H3-sites. Since there is a significant row-pairing of the topmost surface atoms (connected by arrows in Fig. 5.25) in (2×2)-1N, but not in the (1×2)-1N and (2×1)-1N structures, a higher

coverage (GML)		E_{bind} (eV)
0.25	Fig. 5.25(1)	2.21
0.50	Fig. 5.25(2a)	2.07
	Fig. 5.25(2b)	1.60
1.00	Fig. 5.25(3)	1.65
2.00	Fig. 5.25(4)	0.93

Table 5.9: Binding energies (referenced to $^1/_2\,N_2$) for nitrogen on Re(10$\bar{1}$1)-(1×1) at different coverages; only the most stable structure for each coverage is listed (see Fig. 5.25).

binding energy is obtained for 0.25 GML than for 0.50 GML.
At 0.5 GML, the binding energy of the (1×2)-1N adlayer (E_{bind} =1.60 eV) is considerably lower than that of (2×1)-1N (E_{bind} =2.07 eV), showing a notable repulsion between adatoms along the close-packed Re rows.
Increasing the coverage to 1 GML, we find a binding energy close to that obtained for 0.5 GML in the (1×2)-1N configuration. Therefore, we can conclude that the interaction between nitrogen adatoms of different rows is small.
At 2 GML, the structure shown in Fig. 5.25(4) is the most stable one (E_{bind} =0.93 eV). This result is consistent with the higher binding energy of nitrogen at H3- and H1-sites with respect to other adsorption sites at lower coverages.

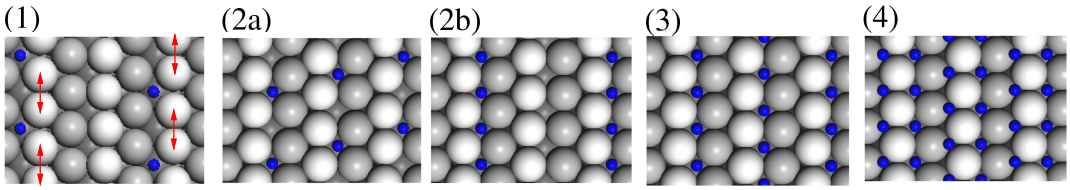

Figure 5.25: Top views of the most stable structures of nitrogen-covered unreconstructed Re(10$\bar{1}$1)-(1×1) in different overlayers and coverages: (1) (2×2) overlayer at 0.25 GML, (2a) (2×1) and (2b) (1×2) overlayer at 0.5 GML, (3) (1×1) overlayer at 1 GML, (4) (1×1) overlayer at 2 GML. The arrows indicate the Re atoms that move toward each other upon relaxation.

5.3.4 Reconstructed N/Re(10$\bar{1}$1)-(1×2)

By performing the same calculations as those discussed for O adsorption we find that the H2-site is also preferred for N adatoms at 0.25 and 0.50 GML (Figs. 5.22(1) and (2)). As mentioned in the previous section, on the unreconstructed surface, N binds most strongly at H3-site in all considered overlayers and coverages. Considering 0.25 GML in the (2×2)-1N structure and 0.50 GML in the (1×2)-1N adlayer, we find that missing-row reconstruction stabilizes (destabilizes) the H2-sites (the H3-sites) compared to Re(10$\bar{1}$1)-(1×1). Since the row-pairing of the first layer

coverage (GML)		E_{bind} (eV)
0.25	Fig. 5.22(1)	1.90
0.50	Fig. 5.22(2)	1.60
1.00	Fig. 5.26(1)	1.36
	Fig. 5.26(2)	1.36
2.00	Fig. 5.22(4)	1.03

Table 5.10: Binding energies (referenced to $^1/_2\,N_2$) for nitrogen on Re(10$\bar{1}$1)-(1×2) at different coverages; only the most stable structure for each coverage is listed (see Fig. 5.26).

atoms in N/Re(10$\bar{1}$1)-(1×2) is not considerable at 0.25 GML and not possible at 0.50 GML, the lower binding energy calculated for the latter coverage is mainly due to the lateral N–N repulsions. The most stable structures for 1.00 and 2.00 GML, which are different compared to those determined in O/Re(10$\bar{1}$1)-(1×2), are shown in Figs. 5.26(a) and (b). The data obtained for N adsorption on Re(10$\bar{1}$1) was used to plot the coverage dependence of the nitrogen binding energy (Fig. 5.27). It turned out that the nitrogen adsorption energy is higher on the unreconstructed surface than on Re(10$\bar{1}$1)-(1×2), from 0.25 to 1.00 GML. However, the adsorption of 2.00 GML of N makes the (1×2) MR reconstruction more stable. Unfortunately, there are no experimental studies on N/Re(10$\bar{1}$1) to compare our results with.
We now analyze the PES (Fig. 5.28) for one nitrogen atom per unit cell of Re(10$\bar{1}$1)-(1×1). This plot makes apparent that N prefers to be in the trough. Since the energetic difference between the adsorption sites on the ridges and in the troughs is substantial, the crossing of the ridge along path (a) is considerably unfavorable. However, there is a relatively low energy barrier of $\sim$0.5 eV for diffusion along –H3–B2–H3– direction (path (b)).

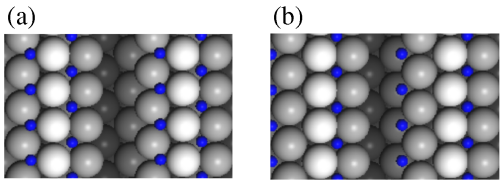

Figure 5.26: Top views of the most stable structures of nitrogen-covered reconstructed Re(10$\bar{1}$1)-(1×2) in a (1×1) overlayer at 1 GML.

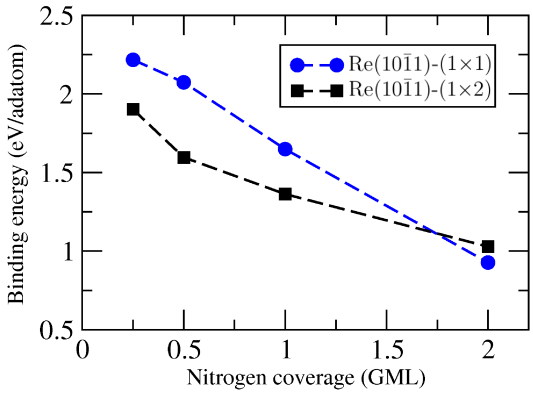

Figure 5.27: Binding energy (referenced to $^1/_2\,N_2$) as a function of nitrogen coverage on Re(10$\bar{1}$1)-(1×1) and -(1×2).

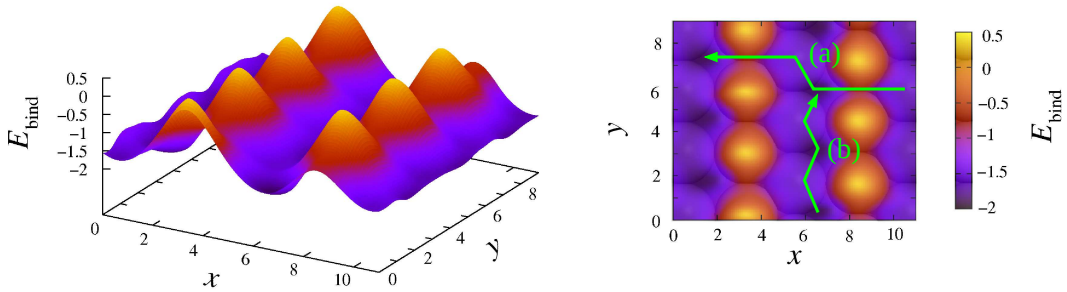

Figure 5.28: Adsorption energy distribution (in eV and referenced to $^1/_2\,N_2$) for binding 1 GML of atomic nitrogen onto Re(10$\bar{1}$1)-(1×1). X and y are given in Å. The arrows indicate different paths for N diffusion on the surface.

5.4 Re(13$\bar{4}$2)

Experimentally, it was found that nitrogen adsorption causes the Re(11$\bar{2}$1) surface to become completely faceted, forming two-sided ridge-like structures (see Section 3.2). The orientations of the faces of the ridges are (13$\bar{4}$2) and (31$\bar{4}$2), which are different from the facets found in the oxygen-induced faceting of Re(11$\bar{2}$1). To complete our study of the faces which occur when the Re(11$\bar{2}$1) surface forms facets, we investigate now the adsorption of atomic oxygen and nitrogen on Re(13$\bar{4}$2)[4] for coverages ranging from 1 to 6 GML. There are a lot of different sites on the Re(13$\bar{4}$2) surface. Fig. 5.29 shows 21 probable binding sites, which we assumed as initial positions for O and N adsorbates. Our results are summarized in Figs. 5.30 and 5.32 as well as Tabs. 5.11 and 5.12.

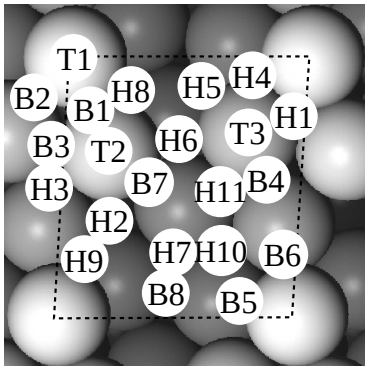

Figure 5.29: Top view of Re(13$\bar{4}$2) showing all binding sites at which O and N adsorption has been studied.

[4]In Chapter 4 we have seen that Re(13$\bar{4}$2)A and Re(13$\bar{4}$2)B have the same stability. Therefore, here we continue our studies by considering one of these configurations (Re(13$\bar{4}$2)A) and for simplicity we refer to it as Re(13$\bar{4}$2).

5.4.1 O/Re(13$\bar{4}$2)

Our calculations reveal that the most stable binding site for 1 GML is a three-fold hollow H1-site (see Fig. 5.30(1)), where each adsorbate binds to top, second, and third-layer Re atoms, with a binding energy of 4.03 eV. This value is higher than that obtained at the similar three-fold hollow H1-sites on Re(10$\bar{1}$0) and Re(10$\bar{1}$1) at low coverages.
The O atoms are less stable at the lower accessible positions below the surface-plane of Re(13$\bar{4}$2). This can be seen in the full PES (Fig. 5.31). As the PES has been constructed with the binding energies obtained for one oxygen per unit cell, Fig. 5.31 reflects the case of Θ=1 GML. This plot shows that the energy barrier for diffusion between H1- and B1-sites is only 0.1 eV, suggesting a mixed site occupation at finite temperatures. The largest energy barrier for diffusion along both directions (a) and (b) is relatively high ($\sim$0.8 eV). All other possible diffusion paths are considerably unfavorable. Therefore, O atoms would be trapped in the H1- and B1-sites at low temperature.

coverage (GML)		E_{bind} (eV)
1		4.03
2		3.78
3		3.67
4	Fig. 5.30(4a)	3.55
	Fig. 5.30(4b)	3.54
5		3.38
6		3.15

Table 5.11: Binding energies (referenced to $^1/_2\,O_2$) for oxygen on Re(13$\bar{4}$2) at different coverages; only the most stable structure for each coverage is listed (see Fig. 5.30).

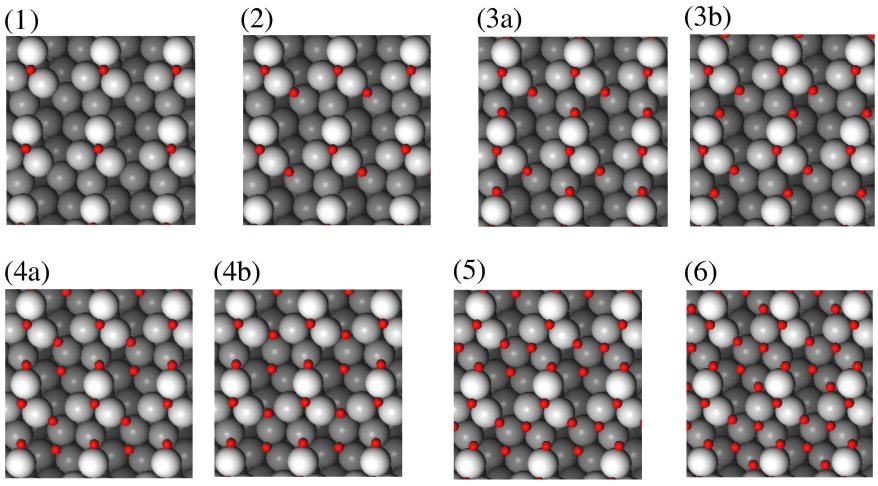

Figure 5.30: Top views of the most stable structures of oxygen-covered Re(13$\bar{4}$2) in a (1×1) overlayer and different coverages: (1) 1 GML, (2) 2 GML, (3a and 3b) 3 GML, (4a and 4b) 4 GML, (5) 5 GML, (6) 6 GML.

As a consequence of the large surface unit cell of Re(13$\bar{4}$2), we observe a small O–O repulsion for 2 GML $\leq \Theta \leq$ 4 GML. The calculated adsorption energy for the most stable structures at Θ=2 (Fig. 5.30(2)) and 3 GML (Fig. 5.30(3)) is 3.78 and 3.67 eV, which are both only 0.13 eV smaller than the corresponding $\bar{E}_{\mathrm{bind}}$ values (see eq. (5.2)). At a coverage of 4 GML, the most stable structure (Fig. 5.30(4a)) has a binding energy of 3.55 eV, which is only 0.07 eV lower than the value obtained for $\bar{E}_{\mathrm{bind}}$. For this coverage, the second favorable structure shown in Fig. 5.30(4b) is 0.01 eV less stable.
A relatively strong O–O interaction between the adatoms is found for 5 and 6 GML. At 5 GML, in the preferred structure (Fig. 5.30(5)), where the fifth O atom binds at the vacant H11-position on the configuration of Fig. 5.30(4b), the binding site of one of the preadsorbed atoms changes from H6 to B7 during geometry optimization (to minimize adsorbate–adsorbate repulsions). The relatively strong O–O interaction between the adatoms is also confirmed by the calculated binding energy of 3.38 eV, which is 0.21 eV lower than the $\bar{E}_{\mathrm{bind}}$ value. Finally, the $\bar{E}_{\mathrm{bind}} - E_{\mathrm{bind}}$ value increases to 0.39 eV at 6 GML. In the next section, we present the results of N/Re(13$\bar{4}$2) and compare the changes in the adsorption energy introduced by O and N adsorbates.

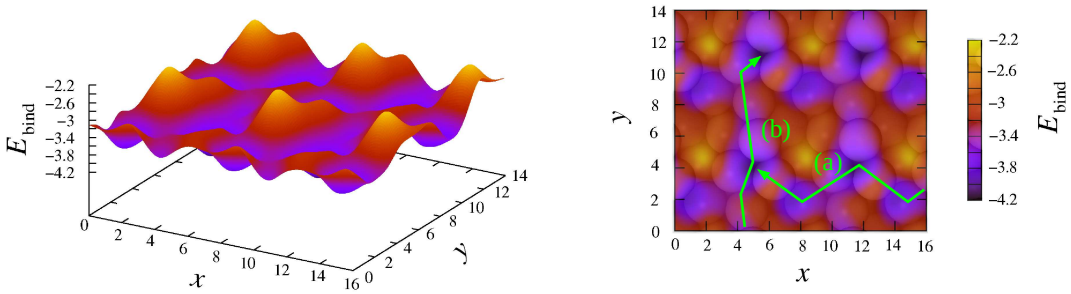

Figure 5.31: Adsorption energy distribution (in eV and referenced to $^1/_2\,O_2$) for binding 1 GML of atomic oxygen onto Re(13$\bar{4}$2). X and y are given in Å. The arrows indicate different paths for O diffusion on the surface.

5.4.2 N/Re(13$\bar{4}$2)

For N-adsorbed systems we followed a similar procedure as described in the previous sections. It turned out that at 1 GML the most stable binding site is different from that predicted for oxygen adsorption. At this coverage, N prefers the H6-position (Fig. 5.32(1)), where each adsorbate forms bonds to the second, third, fifth, and eighth-layer Re atoms, finally resulting in a four-fold binding. The calculated binding energy of N in the H6-site (E_{bind}=2.35 eV) is somewhat larger than that in the H1-site (E_{bind}=2.07 eV) and B1-site (E_{bind}=2.03 eV). The PES (Fig. 5.33) shows that N diffusion from H6-site to H1- or B1-site (path (a)) has

a barrier of ~ 0.5 eV. All other considered adsorption positions are significantly less stable compared to H6, H1, and B1. We also find that the largest barrier for diffusion along path (b) and (c) is ~ 1.5 eV. Therefore, N atoms would be trapped in the H6-sites at low temperature, while they may also occupy H1- and B1-sites at higher temperatures.

coverage (GML)		E_{bind} (eV)
1		2.35
2		2.20
3		1.89
4		1.54
5	Fig. 5.32(5a)	1.22
	Fig. 5.32(5b)	1.20
6		0.95

Table 5.12: Binding energies (referenced to $^1/_2\,N_2$) for oxygen on Re(13$\bar{4}$2) at different coverages; only the most stable structure for each coverage is listed (see Fig. 5.32).

Interestingly, two and three nitrogen atoms per unit cell give a low adsorbate density and therefore no N–N repulsion is found in these coverages. At 2 GML, a structure with nitrogen atoms at H1- and H6-sites (Fig. 5.32(2)) has the highest binding energy of 2.20 eV. This is very similar to the value of 2.21 eV obtained for $\bar{E}_{\mathrm{bind}}$. For 3 GML coverage, a structure where H9, H1, and H6-sites (Fig. 5.32(3)) are occupied is most stable. Here the binding energy of 1.89 eV is again very close to the value of 1.88 eV obtained for $\bar{E}_{\mathrm{bind}}$. Interaction between adsorbates becomes significant at Θ=4 GML. The binding energy of most stable configuration for this coverage (Fig. 5.32(4)) is 0.14 eV lower than $\bar{E}_{\mathrm{bind}}$=1.68 eV. The preferred configuration for 5 GML (Fig. 5.32(5a)) with a binding energy of 1.22 eV ($\bar{E}_{\mathrm{bind}}$=1.49 eV) shows an increasing N–N repulsion. The most stable structure obtained for the same coverage of O on this surface (Fig. 5.32(5b)) is now 0.02 eV less stable. Finally, at a coverage of 6 GML, a notable difference is obtained between E_{bind}=0.95 eV and $\bar{E}_{\mathrm{bind}}$=1.63 eV.

From Fig. 5.34 it can be clearly seen that the binding energy decreases with increasing N or O coverage. As mentioned in the previous section, there is a weak O–O repulsion for 2 GML $\leq \Theta \leq$ 4 GML. The interaction between nitrogen adatoms for Θ=2 and 3 GML is even much weaker. Therefore, the reduction in binding energy for the low coverages is mainly due to the energy differences between different occupied sites. The binding energy of N decreases slightly as the coverage is increased to Θ=2 GML and then it decreases rapidly (and almost linearly) by increasing the coverage up to Θ=6 GML. This trend is explained as follows. At 2 GML, besides already occupied H6-site, the second N atom populates H1-site, which is only 0.28 eV less stable than H6 while at $\Theta \geq$ 3 GML the additional N adsorbates have to occupy the remaining vacant positions that are considerably less favored compared to H1 and H6 (see Tab. B.19).

Furthermore, the drop in the adsorption energy is generally less significant for oxygen than for nitrogen. To explain this difference, we note that the energy differences of the various sites on Re(13$\bar{4}$2) are within 2.29 eV for N while they

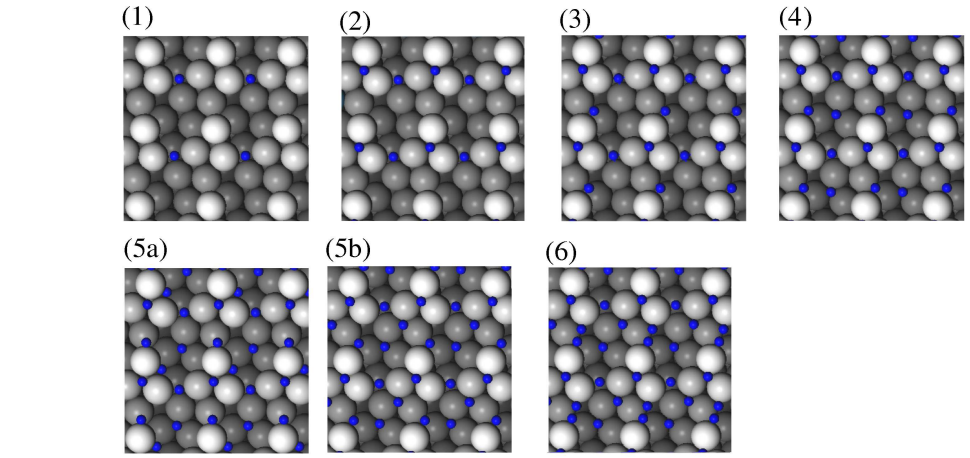

Figure 5.32: Top views of the most stable structures of nitrogen-covered Re(13$\bar{4}$2) in a (1×1) overlayer and different coverages: (1) 1 GML, (2) 2 GML, (3) 3 GML, (4) 4 GML, (5a and 5b) 5 GML, (6) 6 GML.

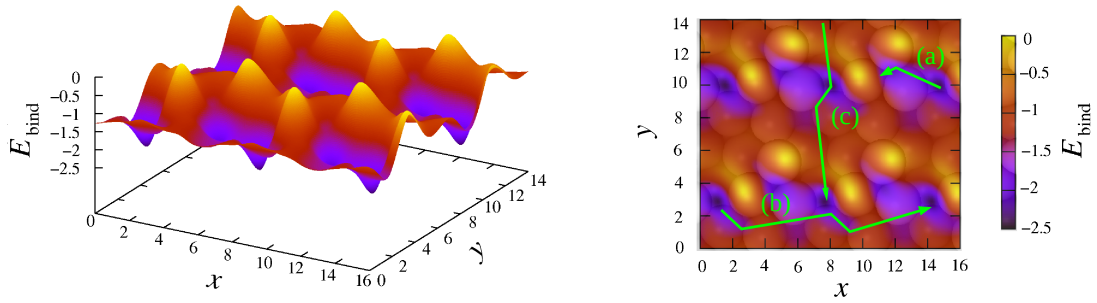

Figure 5.33: Adsorption energy distribution (in eV and referenced to $^1/_2\,N_2$) for binding 1 GML of atomic nitrogen onto Re(13$\bar{4}$2). X and y are given in Å. The arrows indicate different paths for N diffusion on the surface.

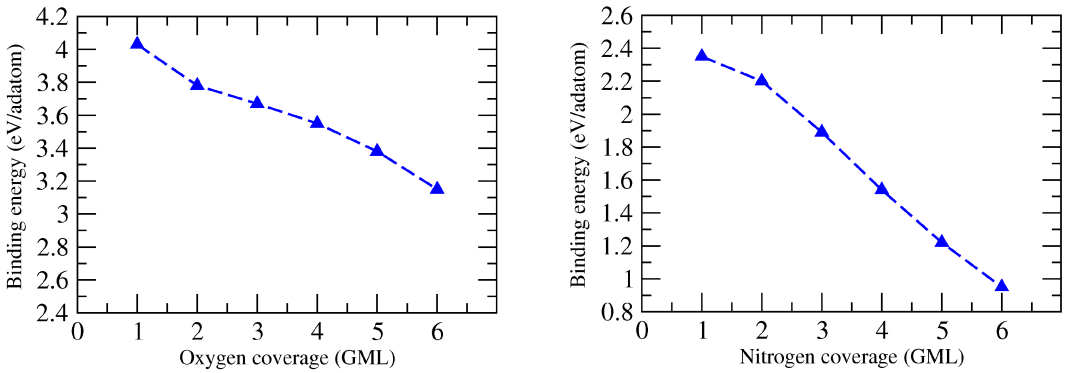

Figure 5.34: Binding energy (referenced to $^1/_2\,O_2$ and $^1/_2\,N_2$) as a function of oxygen (left) and nitrogen (right) coverage on Re(13$\bar{4}$2).

are within 1.65 eV for O. Therefore, with increasing coverage additional O atoms, accommodated further on Re(13$\bar{4}$2), pay smaller energetic penalty compared to N atoms for populating the remaining vacant positions.

5.5 Density of States of Adsorbate-covered Re Surfaces

In this section we will briefly compare in simple terms the binding energy of O or N in the Re(10$\bar{1}$0), (10$\bar{1}$1), (11$\bar{2}$1), and (13$\bar{4}$2) surfaces. For this purpose we analyzed ΔDOS, which is the difference between the density of states of the clean DOS(Re) and the adsorbate-covered surfaces DOS(Re + O)

$$\Delta\mathrm{DOS} = \mathrm{DOS}(\mathrm{Re}_{5d} + \mathrm{O}_{2p}) - \mathrm{DOS}(\mathrm{Re}_{5d}), \tag{5.3}$$

as well as the projected density of states of Re and O atoms for the oxygen-covered surfaces. Similar plots were also obtained for nitrogen adsorption. The results are presented in Figs. 5.35 and 5.36. Since we have chosen the structures with the low coverage of O or N, the adsorbate–adsorbate interaction is expected to be small.

According to the qualitative picture of binding, the overlapping adsorbate–substrate orbitals are split into bonding and antibonding levels. For each system, a large ΔDOS peak due to bonding states is observed below the Fermi level (at $\sim$–7 to –5 eV). The other smaller ΔDOS peaks, positioned above the bonding feature, in which there is an overlap between the Re 5*d* and O or N 2*p* orbitals might be due to the antibonding states.

As can be seen from Fig. 5.35, differences in the ΔDOS (and PDOS) plots between the O-covered Re(10$\bar{1}$0), (10$\bar{1}$1), and (13$\bar{4}$2) surfaces are difficult to identify, showing that the strength of the covalent bonding between O and Re atoms is similar for these orientations. This qualitative conclusion is in agreement with the results obtained in the previous sections, where we found that the variation in the binding energy of O on Re(10$\bar{1}$0), (10$\bar{1}$1), and (13$\bar{4}$2) is within 0.27 eV (7 %). Compared to these three systems, for O/Re(11$\bar{2}$1) we see that although the bonding peak is closer to the Fermi level, the overlap between Re 5*d* and O 2*p* orbitals is larger. Therefore, in this qualitative description, it is difficult to judge whether or not oxygen binding is stronger in Re(11$\bar{2}$1) than in other surfaces.

Interestingly, it can be seen that the Re 5*d* peaks are larger for the O/Re(11$\bar{2}$1) surface in which O occupies a two-fold site than for the other surfaces with O atom sitting on a three-fold hollow site. The Re 5*d* peaks are almost similar for O/Re(10$\bar{1}$0), O/Re(10$\bar{1}$1), and O/Re(13$\bar{4}$2).

In case of N adsorption (see Fig. 5.36), the bonding level is located somewhat deeper (in energy) for Re(13$\bar{4}$2) and (10$\bar{1}$1) than for Re(10$\bar{1}$0) and (11$\bar{2}$1). In addition, on the latter surfaces we observe a weak accumulation (ΔDOS) peak

at $\sim$ –3.2 eV, where there is an overlap of Re 5*d* and N 2*p* states, which may be attributed to the occupied antibonding states.Therefore, these results are in agreement with the calculated adsorption energies in the previous sections that showed stronger interaction of adsorbate with substrate for Re(13$\bar{4}$2) and (10$\bar{1}$1) compared to two other surfaces. Furthermore, the size of the bonding peak is slightly larger in N/Re(13$\bar{4}$2) compared to N/Re(10$\bar{1}$1), indicating a higher adsorption energy for the former system. In addition, the PDOS plots show that the Re 5*d* peaks are larger for N/Re(10$\bar{1}$0) and N/Re(11$\bar{2}$1) than for N/Re(10$\bar{1}$1) and N/Re(13$\bar{4}$2), reflecting higher coordinated adsorption sites on the latter surfaces.

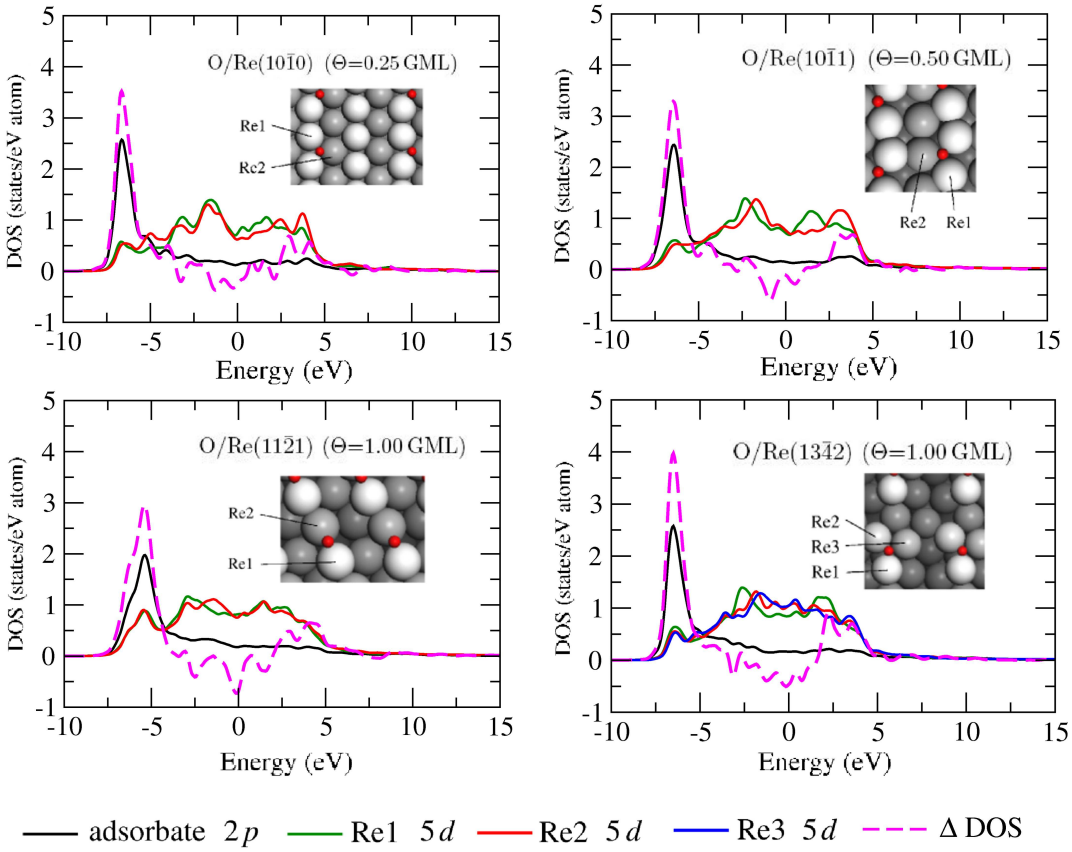

Figure 5.35: ΔDOS and PDOS for O-covered Re surfaces. The energy zero shows the Fermi level.

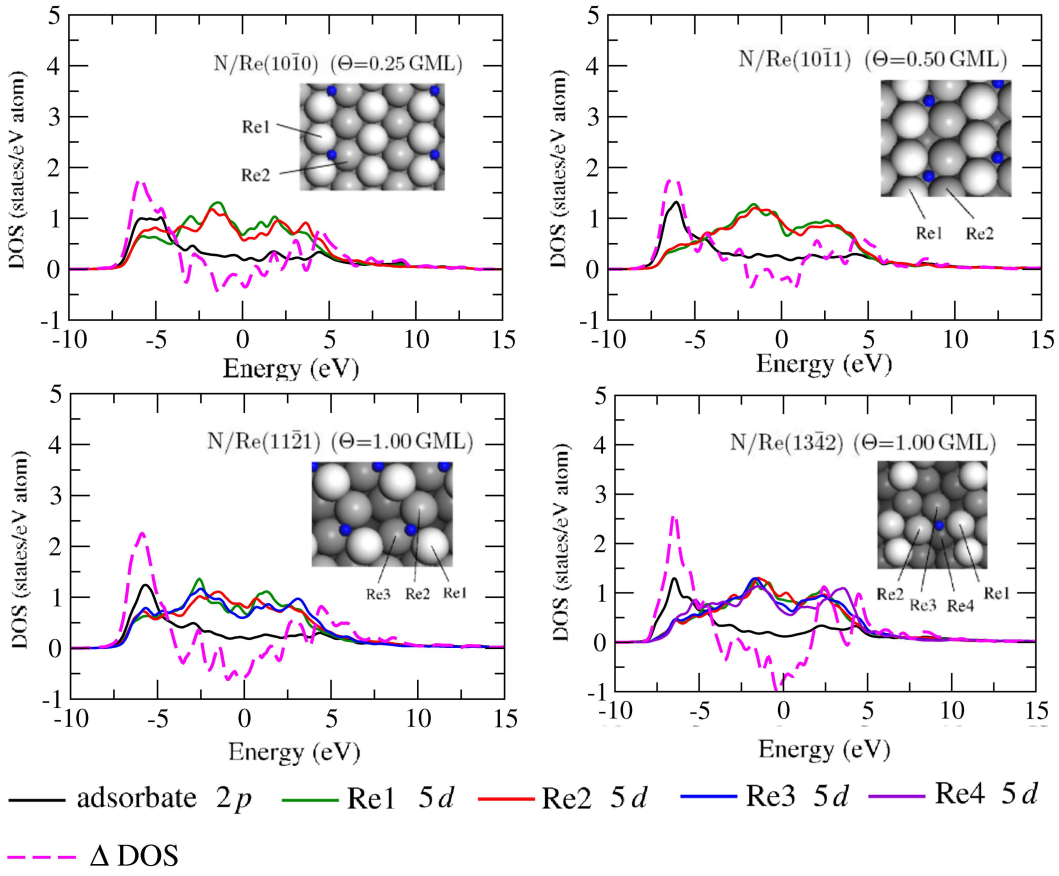

Figure 5.36: ΔDOS and PDOS for N-covered Re surfaces. The energy zero shows the Fermi level.

Chapter 6

Faceting of Re Surfaces

In the previous chapter, DFT calculations on the interactions between oxygen or nitrogen and different Re surfaces were described. So far we did not take into account the effects of temperature and pressure of the surrounding oxygen or nitrogen atmosphere, which are expected to influence the overall surface stabilities. In this chapter, we construct phase diagrams of Re surface structures in the (p, T)-space by employing the *ab initio* atomistic thermodynamics approach as described in Section 2.7.1.

The energies for the most stable configurations for each coverage of O or N on Re(10$\bar{1}$0), Re(10$\bar{1}$1), Re(11$\bar{2}$1), and Re(13$\bar{4}$2) (see Chapter 5) are used to evaluate the surface free energies as defined by eq. (2.51). As mentioned before, since the temperature and pressure dependence of solid phases (surfaces and bulk) is expected to be small compared to those of gaseous phases, we can approximate the Gibbs free energies of the solid phases by the corresponding DFT-calculated total energies. The surface phase diagrams are constructed by plotting the surface free energies as function of the chemical potential of the corresponding gaseous species referenced by $\Delta\mu_x^{\text{gas}} = \mu_x^{\text{gas}} - 1/2E_{x_2}^{\text{tot}}$ (x = O or N). In order to allow for a better comparison with experimental results, we use eq. (2.52) to convert the chemical potential of the surrounding gas to a temperature scale for the partial pressure at which the corresponding experiments have been conducted.

Plotting the surface free energy of a particular structure versus the chemical potential of the surrounding gas phase yields a straight line. Since the slope of these lines is proportional to the number of adsorbate, increasing the coverage leads to an increase of the slope of the line. The most relevant surface structures are then characterized by the lowest lying-line (lowest surface free energy). The stability range of phases is determined by the crossing points between these lines. If we convert the chemical potentials of these crossing points to temperatures and pressures by using eq. (2.52), an alternative plot is obtained, which shows the (p, T)-conditions under which most favorable structures can form.

In the following sections, we proceed to the investigation of the full phase di-

agrams for oxygen and nitrogen-induced faceting of Re(11$\bar{2}$1). In the case of oxygen adsorption, experimental results (see Section 3.1) show that the faceted structures are four-sided pyramids, consisting of (10$\bar{1}$0) and (10$\bar{1}$1) facets. While O-covered Re(10$\bar{1}$1) has experimentally not been studied in detail, there are two reports on the oxygen adsorption on planar Re(10$\bar{1}$0) (see Chapter 3), indicating that, depending on (p, T)-conditions and oxygen exposure, O adsorption leads to the formation of (1×3) overlayer on Re(10$\bar{1}$0) or facets parallel to the (10$\bar{1}$1) plane. Therefore, here we first generate the corresponding phase diagram for oxygen-induced changes in surface morphology of planar Re(10$\bar{1}$0) and make a comparison with experimental observations. This helps us to understand the influence of the Re(10$\bar{1}$0) faces on the stability of pyramidal facets. Afterwards we will focus on the phase diagrams for surface faceting on Re(11$\bar{2}$1) in the presence of an O or N atmosphere.

6.1 Surface Phase Diagram of O/Re(10$\bar{1}$0)

By using eq. (2.51) together with the DFT-calculated total energies, we obtained the surface phase diagram for O/Re(10$\bar{1}$0) (Fig. 6.1), where the surface stabilities γ are plotted versus the chemical potential of the surrounding oxygen. Here, we distinguish between clean and oxygen-covered surfaces of:

- unreconstructed Re(10$\bar{1}$0)-(1×1);
- reconstructed Re(10$\bar{1}$0)-(1×2) and -(1×3);
- two-sided ridge-like structures with (10$\bar{1}$1) and (01$\bar{1}$1) faces.

These surfaces have been already discussed in Sections 5.2 and 5.3. The surface free energies for the faceted surface were projected onto the planar surface by using the left side of eq. (2.64) with ϑ^{geo}=25.47°.
Since our focus is on oxygen adsorption on pure Re, the phase diagram is valid in the oxygen chemical potential range, where the bulk oxide is not stable. To evaluate this condition, we refer to Section 4.1.3 where the heat of formation of ReO_2 was calculated to be –2.24 eV per oxygen.
Fig. 6.1 indicates that at low oxygen chemical potentials the clean unreconstructed Re(10$\bar{1}$0)-(1×1) surface (see Fig. 6.2(a)), represented by a horizontal line, is thermodynamically stable. Increasing the oxygen chemical potential results in the formation of a c(2×4)-2O overlayer on unreconstructed Re(10$\bar{1}$0)-(1×1) (see Fig. 6.2(b)) between $\Delta\mu_{\text{O}} = -3.67$ and -3.56 eV. Further increase of the oxygen chemical potential up to –1.85 eV does not change the preferred substrate structure but increases the coverage of the adlayer (see Figs. 6.2(c)-(d′)). Interestingly, for $\Delta\mu_{\text{O}} \geq$ –1.85 eV, the (1×3)-6O overlayer on the reconstructed Re(10$\bar{1}$0)-(1×3)

triple MR surface (see Figs. 6.2(e) and (e′)) becomes stable. The surface phase diagram makes also apparent that two-sided ridge-like structures with (10$\bar{1}$1) and (01$\bar{1}$1) faces are not favorable at any oxygen chemical potential. Finally, from a thermodynamic viewpoint ReO_2 bulk-oxide should form at the oxygen chemical potentials of $\Delta\mu_O \geq -2.24\,eV$.

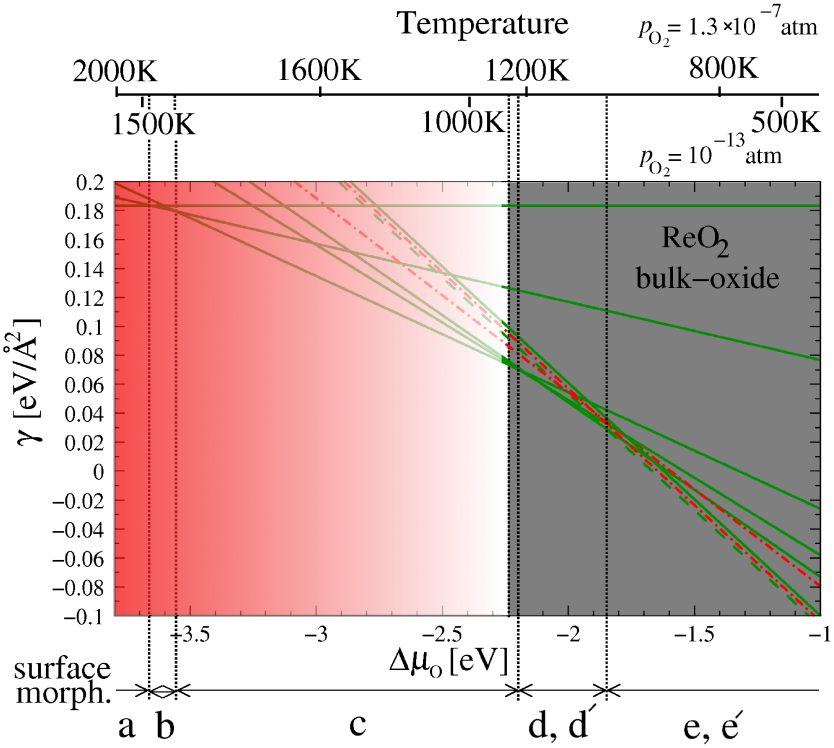

Figure 6.1: Surface phase diagram for O adsorption on Re(10$\bar{1}$0) showing the surface free energy as function of the oxygen chemical potential referenced as $\Delta\mu_O = \mu_O - \frac{1}{2}E^{tot}_{O_2}$. The labels a–e′ refer to the surface structures of Fig. 6.2.

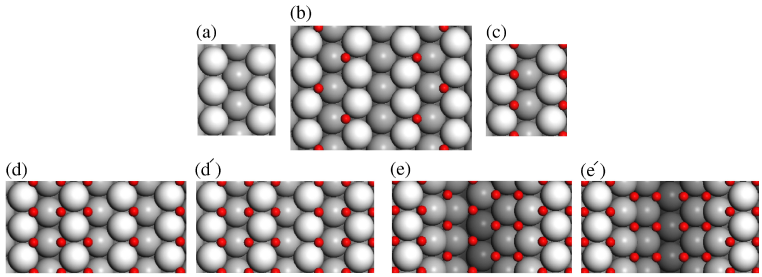

Figure 6.2: The surface structures for the stable phases of the O/Re(10$\bar{1}$0) phase diagram presented in Fig. 6.1: (a) clean Re(10$\bar{1}$0)-(1×1), (b) c(2×4)-2O overlayer on Re(10$\bar{1}$0)-(1×1), (c) (1×1)-1O overlayer on Re(10$\bar{1}$0)-(1×1), (d) (1×3)-4O overlayer on Re(10$\bar{1}$0)-(1×1), (d′) (1×2)-3O overlayer on Re(10$\bar{1}$0)-(1×1), (e) and (e′) (1×3)-6O overlayer on Re(10$\bar{1}$0)-(1×3) triple MR. The layers are indicated more dark with increasing depth.

In order to allow for a better comparison with experiment, the oxygen chemical potential has been converted to temperature scales for oxygen partial pressures of 1.3×10^{-7} and 10^{-13} atm as used experimentally by Zehner *et al.* [63] and Lenz *et al.* [64], respectively. It can be seen that at an oxygen partial pressure of 1.3×10^{-7} atm (10^{-13} atm) no oxygen is adsorbed on the surface for $T \geq 1950$ K ($T \geq 1500$ K). This high desorption temperature is directly related to the rather strong binding energy of oxygen to Re(10$\bar{1}$0) (3.79 eV per $^1/_2$ O_2). Since entropy contributions that have been neglected here might become relevant as temperature rises, we expect a qualitative understanding of the stability of phases from the phase diagram at high temperature regions (shown by red color in Fig. 6.1). Therefore, in the following we will focus on the stability of phases at lower temperatures.

At oxygen partial pressures of 1.3×10^{-7} atm and T=1300 K, a (1×1) adlayer with a coverage of 1 GML adsorbed on the unreconstructed Re(10$\bar{1}$0)-(1×1) surface (Fig. 6.2(c)) has the lowest surface free energy. At this temperature the stability difference between this structure and (1×3)-4O as well as (1×2)-3O (see Figs. 6.2(d) and (d′)) is rather small (5–8 meV/Å^2). Therefore, according to our phase diagram the (1×3) adlayer proposed by Zehner *et al.* at temperatures higher than 1298 K at a pressure of 1.3×10^{-7} atm may exist as a meta-stable phase. Fig. 6.1 also shows that for 1220 K $\geq T \geq$ 1040 K there might be a coexistence of the (1×3)-4O and (1×2)-3O adlayers on still unreconstructed Re(10$\bar{1}$0)-(1×1). Finally, at $T \leq$ 1040 K, the reconstructed Re(10$\bar{1}$0)-(1×3) triple MR structures presented in Figs. 6.2(e) and (e′) appear to be thermodynamically stable. The oxygen coverage on these systems, which have very similar surface free energies ($\Delta\gamma$=0.6 meV/Å^2), is 2 GML. Although the surface free energy of the triple MR surface was considerably larger compared to the unreconstruted surface in the clean state, we find that the former structure becomes more stable by ~ 8 meV/Å^2 when being covered with 2 GML oxygen. As discussed in Section 4.2.2, the triple MR structures can be viewed as {10$\bar{1}$1} microfacets at the (10$\bar{1}$0) surface. Interestingly, this kind of facets has been proposed by Zehner *et al*. at temperatures of 888 K or higher at p_{O_2}=1.3× 10^{-7} atm. In their experiments they were not able to determine the size of these facets. Our calculations indicate that the infinitely large facets with {10$\bar{1}$1} faces do not appear as stable phases, but {10$\bar{1}$1} microfacets, exposing three Re layers, could form. Therefore, Re(10$\bar{1}$0)-(1×3) triple MR is stabilized at high coverages because additional O atoms most probably prefer binding at the edges of the troughs of this structure.

According to our calculations ReO_2 bulk-oxide (having a orthorhombic structure) is thermodynamically stable below 1240 K[1]. Thus, the experimentally observed

[1]Unfortunately, we are not able to compare our theoretical decomposition temperature of ReO_2 with reported measurements. Although experimental studies by Magnéli [85] showed that this structure is stable in the temperature range of 573–1323 K, later, it was suggested that the thermal decomposition of ReO_2 undergoes the following disproportionation reaction $7\,ReO_2(s) \longleftrightarrow 3\,Re(s)+2\,Re_2O_7(g)$ [113–116].

{10$\bar{1}$1} facets for $T \geq 888\,\mathrm{K}$ might be due to kinetic limitations in the formation of ReO_2 bulk-oxide.

In comparison with the experimental results by Lenz *et al.* [64], who have proposed the (1×3)-2O overlayer, we find the triple MR surface with a (1×3)-6O structure to be the most stable in the phase diagram for $T < 780\,\mathrm{K}$ at the experimentally used oxygen partial pressure of p_{O_2}=10^{-13} atm. Although they have not reported the temperature range at which an (1×3)-2O overlayer was observed, it was stated that (1×3)-2O forms after annealing the system to $520\,K < T < 650\,\mathrm{K}$, which lies in the temperature range where the (1×3)-6O structure on the triple MR surface is the most favorable.

In order to investigate the sensitivity of our results on choosing a different xc-functional, we additionally calculated the most relevant surface structures with the LDA functional and generated the equivalent surface phase diagram. Fig. 6.3 shows the stability range of different phases with respect to the temperature and pressure evaluated using the PBE and LDA functional. It can be seen that although with the LDA functional all phase transitions are shifted towards higher temperatures (by 200–250 K), the overall phase ordering and therefore the conclusions drawn above remain unchanged.

In conclusion, we could show that adsorption of atomic oxygen at a coverage of 2 GML leads to a stabilization of the (1×3) missing-row-type reconstruction, being comparable to a nanofaceted surface exposing (10$\bar{1}$1) faces. At this coverage, we find an O adlayer with a (1×3) periodicity on the Re(10$\bar{1}$0)-(1×3) triple MR surface. Therefore, our results are consistent with the experimentally observed {10$\bar{1}$1} facets and also the (1×3) overlayer on the Re(10$\bar{1}$0) surface.

In the next section, we use the energies of the most stable structures for O/Re(10$\bar{1}$0) to plot the full phase diagram of oxygen-induced faceting of Re(11$\bar{2}$1).

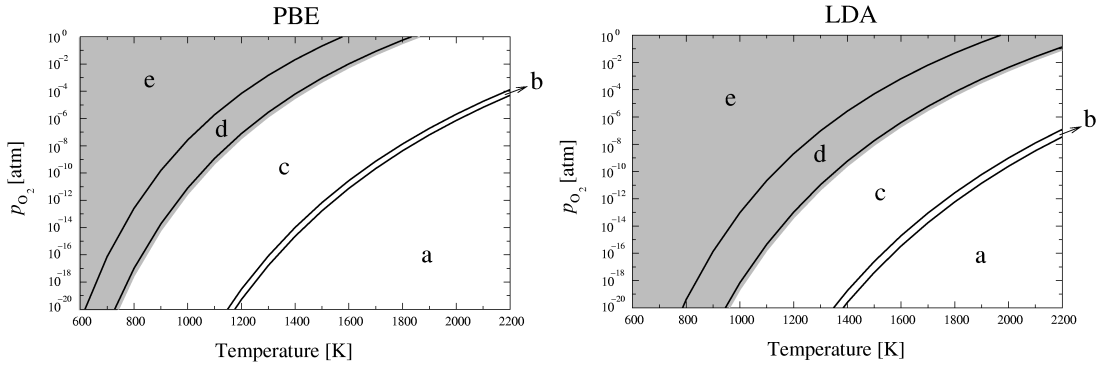

Figure 6.3: Surface phase diagrams for the Re(10$\bar{1}$0) surface in contact with an O gas phase for the PBE and LDA exchange–correlation functional.

6.2 Surface Phase Diagram of O and N/Re(11$\bar{2}$1)

The surface free energies for the faceted surfaces were calculated using the left side of eq. (2.64) with the parameters for the partial surface areas and facet tilt angles summarized in Tab 4.4. Each summand of this equation was evaluated by using eq. (2.51) together with the DFT-calculated total energies, which were obtained in the previous chapter. In our calculations we used geometrical coverages Θ in GML, which are the number of adsorbed O/N atoms per (1×1) unit cell, thus varying with surface orientation. In comparison, experiments used physical coverages (PML), where surface saturation is achieved with 1 monolayer (ML). Unfortunately, there are no direct measurements of saturation coverages on Re(11$\bar{2}$1); but using the highest possible oxygen/nitrogen coverage phases from our calculated phase diagrams (prior to forming the corresponding bulk compounds) to define saturation coverage, we obtain an atom density on Re(11$\bar{2}$1) of 1.33×10^{15} atoms/cm^{-2} for oxygen and 0.89×10^{15} atoms/cm^{-2} for nitrogen. The former value is in good agreement with the available experimental value of 1.32×10^{15} atoms/cm^{-2} for stepped Re(0001) at 350 K [117]. Finally, this leads to the following approximate conversion between geometrical (GML) and physical monolayers (PML) for the Re(11$\bar{2}$1) substrate: 3 GML-O≡1 PML-O and 2 GML-N≡1 PML-N.
Figs. 6.4 and 6.5 show the surface phase diagrams including clean and oxygen/nitrogen-covered planar or fully faceted surfaces of:

- the flat Re(11$\bar{2}$1) substrate;
- two-sided ridge-like structures with (13$\bar{4}$2) and (31$\bar{4}$2) faces;
- nanopyramids exposing (01$\bar{1}$0), (10$\bar{1}$0), (01$\bar{1}$1), and (10$\bar{1}$1) faces.

Any partially-faceted surface structure, such as the zig-zag chains with (11$\bar{2}$1) and (10$\bar{1}$0) faces observed by STM after oxygen adsorption (see Section 3.1), were not considered in the phase diagram since these do not represent thermodynamically stable surface phases.
The phase diagram generated for oxygen-induced faceting of Re(11$\bar{2}$1) (Fig. 6.4) shows that, above 1800 K and at the experimentally used oxygen partial pressure of $p_{O_2} = 5 \times 10^{-10}$ atm, desorption of oxygen should occur. This high temperature is related to the strong binding energy of oxygen to the Re(11$\bar{2}$1) surface (3.85 eV per $^1/_2\,O_2$) and is consistent with the experimental observation that oxygen desorption starts at $T > 1300$ K. Despite this qualitative agreement, further discussion is omitted here since at these rather high temperatures entropy contributions that have been neglected for the adsorbed atoms might affect any conclusion obtained from the phase diagram. At lower temperatures ($T \leq 1130$ K) oxygen-covered two-sided ridges with Re(13$\bar{4}$2) and Re(31$\bar{4}$2) faces as well as

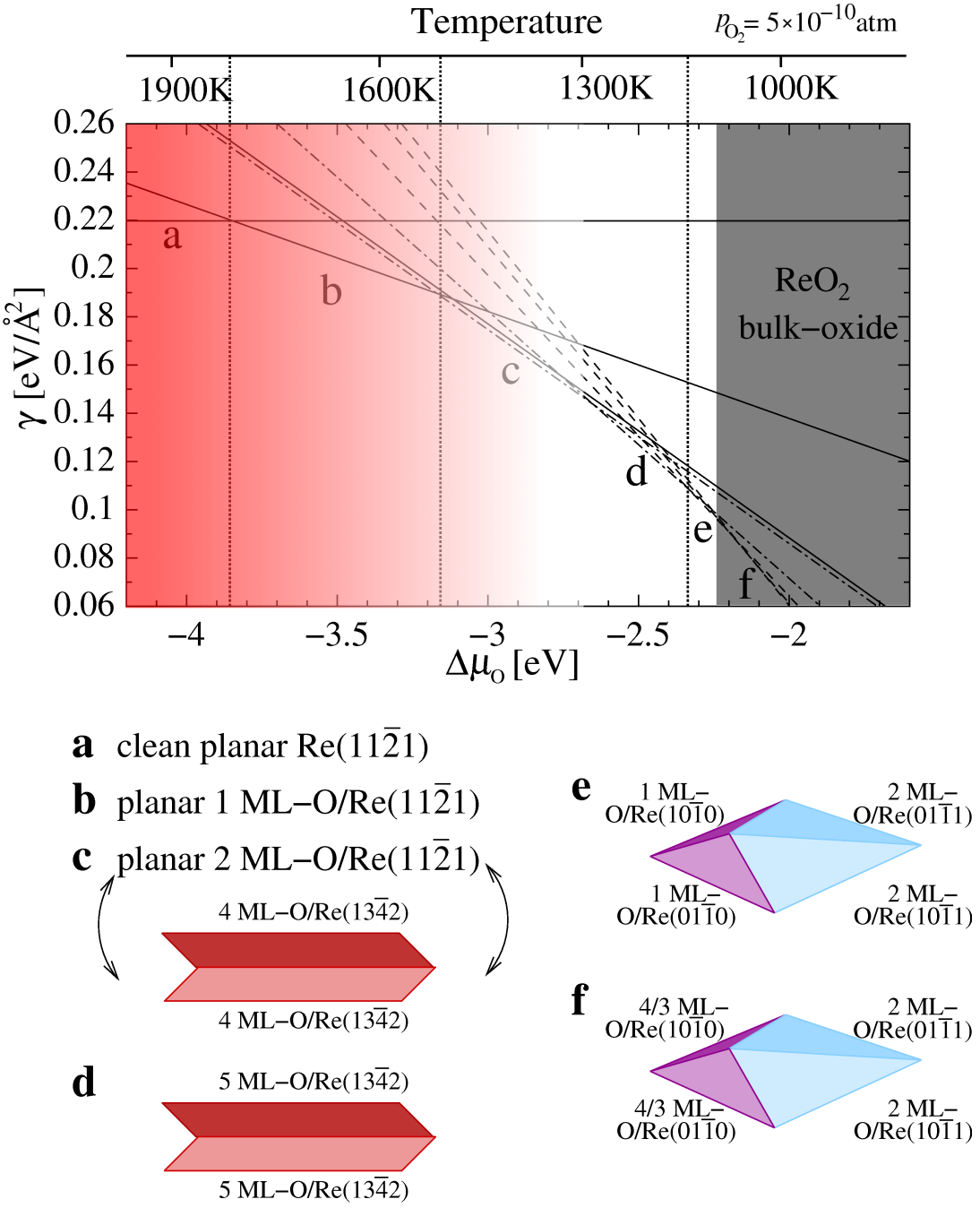

Figure 6.4: Surface phase diagram for O-induced faceting of planar Re(11$\bar{2}$1) showing the surface free energy as function of the oxygen chemical potential referenced as $\Delta\mu_O = \mu_O - \frac{1}{2}E^{tot}_{O_2}$. In order to distinguish between the surface morphologies, the solid, dot-dashed, and dashed lines represent the planar substrate, two-sided ridges, and four-sided pyramids, respectively.

the four-sided nanopyramids with $(01\bar{1}0)$, $(10\bar{1}0)$, $(01\bar{1}1)$, and $(10\bar{1}1)$ faces show comparable surface free energies, deviating by 2–3 meV/Å^2, which is within the accuracy of our calculations. While according to the phase diagram the oxygen coverage on Re$(13\bar{4}2)$ and Re$(31\bar{4}2)$, forming the two-sided ridges, is 5.0 GML (0.83 PML on the substrate), in case of the four-sided pyramids both $(01\bar{1}1)$ and $(10\bar{1}1)$ faces are covered with 2.0 GML oxygen and both $(01\bar{1}0)$ and $(10\bar{1}0)$ faces with 1.0 GML. The latter pyramids were also observed by experiments at 900 K (see Fig. 3.3). At this temperature the energy difference between the four-sided pyramids and the two-sided ridges becomes more pronounced (see Fig. 6.4) with a clear favor for the four-sided nanopyramids. However, according to our calculations ReO_2 bulk-oxide becomes thermodynamically stable already below 1100 K. Thus, the experimentally observed structure at 900 K might represent a metastable phase possibly stabilized due to kinetic limitations in the formation of ReO_2 bulk-oxide.

Regarding the morphology of the oxygen-induced four-sided nanopyramids, LEED studies showed that the $(01\bar{1}1)$ and $(10\bar{1}1)$ faces seem to be (1×2) reconstructed (see Section 3.1). Although in the theoretical phase diagram (Fig. 6.4) the four-sided facets are based on unreconstructed $(01\bar{1}1)$ and $(10\bar{1}1)$ faces, our calculations show that at high adsorbate coverages the reconstructed O/Re$(10\bar{1}1)$-(1×2) surface with a missing-row structure that has been studied in Section 5.3.2 has a comparable surface energy as unreconstructed O/Re$(10\bar{1}1)$-(1×1). Therefore, our calculations qualitatively support the experimental observation of four-sided nanopyramids exhibiting (1×2)-reconstructed $(01\bar{1}1)$ and $(10\bar{1}1)$ faces.

Prior to discussing the results for N/Re$(11\bar{2}1)$, we should mention that experimentally N was deposited on Re$(11\bar{2}1)$ using gaseous NH_3, whereas our phase diagram is based on adsorption of nitrogen from N_2. The assumption of a thermodynamic equilibrium with a N_2 atmosphere is justified by the fact that all nitrogen atoms desorbing from the Re surfaces combine to N_2.

Figure 6.5 shows that, at nitrogen partial pressures of $p_{N_2} = 5 \times 10^{-10}$ atm and $T \geq 1080$ K, no nitrogen is adsorbed on the surface. This temperature is in agreement with the experimental value of 1100 K for desorption of nitrogen from the surface, which according to our calculations should be planar Re$(11\bar{2}1)$. For comparison, clean facets of two-sided ridges and four-sided nanopyramids (see Section 4.2.6) are less stable by 5 and 14 meV/Å^2, respectively. As soon as nitrogen adsorbs below 1080 K, facets become the thermodynamically preferred phase (see Fig. 6.5). As observed experimentally, the stabilized nano-facets are two-sided ridges, combining Re$(13\bar{4}2)$ and Re$(31\bar{4}2)$ faces. For the rather large temperature range of 1080 K $> T >$ 280 K these nanofacets are significantly more stable than nitrogen-covered planar Re$(11\bar{2}1)$ or four-sided nanopyramids with $(01\bar{1}0)$, $(10\bar{1}0)$, $(01\bar{1}1)$, and $(10\bar{1}1)$ faces. The latter structure should, from a thermodynamic viewpoint, form below 280 K and above the temperature where a potential Re-nitride becomes stable, however, at these low temperatures the kinetic energy for overcoming possible barriers is rather low. Experimental ob-

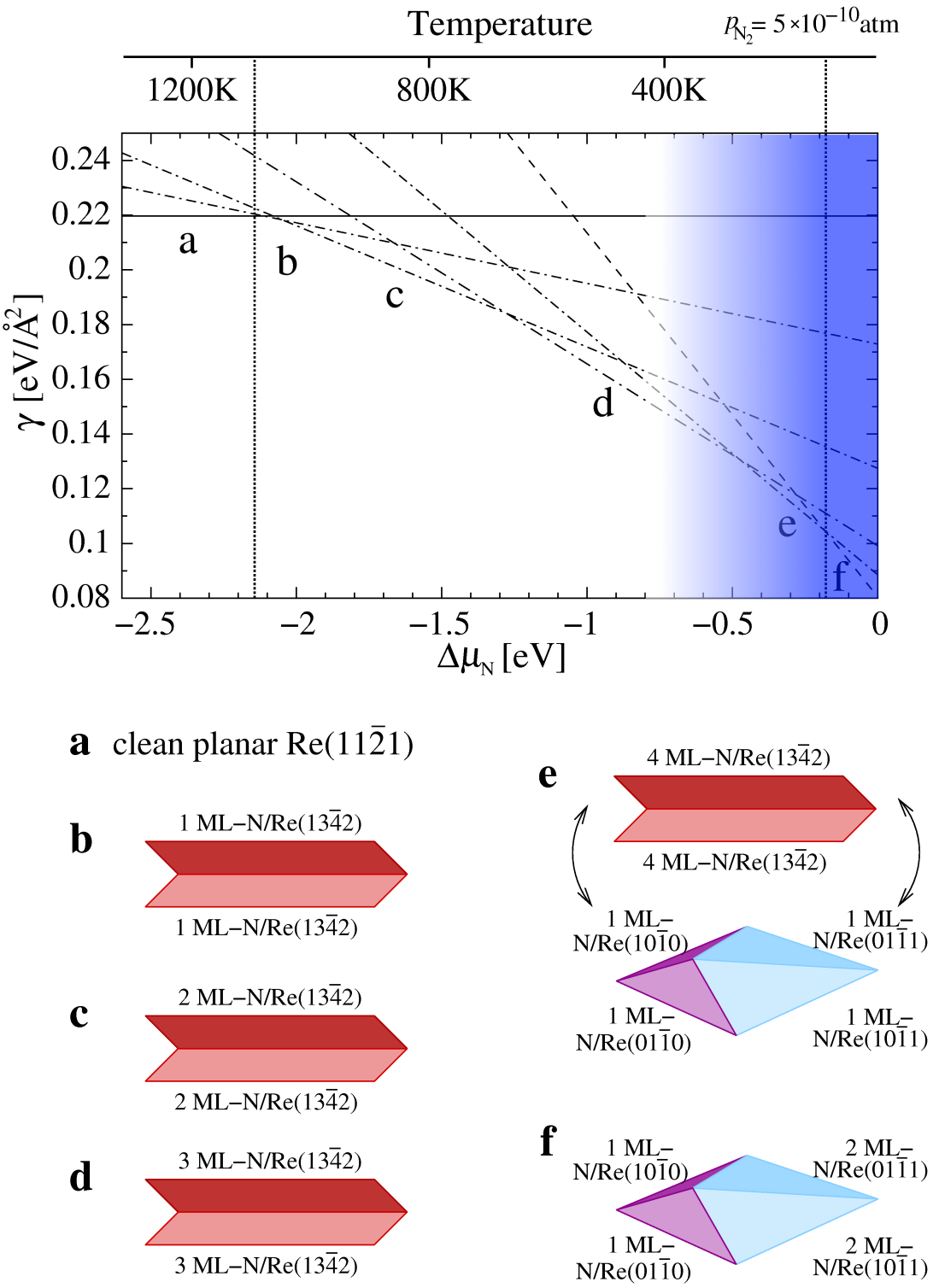

Figure 6.5: Surface phase diagram for N-induced faceting of planar Re(11$\bar{2}$1) showing the surface free energy as function of the nitrogen chemical potential referenced as $\Delta\mu_N = \mu_N - \frac{1}{2}E^{tot}_{N_2}$. In order to distinguish between the surface morphologies, the solid, dot-dashed, and dashed lines represent the planar substrate, two-sided ridges, and four-sided pyramids, respectively.

servations proposed that the facets start to form when the nitrogen coverage is larger than 0.4–0.5 PML at 5×10^{-10} atm and temperatures above 700 K. Under these conditions the phase diagram shows phase c, which has 2 GML of nitrogen on each face, to be thermodynamically stable. Projecting this coverage onto the Re(11$\bar{2}$1) substrate would lead to 1 GML, which converts to 0.5 PML, being in good agreement with the experimental value. Lowering the temperature (at fixed pressure) does not cause the surface morphology to change, but leads to an increase of the nitrogen coverage on the ridges. Although at lower temperatures one would expect a bulk Re-nitride to become thermodynamically stable, but, as mentioned in Section 4.1.4, such a stable compound cannot be obtained directly from the elements [87]. Therefore we only shaded the high $\Delta\mu_N$-range in the phase diagram.

Figs. 6.6 and 6.7 show the stability of different phases with respect to the temperature and pressure evaluated using the PBE and the LDA exchange–correlation functionals. Similar to the case of the O/Re(10$\bar{1}$0), the overall phase ordering and therefore the conclusions drawn above remain unchanged when using LDA functional.

In conclusion, we could reproduce the experimentally observed surface faceting of Re(11$\bar{2}$1) and also provide quantitative information and physical insights into the morphological changes of the facets with adsorbate, adsorbate coverage, and annealing temperature. We could show that, by choosing an appropriate adsorbate and environmental temperature and pressure conditions, Re(11$\bar{2}$1) could be fully faceted with either two-sided ridges or four-sided pyramids.

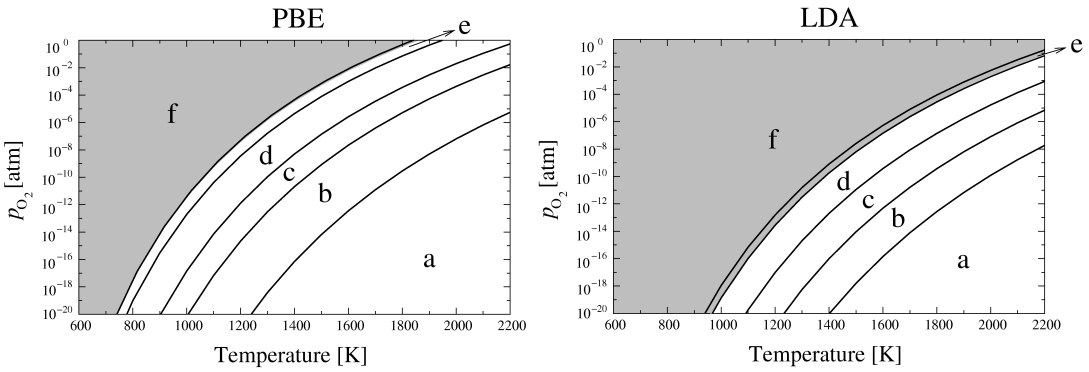

Figure 6.6: Surface phase diagrams for the Re(11$\bar{2}$1) surface in contact with an O gas phase for the PBE and LDA exchange–correlation functional.

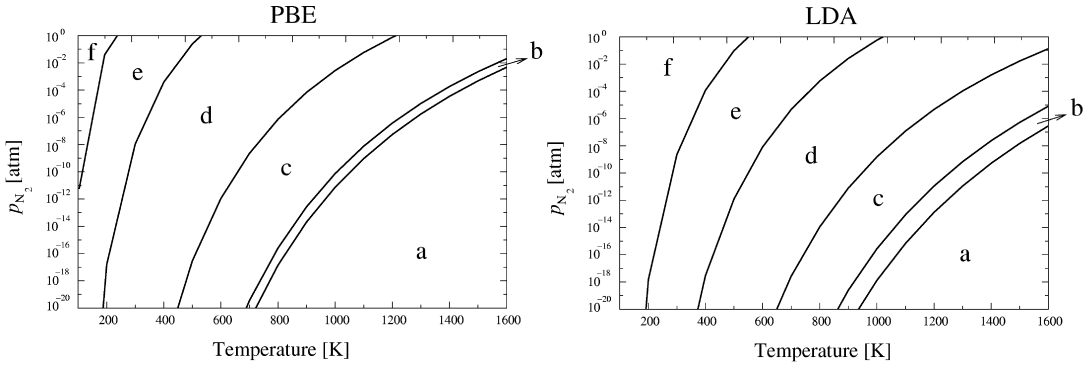

Figure 6.7: Surface phase diagrams for the Re(11$\bar{2}$1) surface in contact with a N gas phase for the PBE and LDA exchange–correlation functional.

Chapter 7

Faceting of Ir(210)

7.1 Experimental Observations

As mentioned in Chapter 3, when atomically-rough Ir(210) is covered with more than a 0.5 physical ML (PML) of oxygen and annealed to 600 K, pyramidal facets develop on the initially planar surface [14,22]. LEED and STM (Fig. 7.1(a)) revealed that these facets, which completely covered the surface, expose faces of Ir(311), Ir(31$\bar{1}$), and Ir(110). Furthermore, the higher resolution STM-image 7.1(b) showed that, while the (311) and (31$\bar{1}$) faces are always unreconstructed, some (110) faces are partially reconstructed. This superstructure was proposed to be a "stepped double-missing-row"-(110) surface [65].

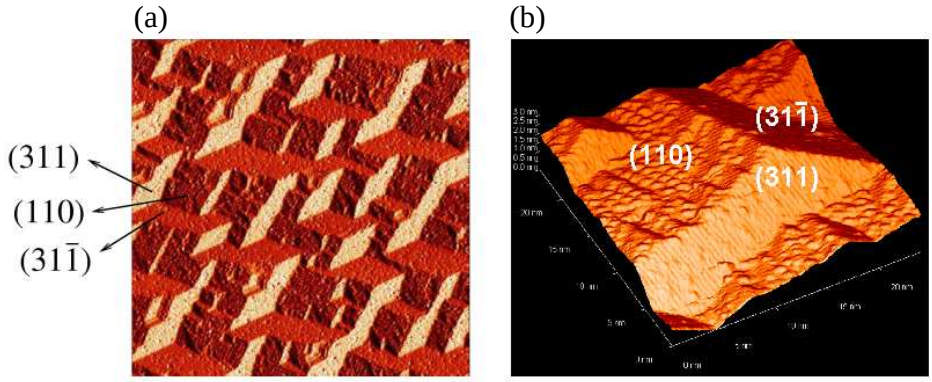

Figure 7.1: (a) STM derivative image (1000 Å×1000 Å) of O-covered faceted Ir(210) prepared by flashing Ir(210) in O_2 (5×10^{-8} Torr) to $T > 1700$ K and subsequent cooling it in O_2 to 300 K. Following a flash annealing in O_2, facets form as the crystal cools below $\sim$ 1150 K. (b) STM scan (240 Å×240 Å) of one pyramid of O-covered faceted Ir(210), showing the superstructure on the (110) facet. From ref. [23].

7.2 Oxygen-covered Ir Surfaces

In this section we discuss the adsorption of oxygen on the different surfaces that are involved in the facet formation, separately (Ir(210), (311), (110), and (110)-superstructure; see Figs. 7.2, 7.4–7.6); these were all generated on the basis of the calculated lattice constant of 3.90 Å (exp. [77]: 3.84 Å).
In order to calculate the total energies of different surface structures, which are required to draw the full (p, T)-surface phase diagram, similar to the case of Re(11$\bar{2}$1) we performed DFT slab calculations using the CASTEP code [71] with Vanderbilt-type ultrasoft pseudopotentials [49] and the generalized gradient approximation (GGA) exchange–correlation functional proposed by Perdew, Burke, and Ernzerhof (PBE) [44].
Layer-converged supercells consisting of 16-layer slabs for Ir(210), 11-layer slabs for Ir(311), 12-layer slabs for Ir(110), and 7-layer slabs for Ir(110)-superstructure were used to model oxygen adsorption with different coverages and adlayer structures. To decouple the interactions between neighboring slabs in the supercell geometry, repeated slabs were separated by a ∼12 Å vacuum. For Ir(210), Ir(311), and Ir(110)-superstructure, the bottom three layers and, for Ir(110), the bottom four layers were fixed at the calculated bulk structure, and the geometry of the remaining layers plus adsorbates was fully optimized (to $< 0.03\,\mathrm{eV/Å}$). The Brillouin zones of the (1×1) surface unit cells of Ir(210), (311), (110), and (110)-superstructure were sampled with 10×8, 14×8, 14×10, and 4×4 Monkhorst–Pack **k**-point meshes, respectively. Finally, a plane-wave basis set with an energy cutoff of 340 eV was used.
Investigating the error sources related to slab thickness, vacuum size, plane-wave cutoff, and **k**-point mesh, we found the maximum overall error bar in the surface free energy to be $< 5\,\mathrm{meV/Å^2}$ when using optimized values for each parameter.
The resulting binding energies are then used to generate the corresponding surface phase diagram for which we used the facet tilt angles (ϑ_f) and partial contributions to each pyramidal-shaped facet (S_f) as summarized in Tab. 7.1. Regarding the facets, two configurations are distinguished: (i) nanopyramids with (311), (31$\bar{1}$), and (110) regular faces, and (ii) and nanopyramids with (311), (31$\bar{1}$), and (110) superstructure faces, which both have been observed experimentally.
For our calculations, we use again geometrical coverages Θ in GML, which are defined as the number of adsorbed oxygen atoms per (1×1) unit cell (see Figs. 7.2, 7.4–7.6) and vary with surface orientation. These are different than physical coverages often used experimentally, where adsorbate saturation is defined as 1 ML. While for Ir(110) regular and Ir(311) 1 geometrical ML (GML) is approximately 1 physical ML (PML), for Ir(210), there is a 2:1 ratio (geom/phys)[1], and

[1]With 2 geometrical ML on Ir(210), the resulting atom density of $1.2 \times 10^{15}\,\mathrm{atoms/cm^2}$ is around the experimental saturation coverage of $1 \times 10^{15}\,\mathrm{atoms/cm^2}$ [14], therefore 2 geometrical ML correspond to approximately 1 physical ML.

for Ir(110)-superstructure the conversion is approximately 8:1.
Figs. 7.2, 7.4–7.6 show probable (highly symmetric) binding sites, which were used as initial positions for the adsorbates, as well as the most stable adlayer configurations, for which the binding energies are summarized in Tab. 7.2. All oxygen binding energies reported here are with respect to half a gas-phase oxygen molecule (similar to Re case).

Surface	A [Å^2]	S	ϑ^{exp} [°]	$\vartheta^{\mathrm{geom}}$ [°]
Ir(210)	17.00	–	–	–
Ir(311)	12.61	0.70	18.7±0.7	19.29
Ir(110)	10.75	0.30	19.0±0.9	18.43
Ir(311)	12.61	0.47	18.7±0.7	19.29
Ir(110)-superstr.	82.24	0.53	7.0±1.0	7.13

Table 7.1: Surface area A per (1×1) unit cell (calculated), partial surface contributions (S) and tilt angles (ϑ) for two types of nanopyramids: those consisting of (311) and (110) faces and those consisting of (311) and (110)-superstructure faces. For the tilt angles, experimentally measured and geometrically derived (assuming bulk-truncated unrelaxed pyramids) values are given (taken from Ref. [65]).

7.2.1 O/Ir(210)

We began our studies with DFT calculations on the adsorption of atomic oxygen on planar Ir(210) with coverages of Θ=0.5, 1, and 2 GML.
At 0.5 GML we find that oxygen prefers binding at B-sites (see Fig. 7.2(1)), but slightly shifted towards the H-position. This allows each adatom to form covalent bonds to two top-layer Ir atoms and the nearby second-layer Ir atom, finally resulting in a three-fold binding. In this configuration the binding energy per oxygen atom is 2.11 eV. The next stable binding sites are the T-site (E_{bind}=1.78 eV) and C-site (E_{bind}=1.76 eV), which are considerably less stable than the B-site. Moreover, we find that oxygen is not stable at A-, D-, E-, and H-positions and during geometry optimization moves to nearby positions: A→T, D→B, E→C, and H→B. For those sites, the adsorbates were first fixed in the x- and y-directions, and after preoptimizing the geometry, all constraints were removed in the final optimization procedure.
At a coverage of 1 GML, oxygen binds most strongly on top (T-site) of each first-layer Ir atom (E_{bind}=1.78 eV) and at D-sites (E_{bind}=1.76 eV), which allows the adsorbate to coordinate to two Ir surface atoms. Only slightly lower binding energies were obtained for the C-site (E_{bind}=1.75 eV) and B-site (E_{bind}=1.74 eV). At the remaining positions (A, E, and H), oxygen is not stable and moves to

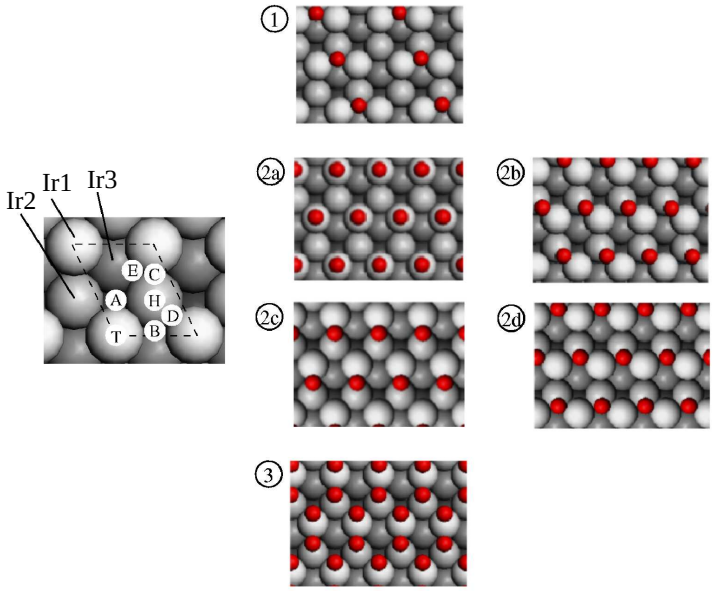

Figure 7.2: Top views of Ir(210) showing all binding sites at which O-adsorption has been studied (left), as well as the most stable structures for different coverages (right): (1) 0.5 GML, (2a–2d) 1 GML, (3) 2 GML.

nearby positions (A→T, E→C, and H→B). The similar binding energies for O on B-, D-, and T-sites result in a lower barrier for O-diffusion along the –T–D–B–D–T– direction. This unusual 1D oxygen diffusion may be the key to the experimentally observed higher reactivity of Ir(210) for CO oxidation compared to that of faceted Ir(210), where the onset CO_2 desorption temperature is much lower on planar than that on faceted Ir(210) [6].

When the coverage is increased to 2 GML, a variety of oxygen overlayers could form. Using the position labeling of Fig. 7.2, several possible combinations of distinguishable surface sites have been studied. Among these configurations occupying A and C (see Fig. 7.2(3)) leads to the highest binding energy (E_{bind}=1.01 eV). In this configuration, the adatoms form a hexagonal-like structure.

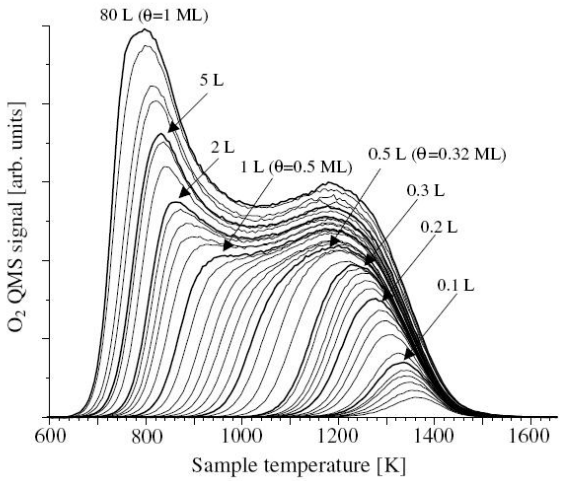

Figure 7.3: TPD spectra of O/Ir(210). Desorption has been performed at room temperature (taken from Ref. [14]).

Interestingly, the A-site was found to be unstable at lower coverages (0.5 and 1 GML). This might explain the presence of two peaks in the low coverage regime of the O_2 TPD spectra (see O_2 TPD spectra for oxygen coverages ≤ 0.5 PML of Fig. 7.3, which has been taken from Ref. [14]). There the peak temperatures are (roughly) 1200 K and 950 K for 0.5 PML of O. However, it should be noted that at higher oxygen coverages (> 0.5 PML) the low temperature peak shifts to a range between 780 and 900 K and therefore might be due to desorption from different faces of the faceted surface, since in this temperature range the surface already converts to the nanofaceted structure (due to higher oxygen coverage of > 0.5 PML).

structure	Coverage (GML)	binding site	E_{bind} (eV)
Ir(210)	0.50	B	2.11
(Fig.7.2(2a))	1.00	T	1.78
(Fig.7.2(2b))	1.00	D	1.76
(Fig.7.2(2c))	1.00	C	1.76
(Fig.7.2(2d))	1.00	B	1.74
	2.00	A/C	1.01
Ir(311) (Fig.7.4(1a))	0.50	A	2.16
(Fig.7.4(1b))	0.50	A	1.71
	1.00	A	1.72
Ir(110)	0.25	D	2.04
	0.50	D	2.09
	1.00	D	1.59
Ir(110)-superstructure	1.00	F	2.19
	2.00	F/D	2.11
	3.00	F/F/D	1.96
	4.00	F/F/E/E	1.31

Table 7.2: Binding energies (referenced to $\frac{1}{2}\,O_2$), and sites for oxygen on Ir(210), Ir(311), Ir(110), and Ir(110)-superstructure surfaces at different coverages. Only the most stable structure for each coverage is listed (see Figs. 7.2, 7.4, 7.5, and 7.6).

7.2.2 O/Ir(311)

On Ir(311) oxygen coverages of 0.5 GML, having (1×2) or (2×1) periodicity, as well as 1 GML with (1×1) periodicity have been studied.
At $\Theta = 0.5$ GML, oxygen prefers binding at the A-site (bridge-site) in a (1×2)-O

adlayer structure (see Fig. 7.4(1a)) for which we calculated a binding energy per oxygen atom of 2.16 eV. Induced by the presence of the strongly interacting adsorbates, there is a significant row-pairing of the topmost surface atoms, in which the Ir-atoms, which are not bound to the same adatom, reduce their interatomic distance by 0.12 Å. The next stable surface sites are the three-fold hollow F-site (E_{bind}=1.59 eV), where oxygen binds to two top-layer and one second-layer Ir atoms and the on-top T-site (E_{bind}=1.27 eV). In contrast, oxygen is not stable at B-, C-, D-, and H-sites and moves to the following nearby positions during geometry optimization: B→A, C→A, D→E, and H→F.
Besides the adlayer arrangements discussed above, a coverage of 0.5 GML can also be achieved in a (2×1)-O structure (Fig. 7.4(1b)). Although in this configuration the preferred binding sites are again A-sites, the adsorption energy of 1.71 eV is 0.45 eV lower than with a (1×2) periodicity. This behavior can be explained by the relatively strong O–O repulsion since along each second substrate row all adjacent A-sites are occupied. Therefore, the row-pairing effect that was observed in case of the (1×2)-O structure is absent now. Again, with the (2×1) periodicity, F- and N-sites are less favorable positions compared to A-sites by 0.39 and 0.42 eV, respectively, and adsorption at B-, C-, D-, or H-sites is not stable at all. Increasing the oxygen coverage to 1 GML, we still find the A-site to be most stable with a binding energy per adatom of 1.72 eV (see Fig. 7.4(2)), which is almost exactly the value obtained for 0.5 GML in a (2×1)-O structure. Therefore, we can conclude that even with 1 GML oxygen on the surface the O–O interaction is mainly due to adatoms being adsorbed on the same substrate row and that there is a negligible interaction between oxygen atoms of different rows.

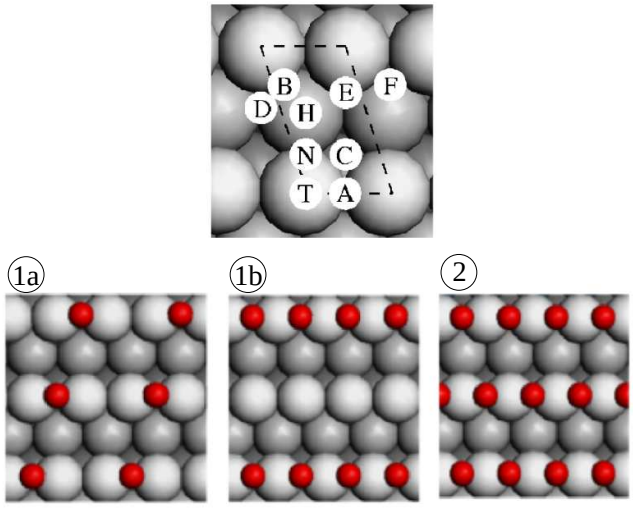

Figure 7.4: Top views of Ir(311) showing all binding sites at which O-adsorption has been studied (top), as well as the most stable structures for different coverages (bottom): (1a and 1b) 0.5 GML, (2) 1 GML.

7.2.3 O/Ir(110)

We have recently studied the structure and stability of Ir(110) surfaces in contact with an oxygen atmosphere by using density functional theory in combination with the *ab initio* atomistic thermodynamics approach [118]. Although in these calculations we found that for clean Ir(110) a (1×4) reconstruction is slightly more stable than the unreconstructed (1×1) surface, the latter becomes more stable as soon as oxygen adsorbs. Since in the present work the (110) faces are only relevant for the nanofacets that form due to oxygen adsorption, in the following, we will not consider the reconstructed Ir(110) surface.
Considering several ordered oxygen structures, we always find the bridge site (D-site) to be preferred (see Fig. 7.5). At 0.25 GML, only weak lateral adatom interactions can be expected. Therefore, the binding energy of 2.04 eV which we calculated for a $p(2\times2)$-O adlayer at the D-site should almost represent the zero-coverage limit. As a consequence of the strong interaction between oxygen and the surface, both Ir atoms to which the adatom binds are displaced by 0.07 Å away from the oxygen. This behavior (row-pairing), which we have already seen for Re surfaces and also Ir(311) surface, seems to be more general for the late 5*d*-elements. Significantly lower binding energies were obtained for C- ($E_{\text{bind}} = 1.24\,\text{eV}$), B- ($E_{\text{bind}} = 1.22\,\text{eV}$), and T-sites ($E_{\text{bind}} = 1.16\,\text{eV}$).

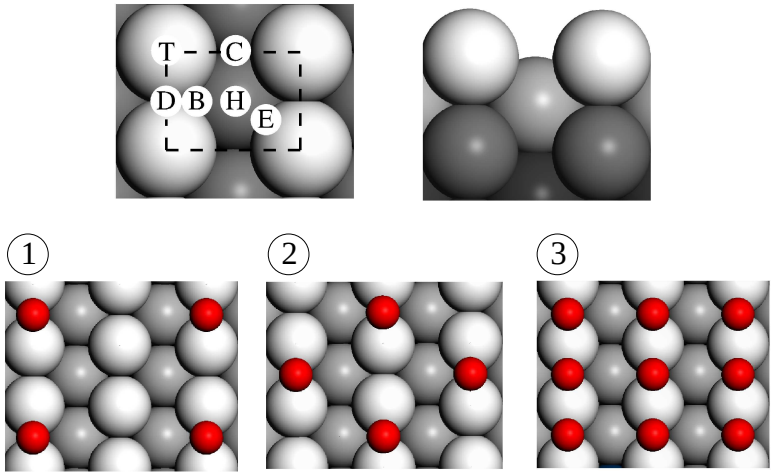

Figure 7.5: Top views of unreconstructed Ir(110) showing all binding sites at which O-adsorption has been studied (top), as well as the most stable structures for different coverages (bottom): (1) 0.25 GML, (2) 0.5 GML, (3) 1 GML.

At 0.5 GML, $c(2\times2)$- and $p(2\times1)$-O are both more stable than the $p(1\times2)$-O adlayer, with binding energies per oxygen of 2.09 and 2.04 eV, respectively (oxygen at D-sites). The geometry of the most stable configuration ($c(2\times2)$-O) shows good agreement with experimental measurements on the "oxidized" Ir(110) surface [119]. The expression "oxidized" is usually used since there is still an ongoing

debate whether oxygen is adsorbed on the surface or forms a surface oxide. For the Ir–O distance and the vertical separation of the topmost substrate layers, we calculate values of d(Ir–0)=1.97 Å and d_{12}=1.31 Å, which should be compared to the corresponding experimental distances of 1.93 ± 0.07 Å and 1.33 ± 0.07 Å. This agreement is rather interesting since the experimentally prepared $c(2\times2)$-O structure is usually thought of being adsorbed on an already formed surface oxide [119–123], while in our calculations we assume a pure Ir(110)-(1×1) surface. At a coverage of 1 GML, the D-site still remains energetically favored with binding energy of $E_{\text{bind}} = 1.59$ eV. Interestingly, the top site (T-site) becomes the second favorable adsorption site ($E_{\text{bind}} = 1.10$ eV). In addition, the calculated binding energy is significantly lower for 1 GML than for 0.25 and 0.5 GML by 0.45 and 0.50 eV, which is a direct consequence of a strong O–O repulsion.

7.2.4 O/Ir(110)-Superstructure

Experimentally, it was found that the (110)-faces of each nanopyramid consist of regular Ir(110)-(1×1) but also a more rough surface structure. On the basis of STM images and geometric considerations, Ermanoski *et al.* [65] proposed the latter one to be a stepped double-missing-row Ir(110)-superstructure as shown on the left side of Fig. 7.6.
To better understand the oxygen adsorption on this rather complex surface and to add this structure to the full surface phase diagram (see section 7.3), we performed DFT calculations on systems with up to four O atoms per unit cell, *i. e.*, $\Theta = 1, \ldots, 4$ GML.
Among the higher-symmetric surface sites indicated in the lower left model of Fig. 7.6, a single oxygen atom per unit cell prefers to occupy F-sites (E_{bind}=2.19 eV), which are bridge positions located directly below the last Ir-atom of each stepped row. Interestingly, binding on-top of the row at the B-site, which again allows for bridge-binding, results in an only slightly lower binding energy of 2.12 eV. Therefore, we can conclude that, on this stepped surface, oxygen is likely to be near the end of each row. However, there is a small barrier of ~ 0.2 eV to diffuse from B- to F-sites, which can be understood as a kind of Ehrlich–Schwöbel barrier. The next stable surface site is the D-site with a binding energy of 2.03 eV. Although this value is only 0.09 eV lower than the binding energy at the nearby B-site of the same row, diffusion of oxygen along the substrate-rows is hindered by a relatively high barrier of > 1 eV, thus again leading to a strong localization of adatoms around the row-ends.
As a consequence of the rather extended surface unit cell of this structure, even two oxygen atoms per unit cell give a relatively low adsorbate density. Therefore, both oxygen atoms behave as almost independent adsorbates, and while the first oxygen occupies a F-site, the D-site remains for the second oxygen (see Fig. 7.6(2)). The weak O–O interaction is also confirmed by the binding energy

per adsorbate of 2.11 eV, which is exactly the averaged value for binding a single oxygen per unit cell at F- and D-sites (see above). Only slightly weaker binding (E_{bind}=2.06 eV) is obtained with the more symmetric configuration of locating oxygen atoms at B- and D-sites.
Adding a third oxygen atom per unit cell does not change the binding site of the first two adsorbed atoms. Since most of the remaining vacant surface positions are lower-lying with respect to the surface-plane, which are rather unfavorable surface sites, the third atom binds at the second of both possible F-sites (see Fig. 7.6(3)). For this F/F/D configuration, we calculated a binding energy of 1.96 eV per oxygen. Compared to the previous systems with one or two oxygen atoms per unit cell, this value is reduced, showing an increasing O–O repulsion. Caused by this relatively strong O–O repulsion, an adlayer configuration in which the spacing between the oxygen atoms is smaller (adsorbates at F-, F-, and B-sites) leads to an 0.53 eV lower average binding energy.
Finally, with the knowledge obtained already, we studied two possible arrangements with four oxygen atoms per unit cell: (i) at F-, F-, E-, and E-sites and (ii) at E-, E-, C-, and C-sites. Since the O–O spacing in the first arrangement is at average larger than that of the second configuration, we find the first structure (see Fig. 7.6(4)) to be 0.76 eV more stable with an average binding energy of E_{bind}=1.31 eV.

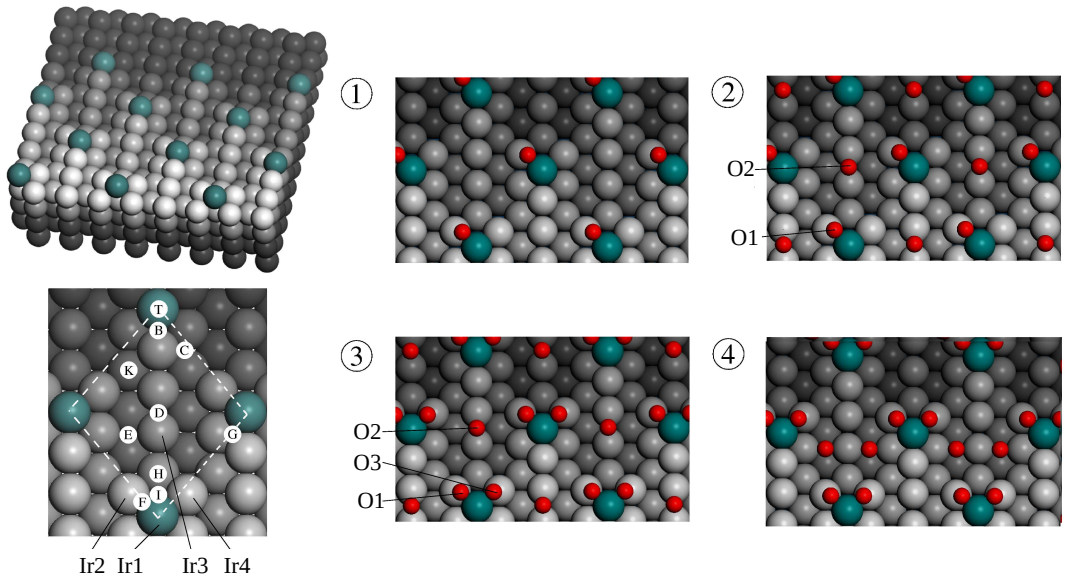

Figure 7.6: Top and perspective view of the "stepped double-missing-row" Ir(110)-superstructure, showing all binding sites at which O-adsorption has been considered (left), as well as the most stable structures for the different coverages (right): (1) 1 GML, (2) 2 GML, (3) 3 GML, (4) 4 GML.

7.3 Surface Phase Diagram of O/Ir(210)

The surface stabilities and oxygen binding energies for the different surfaces discussed in the previous sections and summarized in Tab. 7.2 [Ir(210), Ir(311)/Ir(31$\bar{1}$), Ir(110), and Ir(110)-superstructure] were used to generate a full phase diagram for surface faceting (see Fig. 7.7). There we distinguish between clean and oxygen-covered surfaces of:

- planar Ir(210);
- nanopyramids with (311), (31$\bar{1}$), and (110)-regular faces;
- nanopyramids with (311), (31$\bar{1}$), and (110)-superstructure faces.

The surface free energies γ for the faceted surfaces were calculated using the left side of eq. (2.64) with the parameters for the partial surface areas and facet tilt angles listed in Tab. 7.1. Each summand of this equation was evaluated by eq. (2.51) where the main temperature and pressure dependence is assumed to be dominated by the oxygen chemical potential (eq. (2.52)). In order to construct the phase diagram, the total surface free energy was plotted against the oxygen chemical potential referenced by $\Delta\mu_\mathrm{O} = \mu_\mathrm{O}^\mathrm{gas} - \frac{1}{2}E_{\mathrm{O}_2}^\mathrm{tot}$. The chemical potential was then converted to a temperature scale for $p_{\mathrm{O}_2} = 5 \times 10^{-11}$ atm, since most facet formation experiments have been conducted under this pressure. The remaining discussion is based on this condition.
Although experimentally the coexistence of (110)-regular and (110)-superstructure was observed on the largest nanopyramids, we only consider the extremes in which the entire (110)-faces of all pyramids are either (110)-regular or (110)-superstructure (see above).
Since our interest is in clean or oxygen-covered surface structures, we concentrate on the chemical potential range, where the IrO_2 bulk-oxide (rutile-type structure) is not stable. To evaluate this condition, we calculated the corresponding heat of formation. The obtained value of $\Delta\mu_\mathrm{O} = 0.93\,\mathrm{eV}$ per oxygen atom is lower than the experimental value of $\Delta H_\mathrm{f}^0 = 1.17\,\mathrm{eV/O}$ [124], which might be related to the known difficulties of density functional theory to accurately describe the O_2 molecule. Therefore, we shifted the $\Delta\mu_\mathrm{O}$-scale to match the experimental value. This procedure only causes a modified reference for the oxygen chemical potential, but does not change the conclusions, which are based on relative stabilities.
The surface phase diagram (Fig. 7.7) shows that for temperatures above 1130 K no oxygen is adsorbed on the surface (phase a), which nicely agrees with the experimental value of 1150 K [14]. Although we find the lowest surface free energy for a faceted surface in which the nanopyramids consist of (311), (31$\bar{1}$), and (110)-superstructure faces, the second type of nanofacets as well as planar

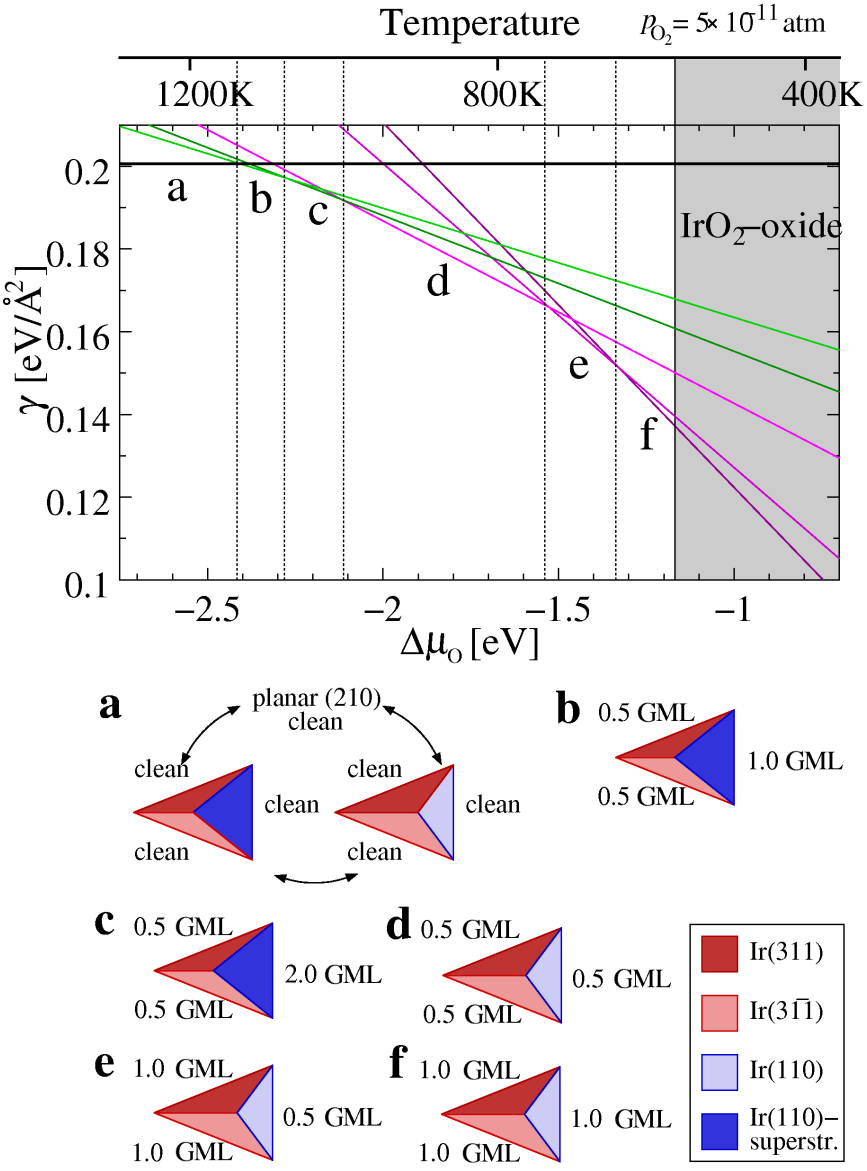

Figure 7.7: Surface phase diagram for the faceting of planar Ir(210), which shows the surface free energy γ as function of the oxygen chemical potential $\Delta\mu_O$. It combines clean and oxygen covered planar Ir(210) as well as two types of three-sided nanopyramids: (311)/(31$\bar{1}$)/(110)-regular (red lines) and (311)/(31$\bar{1}$)/(110)-superstructure (green lines). To avoid confusion only those phases (lines) are shown, which are most stable (lowest lying) in their particular oxygen chemical potential range (labeled as a–f). The models below the diagram sketch the surface structures and oxygen coverages of these phases. Finally, for $p_{O_2} = 5 \times 10^{-11}$ atm $\Delta\mu_O$ has been converted to a corresponding temperature scale given above the diagram.

Phase	Temp. range [K]	Theoretically predicted structure
a	$1130 < T$	coexistence of planar and faceted Ir(210)
b	$1070 < T < 1130$	nanofacets with 0.5 GML oxygen on (311) and (31$\bar{1}$), and 1.0 GML on (110)-superstructure
c	$1000 < T < 1070$	nanofacets with 0.5 GML oxygen on (311) and (31$\bar{1}$), and 2.0 GML on (110)-superstructure
d	$740 < T < 1000$	nanofacets with 0.5 GML oxygen on (311) and (31$\bar{1}$), and 0.5 GML on (110)-regular
e	$650 < T < 740$	nanofacets with 1.0 GML oxygen on (311) and (31$\bar{1}$), and 0.5 GML on (110)-regular
f	$575 < T < 650$	nanofacets with 1.0 GML oxygen on (311) and (31$\bar{1}$), and 1.0 GML on (110)-regular

Table 7.3: Temperature ranges, structures, and oxygen coverages of the different surface phases shown in the phase diagram Fig. 7.7. Note: For all surfaces 1 GML refers to 1 adatom per unit cell, whose sizes are given in Tab. 7.1.

nonfaceted Ir(210) are only 3–4 meV/Å^2 less stable. Since this energy difference is certainly within the accuracy of the calculations, from the surface free energies alone, no clear statement on the morphology of the clean surface is possible, that is why, in Fig. 7.7, phase a has been assumed to show coexistence between clean planar and clean faceted Ir(210). However, so far we have neglected energy contributions from step-edges and kinks, which usually reduce the stability. Since these contributions, which will be in the same energy range, are only relevant for the faceted surfaces, we would predict the most stable clean surface to be planar Ir(210). This is also in agreement with experiment observations, finding clean planar Ir(210) at these high temperatures.
Below 1130 K, adsorption of oxygen takes place, causing the formation or stabilization of the nanofaceted surface. While facets formed at higher temperatures consist of (311), (31$\bar{1}$) and (110)-superstructure faces (Fig. 7.7: phases b and c), at lower temperatures facets with (311), (31$\bar{1}$) and (110)-regular faces are stable (phases d–f). Formation at even lower temperatures leads to an increasing oxygen coverage on the different facet faces, but does not modify the structure. Finally, the IrO_2 bulk-oxide appears as stable phase for temperatures lower than 575 K [124]. Overall, we find the surface phases summarized in Tab. 7.3.
While we expect clean planar Ir(210) to be the stable phase at high temperatures, oxygen-covered planar Ir(210) might only be stable at temperatures below 1050 K and low adsorbate coverages. However, facets immediately become stabilized if there is enough oxygen on the surface to generate phase b or c of the phase diagram (Fig. 7.7), which means 0.5 GML on both {311} faces and 1.0–2.0 GML on the Ir(110)-superstructure phase. Assuming that during

facet formation no oxygen desorbs from the surface, this would convert to $\sim 0.9\,\mathrm{GML}$ (0.45 physical ML (PML)) on the planar Ir(210) substrate, which nicely agrees with the critical coverage for faceting of $\geq 0.5\,\mathrm{PML}$ observed experimentally [14, 22]. Moreover, the presence of the (110)-superstructure face at temperatures of $1130\,\mathrm{K} > T > 1000\,\mathrm{K}$ is rather remarkable. On a planar Ir(110) surface, this superstructure is always less favorable than regular (110), but this is different for the faceted Ir(210) surface. There, the superstructure forms on the (110)-side of the nanopyramids at higher temperatures, which is a consequence of the non-linear dependency of the surface free energy on the tilt angle (see prefactors on the left side of eq. (2.64)) and the fact that the (110)-faces of the nanopyramids are already tilted with respect to the (210)-substrate. Again, this behavior is observed experimentally [65].

In order to evaluate the influences coming from choosing the PBE exchange-correlation functional, we additionally calculated the most relevant surface structures with the LDA functional and generated the equivalent surface phase diagram. Comparison shows that with the LDA functional all phase transitions are shifted toward higher temperatures, without causing any changes in the ordering of the stable phases. Furthermore, the stability ranges, respectively, chemical potential ranges, of the different phases are almost the same with both xc-functionals. Therefore, the conclusions drawn above are qualitatively independent of the xc-functional.

In summary, we studied the surface stability of clean and oxygen-covered surfaces of Ir(210), (311), (110), and (110) superstructure, which are involved in the formation of nanopyramidal facets on Ir(210). The corresponding surface phase diagram shows that for an oxygen partial pressure of 5×10^{-11} atm and temperatures lower than 1130 K, oxygen adsorbs on the surface, leading to the formation of the experimentally observed three-sided facets. While at higher temperatures these facets consist of (311), $(31\bar{1})$, and (110) superstructure faces, at lower temperatures, the (110) face is found to be unreconstructed, leading to $(311)/(31\bar{1})/(110)$ regular facets. Finally, lowering the temperature only leads to an increasing oxygen coverage at the different facet faces.

Chapter 8

Conclusions and Outlook

Controlling a desired nanometer-scale morphology of surfaces is an important concept in surface science. Studies of adsorbate-induced faceting can provide a step in this direction. Furthermore, faceted metal surfaces are interesting model systems for studying structural sensitivity and size effects in catalytic reactions. Experimental studies showed that planar metal surfaces that are rough on the atomic scale, such as hcp Re(11$\bar{2}$1) and fcc Ir(210), become faceted when covered by certain strongly-interacting gases and annealed at elevated temperatures. This work aims to understand the adsorbate-induced faceting of these surfaces on the basis of microscopic information. In the present work density functional theory (DFT) calculations in conjunction with thermodynamic considerations were performed to obtain an atomistic understanding of facet formation. By performing an extended number of calculations we have determined structures and energetics of all clean and adsorbate-covered surfaces involved in the faceting of Re(11$\bar{2}$1) and Ir(210). In addition, for those surfaces, that showed indications for reconstructions, we also investigated the possibility to induce or remove these reconstructions by adsorptions. Using the obtained energies for the different surfaces together with the *ab initio* atomistic thermodynamics approach, we investigated the stabilities both of the planar substrates as well as the facets in the presence of either surrounding O_2 or N_2 gas.

Our calculations confirm the recent STM measurements that, depending on the nature of the adsorbate, showed distinct facets when the Re(11$\bar{2}$1) substrate is annealed to elevated temperatures. Experimentally, four-sided pyramids are formed in the case of oxygen adsorption while two-sided ridges appear after nitrogen adsorption. For the clean surfaces, our results reveal a higher stability of planar Re(11$\bar{2}$1) compared to both types of facets. This preference is in line with experimental observations and comes from the fact that anisotropy in surface free energy is not high enough.

According to the theoretical phase diagrams, in case of oxygen one can tune between the planar substrate, two-sided ridges, or even four-sided nano-pyramids by

setting the temperature and pressure conditions accordingly. The experimentally observed four-sided nano-pyramids are more favorable than the other two possibilities at 900 K at the experimentally used oxygen partial pressure of 5×10^{-10} atm and are possibly stabilized due to kinetic limitations in the formation of ReO_2 bulk-oxide. In contact with a nitrogen atmosphere, under the experimentally used temperature and pressure conditions ($T \geq 900$ K and $p_{O_2} = 5 \times 10^{-10}$ atm) two-sided ridges are significantly more stable than the planar surface and four-sided pyramids, which was the facet structure observed after oxygen adsorption. These conclusions are in good agreement with the experimental results.

Furthermore, facet formation on Ir(210) induced by oxygen adsorption was studied. Under experimental temperature and pressure conditions ($T \geq 600$ K and $p_{O_2} = 5 \times 10^{-11}$ atm) oxygen adsorption on the Ir(210) surface leads to the formation of the experimentally observed three-sided facets. In a narrow temperature range, a type of Ir(110) reconstruction is stabilized on one of the faces of the nanopyramids. Interestingly, this structure is not favorable on a regular (110) surface and is stable only on the facets.

In this thesis, by a very close collaboration with experimentalists, deeper insights into surface faceting were obtained. The surface phase diagrams generated on the basis of DFT calculations confirmed that the presence of adsorbates enhances the anisotropy in surface free energy for the different orientations, which finally causes the faceted surfaces to become thermodynamically favorable. We could also show that by choosing an appropriate adsorbate and environmental temperature and pressure conditions, the surface morphology could be tailored on the nanometer-scale. Our calculations not only reproduce the experimentally observed surface faceting, but also provide quantitative information and physical insights into the morphological changes of the facets with adsorbate, adsorbate coverage and annealing temperature.

This study has important implications for transition metal-based catalysts that work under oxygen- or nitrogen-rich environments since the performance of the catalysts is usually affected by their structures. Besides the catalytic properties such nanostructured surfaces might provide a basis for bridging the gap between nanoparticles and single crystal surfaces.

We believe that this work might stimulate further experimental work using these surfaces as model systems for catalytic studies or as templates for growing nanostructures. It is also desirable to extend this research to other transition metal surfaces, which have applications in magnetic storage devices or sensors.

Appendix A

Convergence Tests

To determine the numerical uncertainties, we carefully checked the convergence of the energetics of the bulk crystals and surfaces with respect to the energy cutoff and **k**-point mesh. Additionally, similar tests were carried out to find the minimal set for the supercell parameters (the number of layers and vacuum size) required for an appropriate modeling of surface properties. This allowed us to reduce the computational effort while understanding the accuracy.

A.1 Bulk Re

The calculated physical properties of bulk materials can be strongly influenced by choosing different number of **k**-points and energy cutoffs. To find reasonable parameters for Re bulk calculations, we obtained the cohesive energies for:

- a variety of energy cutoff values with a fixed number of **k**-points of 160, corresponding to a 8×8×5 MP **k**-point mesh;
- different number of **k**-points ($N_\mathrm{x} \times N_\mathrm{y} \times N_\mathrm{z}$ Monkhorst-Pack (MP) **k**-point meshes) for a fixed energy cutoff of 300 eV.

These calculations were performed with bulk unit cells with the following lattice constants: $a = b = 2.76$ Å and $c = 4.47$ Å . The single Re atom, which is required for evaluating the cohesive energy, was modeled with a non-symmetric 16 Å×17 Å×20 Å supercell. Besides PBE, the same procedure was repeated for the LDA exchange–correlation functional. The results are illustrated in Fig. A.1. It can be seen that for both PBE and LDA the cohesive energy is converged within 10 meV/atom with an energy cutoff of E_cutoff=380 eV and 160 **k**-points in the BZ, corresponding to a $8 \times 8 \times 5$ Monkhorst-Pack grid.

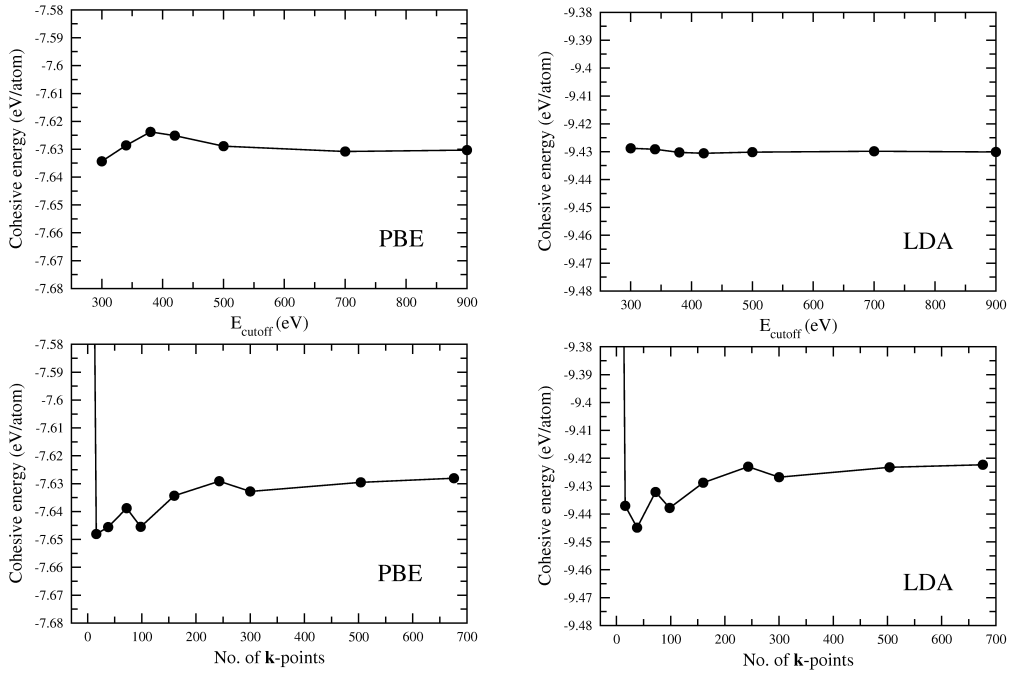

Figure A.1: Cohesive energy of Re as a function of energy cutoff (above) and number of **k**-points (below) for the PBE and LDA functional.

A.2 Bulk ReO_2

Similar to rhenium bulk, for ReO_2 bulk-oxide we checked convergence of the heat of formation with respect to the energy cutoffs and number of **k**-points. Heats of formation were obtained for:

- a variety of energy cutoffs for a fixed number of **k**-points of 50, corresponding to a 5×4×5 MP **k**-point mesh;
- different number of **k**-points for a plane wave cutoff of 380 eV.

These calculations were performed using lattice constants of a=4.8094 Å, b=5.6433 Å, and c=4.6007 Å for ReO_2 and a=2.78 Å and c= 4.48 Å for Re. The results are presented in Fig. A.2. It is found that the heat of formation is converged within 40 meV (in both PBE and LDA) with an energy cutoff of E_{cutoff}=380 eV and 50 **k**-points in the BZ, corresponding to Monkhorst-Pack grid of $5 \times 4 \times 5$.

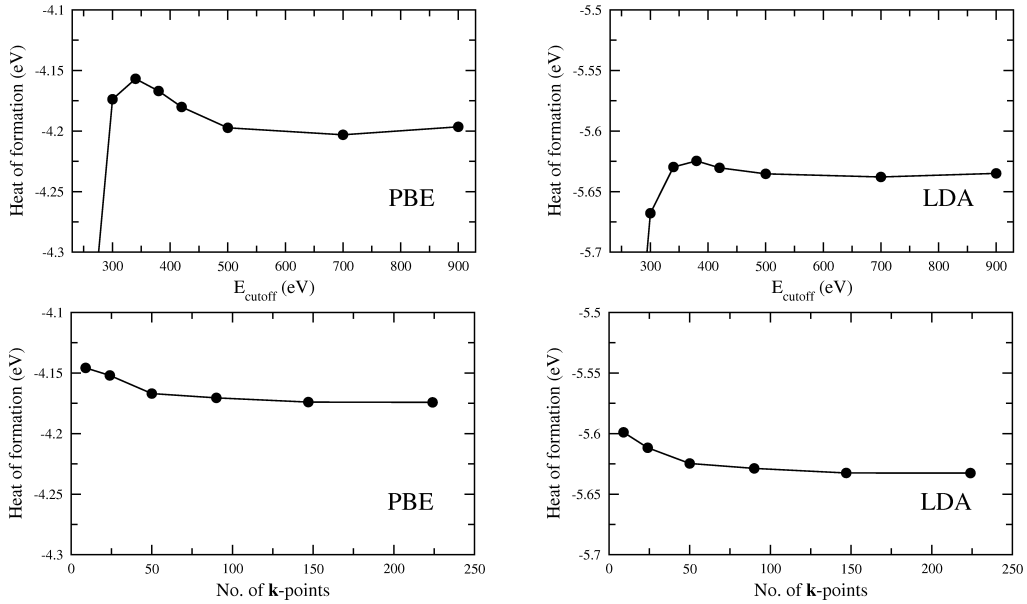

Figure A.2: Heat of formation of ReO_2 as a function of energy cutoff (above) and number of **k**-points (below) for the PBE and LDA functional.

A.3 Molecular Properties

To generate the (p, T)-phase diagrams for O and N/Re$(11\bar{2}1)$ we needed to evaluate the energetics of the isolated oxygen and nitrogen molecules. The molecules (O_2 and N_2) and the corresponding atoms were modeled using fully non-symmetric 16 Å×17 Å×20 Å supercells and considering one **k**-point for sampling of the Brillouin zone. For both atoms and molecules we performed spin-polarized calculations. It should be noted that quantities of interest such as equilibrium bond length, binding energy, and vibrational frequency of the molecules are strongly influenced by the energy cutoff. For each molecule we determined these quantities for several E_{cutoff} by applying a polynomial fit to the obtained total energies versus bond length curves. The results are discussed in the following sections.

A.3.1 Oxygen

Fig. A.3 shows the convergence of binding energy, bond length, and vibrational frequency of O_2 with respect to the energy cutoff for the PBE and LDA functional. It can be seen that these quantities are well converged with an energy cutoff of 380 eV. The calculated physical properties at the optimum energy cutoff are given in Tab. A.1. The binding energy of O_2 ($E^{\text{b}}_{O_2}$) obtained with both functionals using ultrasoft pseudopotential (USPP) are larger than the experimental value, which is in line with other DFT-GGA and LDA results. The reason for this error in

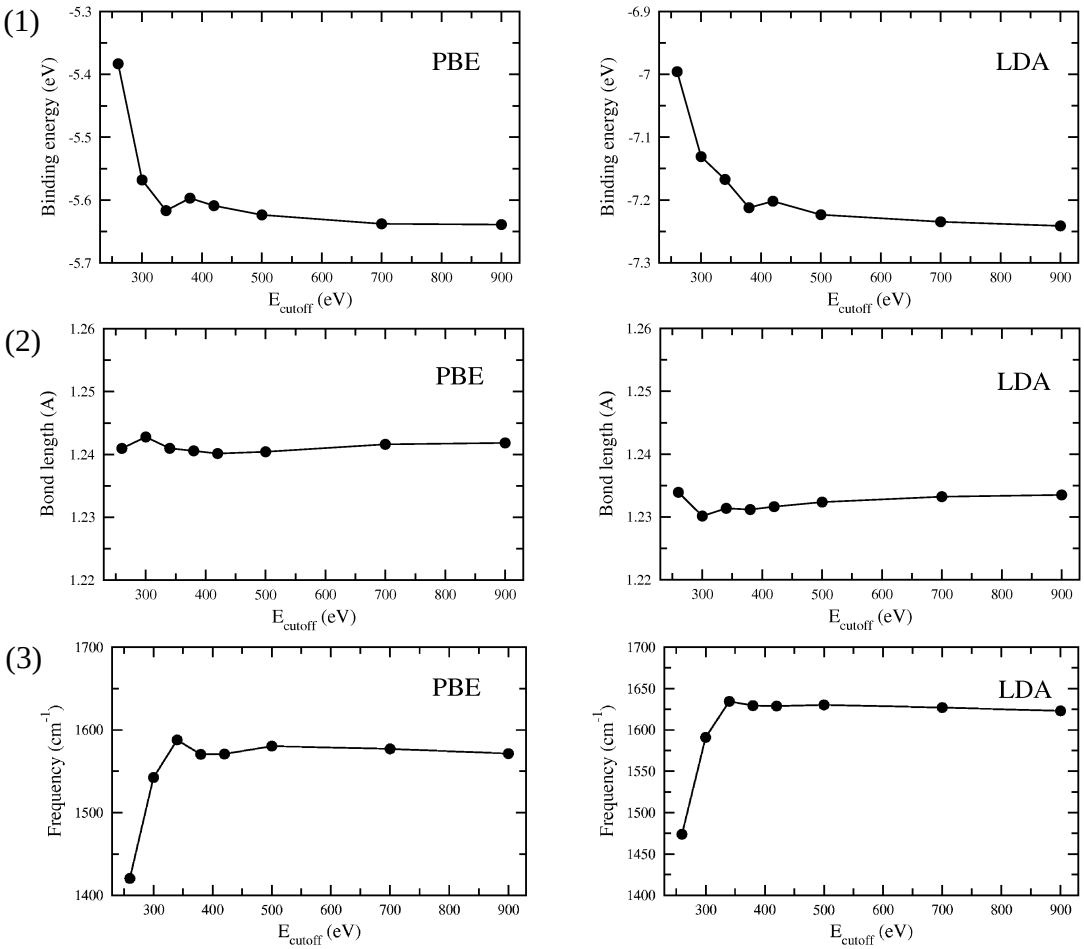

Figure A.3: (1) Binding energy, (2) bond length, and (3) frequency of O_2 molecule as a function of energy cutoff for the PBE and LDA functional.

Method	$E^{\mathrm{b}}_{\mathrm{O}_2}$ (eV)	$d_{\mathrm{O-O}}$ (Å)	ω (cm^{-1})
USPP-PBE	5.60	1.24	1570
USPP-LDA	7.21	1.23	1629
AE-PBE [125]	6.20	1.22	1527 [126]
AE-LDA [125]	7.56	1.21	1592 [126]
Expt. [127]	5.17	1.21	1580 [128]

Table A.1: The binding energy ($E^{\mathrm{b}}_{\mathrm{O}_2}$), bond length ($d_{\mathrm{O-O}}$), and frequency ($\omega$) for the O_2 molecule calculated using the PBE and LDA functional. The all-electron results and experimentally measured values are included for comparison.

the binding energy of O_2 calculated by using DFT is that the exchange energy is not very well approximated by LDA and GGAs in this system [129]. Fortunately, quantities like O adsorption energy on a surface or surface free energy of O-covered systems are obtained by differences in DFT energies and a significant error cancellation is usually achieved in these kind of calculations.
Furthermore, other quantities (d_{O-O} and ω) calculated by USPP are in good agreement with both all electron (AE)[1] and experimental results.

A.3.2 Nitrogen

Fig. A.4 shows the convergence of binding energy, bond length, and vibrational frequency of N_2 with respect to the energy cutoff for PBE and LDA. We see that the energy cutoff of 380 eV yields converged results for these quantities. The

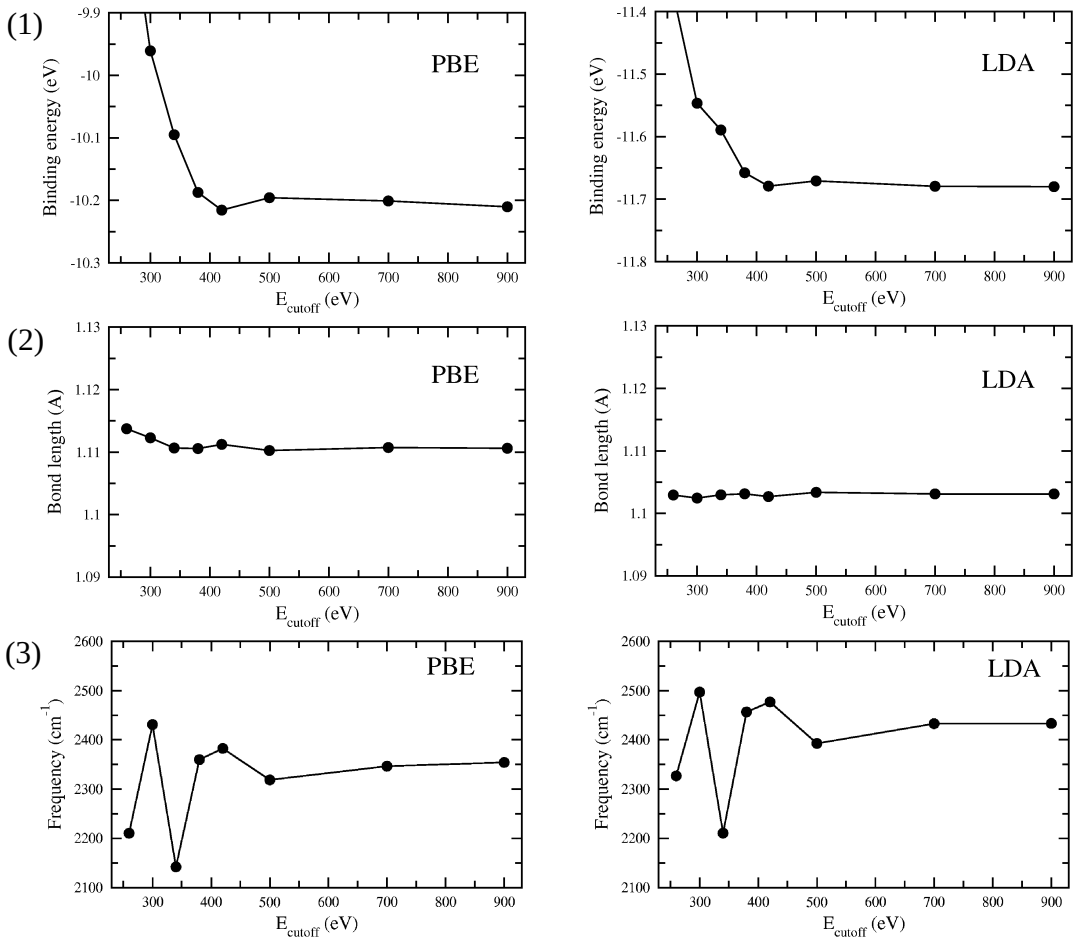

Figure A.4: (1) Binding energy, (2) bond length, and (3) frequency of N_2 molecule as a function of energy cutoff for the PBE and LDA functional.

[1] All electron calculations were performed by using the WIEN2K code [78].

calculated physical properties at this energy cutoff are given in Tab. A.2. Our results for USPP-PBE agree well with those calculated via AE-PBE approach and measured experimentally. As expected, the USPP-LDA overestimates the binding energy of N_2 compared to experimental value, but gives very similar result to the AE-LDA.

Method	$E^{b}_{N_2}$ (eV)	d_{N-N} (Å)	ω (cm^{-1})
USPP-PBE	10.19	1.11	2360
USPP-LDA	11.66	1.10	2457
AE-PBE [130]	10.38	1.11	2349.6
AE-LDA [131]	11.587	1.099	2384
Expt. [132]	9.9	1.10	2360

Table A.2: The binding energy ($E^{b}_{N_2}$), bond length (d_{N-N}), and frequency (ω) for the N_2 molecule calculated using the PBE and LDA functional. The all-electron results and experimentally measured values are included for comparison.

A.4 Re Surfaces

As we mentioned in Chapter 6, the surface free energy (γ) is calculated to compare the stability of different Re surfaces. This quantity can change strongly with the plane wave cutoff, number of **k**-points, layer thickness, and vacuum thickness. To find the optimum values for these parameters we checked the convergence of γ for all Re surfaces involved in the faceting of Re(11$\bar{2}$1). The convergence of each parameter was tested independently. All test calculations presented below were performed only by using the PBE functional since similar convergence behaviors are expected for LDA (see previous sections).
Although we have found that using the energy cutoff of 380 eV yields to reasonably accurate results for Re, ReO_2, O_2, and N_2 systems, it is noteworthy to check this result for the surfaces. For each surface orientation the surface free energies were calculated considering the same surface geometry (without relaxation) assuming a variety of different energy cutoffs. For nitrogen-adsorbed Re surfaces we only focused on N/Re(10$\bar{1}$0). In this case we expect similar results as for the oxygen-covered surfaces, since we found that the physical quantities of Re bulk as well as O_2 and N_2 molecules are converged with the same energy cutoff. The surface free energy versus energy cutoff for O/Re(11$\bar{2}$1), O/Re(10$\bar{1}$0), O/Re(10$\bar{1}$1), and O/Re(13$\bar{4}$2) is shown in Fig. A.5 and for N/Re(10$\bar{1}$0) is presented in Fig. A.6. As we expected, the energy cutoff of 380 eV is sufficient to yield converged results for all systems. At this cutoff, γ is converged up to 2 meV/Å^2.

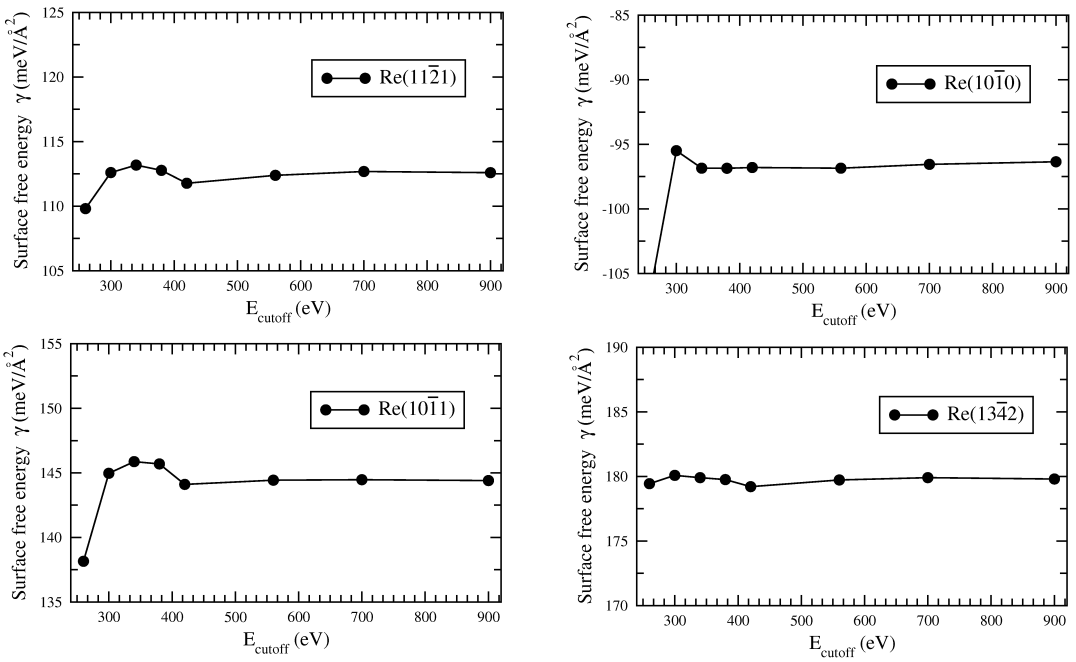

Figure A.5: The surface free energy γ as a function of energy cutoff for the oxygen-covered Re surfaces.

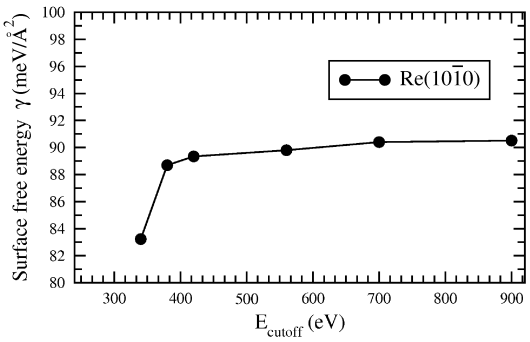

Figure A.6: The surface free energy γ as a function of energy cutoff for the N/Re(10$\bar{1}$0) surface.

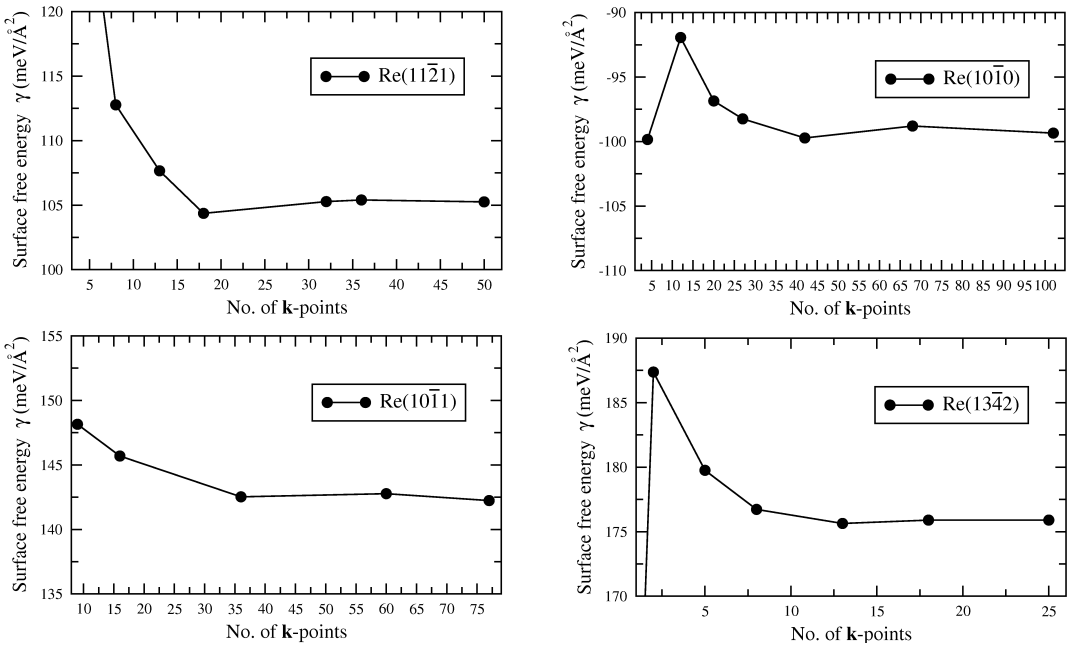

Figure A.7: The surface free energy γ as a function of total number of **k**-points for the oxygen-covered Re surfaces.

To test the number of **k**-points we used the optimum value of E_{cutoff}=380 eV. We find from Fig. A.7 that with a total number of **k**-points of 8, 20, 16, and 5, corresponding to 4×4, 5×8, 4×8, and 3×3 Monkhorst–Pack **k**-point meshes, the γ is converged up to $\sim$ 7, 3, 3, and 4 meV/Å^2 compared to the best obtained values for Re(11$\bar{2}$1), (10$\bar{1}$0), (10$\bar{1}$1), and (13$\bar{4}$2) surfaces, respectively. Similar convergence behavior is observed for these surface orientations. Therefore, we expect that uncertainties arising from the **k**-point sampling should be insignificant when comparing the stability of (10$\bar{1}$0), (10$\bar{1}$1), and (13$\bar{4}$2) surfaces with each other (due to error cancellation). A larger inaccuracy of $\sim$ 4 meV/Å^2 is estimated when comparing the stability of (11$\bar{2}$1) with the mentioned orientations.
Concerning the number of Re layers in the slab, we performed the convergence tests for each orientation using the optimum energy cutoff and number of **k**-points as found above. Fig. A.8 presents γ corresponding to the fully relaxed oxygen-covered surfaces as a function of slab thickness. It turned out that slabs with 19, 11, 14, and 30 Re-layers for Re(11$\bar{2}$1), (10$\bar{1}$0), (10$\bar{1}$1), and (13$\bar{4}$2) give satisfactory results, showing convergence up to 2 meV/Å^2.
In this work, for all Re surfaces, the vacuum size was always chosen $\geq$ 13 Å. In order to investigate how our results change when using supercells with a larger vacuum thickness, we also tested a vacuum of 20 Å. Changes in the surface free energies were determined to be smaller than 0.5 meV/Å^2 for any of the studied orientations. Therefore, the vacuum size of 13 Å was found to be sufficiently

large enough to separate periodically repeated slabs.

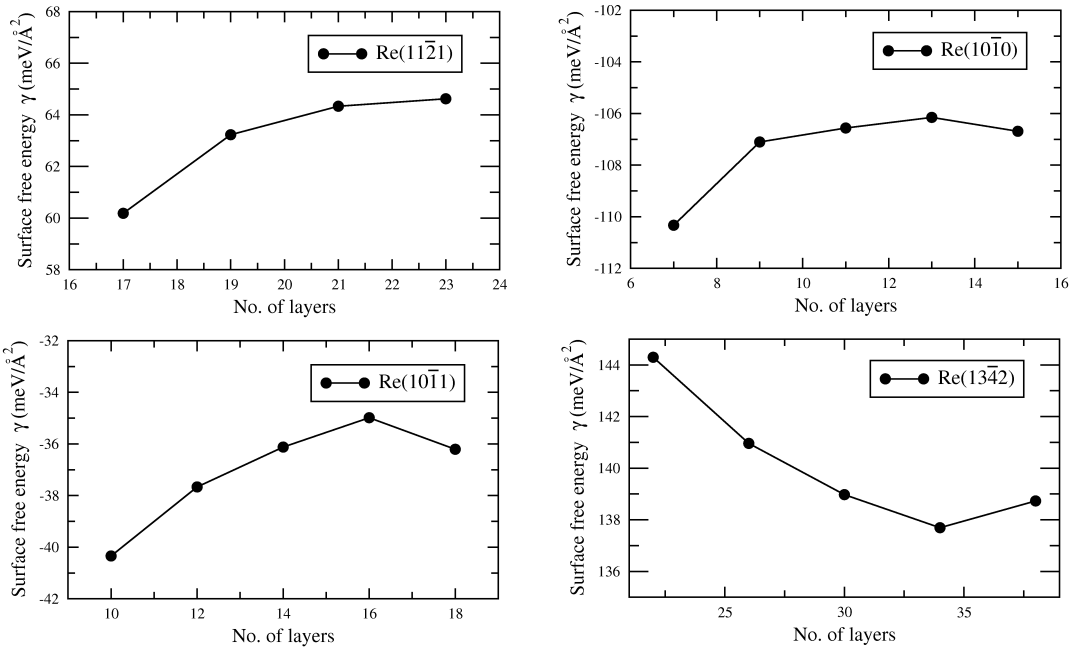

Figure A.8: The surface free energy γ as a function of the number of layers for the oxygen-covered Re surfaces.

Appendix B

Binding Energies of O and N on Re Surfaces

B.1 Re(11$\bar{2}$1)

	oxygen adsorbate		nitrogen adsorbate	
	(1×2)-O	(2×1)-O	(1×2)-N	(2×1)-N
binding site	E_{bind} (eV)	E_{bind} (eV)	E_{bind} (eV)	E_{bind} (eV)
H1	3.61	–	1.56	1.35
H4	3.66	3.78	1.68	1.83
B1	3.70	3.71	1.19	–
B3	2.58	–	1.22	1.38
B5	3.82	3.81	1.27	1.27
T1	3.44	–	0.04	–
H2	unstable	–	1.00	–
H3	unstable	–	0.80	–
T2	unstable	–	–0.10	–
B2	unstable	–	unstable	–
B4	unstable	–	unstable	–
T3	unstable	–	unstable	–
T4	unstable	–	unstable	–

Table B.1: Binding energies (referenced to $^1/_2\,O_2$ or $^1/_2\,N_2$) for the adsorption of oxygen or nitrogen to different sites (as labeled in Fig. 5.1) on the Re(11$\bar{2}$1) surface at 0.5 GML with (1×2) or (2×1) periodicity.

	oxygen adsorbate	nitrogen adsorbate
binding site	E_{bind} (eV)	E_{bind} (eV)
H1	3.55	1.39
H4	3.65	1.66
B1	3.72	1.14
B3	2.81	1.35
B5	3.85	1.27
T1	3.34	0.02
H2	unstable	0.87
H3	unstable	0.75
B2	unstable	unstable
B4	unstable	unstable
T2	unstable	unstable
T3	unstable	unstable
T4	unstable	unstable

Table B.2: Binding energies (referenced to $^1/_2\,O_2$ or $^1/_2\,N_2$) for the adsorption of oxygen or nitrogen to different sites (as labeled in Fig. 5.1) on the Re(11$\bar{2}$1) surface at 1 GML.

	oxygen adsorbate	nitrogen adsorbate
binding site	E_{bind} (eV)	E_{bind} (eV)
B5/H3	3.26	0.97
B5/H1	3.35	0.96
B5/B3	3.06	1.01
T1/B3	3.09	0.86
H1/H3	3.00	0.54
H1/H2	2.79	0.74
B1/B3	2.99	1.00
H4/H2	2.89	0.83
H4/H1	3.28	1.21
H4/B3	unstable	1.06
B1/H2	unstable	1.10
H4/B1	3.48	unstable
H1/B3	unstable	unstable

Table B.3: Binding energies (referenced to $^1/_2\,O_2$ and $^1/_2\,N_2$) for a variety of oxygen or nitrogen configurations on the Re(11$\bar{2}$1) surface at 2 GML. The binding sites are as labeled in Fig. 5.1.

	oxygen adsorbate	nitrogen adsorbate
binding site	E_{bind} (eV)	E_{bind} (eV)
B5/H3/B3	2.98	0.39
B5/H3/H1	2.97	0.73
H4/B1/H2	2.95	0.73
H4/H1/T4	2.81	0.81
H4/T1/B3	2.87	unstable
B5/H3/B4	2.77	unstable
B5/H1/B2	unstable	unstable
H4/B1/B3	unstable	unstable
H4/H1/H2	unstable	unstable

Table B.4: Binding energies (referenced to $^1/_2\,O_2$ and $^1/_2\,N_2$) for a variety of oxygen or nitrogen configurations on the Re(11$\bar{2}$1) surface at 3 GML. The binding sites are as labeled in Fig. 5.1.

B.2 Re(10$\bar{1}$0)

B.2.1 Unreconstructed Re(10$\bar{1}$0)-(1×1)

	oxygen adsorbate		nitrogen adsorbate	
	(1×2)-O	(2×1)-O	(1×2)-N	(2×1)-N
binding site	E_{bind} (eV)	E_{bind} (eV)	E_{bind} (eV)	E_{bind} (eV)
H1	3.71	3.61	1.67	1.33
H2	2.53	–	0.67	–
B1	3.55	3.05	1.14	0.52
B2	2.29	–	0.59	–
T1	3.29	–	0.09	–
T2	1.42	–	-1.31	–
B3	unstable	–	unstable	–

Table B.5: Binding energies (referenced to $^1/_2\,O_2$ or $^1/_2\,N_2$) for the adsorption of oxygen or nitrogen to different sites (as labeled in Fig. 5.7) on the Re(10$\bar{1}$0)-(1×1) surface at 0.5 GML with (1×2) or (2×1) periodicity.

	oxygen adsorbate	nitrogen adsorbate
binding site	E_{bind} (eV)	E_{bind} (eV)
H1	3.60	1.27
H2	2.82	0.36
B1	3.09	0.49
B2	2.45	0.2
T1	2.65	–0.51
T2	1.48	–1.33
B3	unstable	unstable

Table B.6: Binding energies (referenced to $^1/_2\,O_2$ or $^1/_2\,N_2$) for the adsorption of oxygen or nitrogen to different sites (as labeled in Fig. 5.7) on the Re(10$\bar{1}$0)-(1×1) surface at 1 GML.

	oxygen adsorbate	nitrogen adsorbate
binding site	E_{bind} (eV)	E_{bind} (eV)
B1/T2	1.74	–0.91
B1/B2	2.39	–0.03
H1/H2	2.76	0.09
T1/B2	1.99	–0.39
T1/T2	1.61	–1.06
H1/H1	2.69	0.23

Table B.7: Binding energies (referenced to $^1/_2\,O_2$ or $^1/_2\,N_2$) for a variety of oxygen or nitrogen configurations on the Re(10$\bar{1}$0)-(1×1) surface at 2 GML. The binding sites are as labeled in Fig. 5.7.

B.2.2 Reconstructed Re(10$\bar{1}$0)-(1×2)

coverage (GML)	binding site	E_{bind} (eV)
0.5	H1	3.89
1.0	H1/H1′	3.58
1.5	H1/B2/H1′	3.26
	H2/T3/H2′	3.22
	H1/H3/H1′	3.25
	H1/T3/H1′	unstable
2.0	H1/H3/B2′/H2′	2.90
	H1/H3/H3′/H1′	2.98
	B1/H2/B2/H2′	2.97
	B1/H2/T3/H2′	unstable

Table B.8: Binding energies (referenced to $^1/_2\,O_2$) for a variety of oxygen configurations on the Re(10$\bar{1}$0)-(1×2) surface at different coverages. The binding sites are as labeled in Fig. 5.10(a).

B.2.3 Reconstructed Re(10$\bar{1}$0)-(1×3)

coverage (GML)	binding site	E_{bind} (eV)
0.33	H1	3.81
	H2	3.27
	H3	3.07
	H5	2.87
	B2	3.13
	B3	2.74
	T1	2.65
	T2	2.60
	H4	unstable
	B1	unstable
	T3	unstable
0.66	H1/H1′	3.78
	H1/H4	3.71
1.00	H1/H1′/H4	3.50
	H2/H2′/H4	3.26
	H1/T3/H4	3.47
1.33	H2/H2′/H4/H4′	3.23
	H2/T3/H2′/H4	3.20
	H1/T3/H1′/H4	3.30
	H1/H3/H1′/H4	3.26
	H1/H3′/H1′/H4	3.29
	H1/B3/H1′/H4	unstable
1.66	H1/T3/H1′/H4/H4′	3.16
	H1/T3/H1′/H4/H5′	3.11
	H1/H3/H1′/H4/H4′	3.12
	H2/T3/H2′/H4/H4′	3.21
	H2/T3/H2′/H4/H5′	3.18
	H2/B3/H2/H4/H4′	3.14
	B1/H2/T3/H2/H5	3.18
	H2/T3/H2′/H4/H4′	3.21
	H2/T3/H2′/H4/H4′	3.21
	H2/H3/H2/H4/H4′	unstable
2.00	H1/H3/H3′/H1′/H4/H4′	2.90
	H1/H3/T3/H2′/H4/H4′	2.86
	H1/H3/T3/H1′/H4/H4′	2.81
	H1/H3/H3′/H1′/H4/H4′	2.90
	H4′/H2/T3/H2′/B1′/H5	2.99
	H1/H3/T3/H1′/H4/H4′	unstable
	H2/H3/H3′/H2′/H4/H4′	unstable

Table B.9: Binding energies (referenced to $^1/_2\,O_2$) for a variety of oxygen configurations on the Re(10$\bar{1}$0)-(1×3) single MR surface at different coverages. The binding sites are as labeled in Fig. 5.10(a).

coverage (GML)	binding site	E_{bind} (eV)
0.33	H1	3.84
	H2	3.31
	H3	3.12
	H4	2.72
	B1	3.01
	B2	3.30
	B3	3.47
	B5	2.63
	T1	2.70
	T2	2.71
	T4	2.71
	B4	unstable
	T3	unstable
0.66	H1/B2′	3.54
	H1/B3	3.67
	H1/H1′	3.55
1,00	H1/B3/H1′	3.53
	H2/B3/H2′	3.40
1.33	H1/B2/B2′/H1′	3.09
	H1/H3/H3′/H1′	3.12
	H1/H4/H4′/H1′	3.21
	H1/H3/B3/H1′	3.36
	H2/B2/B2′/H2′	3.09
	H2/H4/H4′/H2′	3.18
1.66	H1/B2/B3/B2′/H1′	3.14
	H1/H3/B3/H3′/H1′	3.20
	H2/B2/B3/B2′/H2′	3.04
	H1/B2/B3/B2′/H2′	3.12
	B1/B2/B3/B2′/H2′	unstable
2.00	H1/B2/H4/H4′/B2′/H1′	2.66
	H1/H3/B2/B2′/H3′/H1′	2.77
	H1/H3/H4/H4′/H3′/H1′	2.97
	H2/B2/H4/H4′/B2′/H2′	2.77
	B1/H2/B2/B3/B2′/H2′	2.89

Table B.10: Binding energies (referenced to $^1/_2\,O_2$) for a variety of oxygen configurations on the Re(10$\bar{1}$0)-(1×3) double MR surface at different coverages. The binding sites are as labeled in Fig. 5.10(b).

coverage (GML)	binding site	E_{bind} (eV)
0.33	H1	3.83
	H2	3.36
	H3	3.35
	H4	3.32
	H5	3.09
	B1	3.08
	B2	3.56
	T1	2.75
	B3	unstable
	B4	unstable
	T2	unstable
	T3	unstable
	T4	unstable
0.66	H1/B2′	3.66
	H1/H4	3.51
	H1/H1′	3.53
	H1/H3′	3.61
	H2/B2′	3.46
1.00	H1/H4/B2′	3.50
	H1/B2/B2′	3.50
	H1/H4/H3′	3.49
	H1/B2/H1′	3.39
	H1/H4/H1′	3.43
	H2/B2/B2′	3.32
1.33	H1/B2/B2′/H1′	3.30
	H1/H3/H3′/H1′	3.26
	H2/B2/B2′/H2′	3.22
1.66	H1/B2/B4/B2′/H1′	3.12
	H1/B2/H4/B2′/H1′	3.17
	H1/B2/H4/B2′/H1′	3.17
	H1/H3/H5/H3′/H1′	3.19
	H1/H3/H4/H3′/H1′	3.19
	H2/B2/H4/B2′/H2′	3.08
	B1/H2/B2/H4′/H2′	3.11
2.00	H1/B2/H4/H4′/B2′/H1′	2.87
	H1/B2/H4/H5′/B2′/H1′	2.78
	H1/H3/H4/H4′/H3′/H1′	3.04
	H1/H3/H4/H5′/H3′/H1′	3.04
	B1/H2/B2/H4/H4′/B2′	2.80
	B1/H2/B2/H4′/B2′/H2′	2.96

Table B.11: Binding energies (referenced to $^1/_2\,O_2$) for a variety of oxygen configurations on the Re(10$\bar{1}$0)-(1×3) triple MR surface at different coverages. The binding sites are as labeled in Fig. 5.10(c).

B.3 Re(10$\bar{1}$1)

B.3.1 Unreconstructed Re(10$\bar{1}$1)-(1×1)

	oxygen adsorbate	nitrogen adsorbate
binding site	E_{bind} (eV)	E_{bind} (eV)
H1	3.79	1.79
H2	3.56	1.53
H3	3.66	2.21
B1	3.60	–
B2	3.39	–

Table B.12: Binding energies (referenced to $^1/_2\,O_2$ or $^1/_2\,N_2$) for the adsorption of oxygen or nitrogen to different sites (as labeled in Fig. 5.20(a)) on the Re(10$\bar{1}$1)-(1×1) surface at 0.25 GML with (2×2) periodicity.

	oxygen adsorbate		nitrogen adsorbate	
	(2×1)-O	(1×2)-O	(2×1)-N	(1×2)-N
binding site	E_{bind} (eV)	E_{bind} (eV)	E_{bind} (eV)	E_{bind} (eV)
H1	3.80	3.51	1.81	1.31
H2	3.50	3.65	1.45	1.41
H3	3.68	3.44	2.07	1.60
B1	3.61	3.37	1.19	–
B2	3.39	3.54	1.07	–
T1	2.90	–	T1	0.18
B3	unstable	–	unstable	–
T2	unstable	–	unstable	–

Table B.13: Binding energies (referenced to $^1/_2\,O_2$ or $^1/_2\,N_2$) for the adsorption of oxygen or nitrogen to different sites (as labeled in Fig. 5.20(a)) on the Re(10$\bar{1}$1)-(1×1) surface at 0.5 GML with (1×2) or (2×1) periodicity.

	oxygen adsorbate	nitrogen adsorbate
binding site	E_{bind} (eV)	E_{bind} (eV)
H1	3.51	1.33
H2	3.53	1.31
H3	3.46	1.65
B1	3.32	0.71
B2	3.55	1.12
T1	2.82	0.30
B3	unstable	unstable
T2	unstable	unstable

Table B.14: Binding energies (referenced to $^1/_2\,O_2$ or $^1/_2\,N_2$) for the adsorption of oxygen or nitrogen to different sites (as labeled in Fig. 5.20(a)) on the Re(10$\bar{1}$1)-(1×1) surface at 1 GML.

	oxygen adsorbate	nitrogen adsorbate
binding site	E_{bind} (eV)	E_{bind} (eV)
H1/B2	3.10	0.40
H1/H3	3.00	0.93
H2/B1	3.06	0.47
H2/B2	3.11	0.43
H1/B2	3.10	0.40
B1/B2	unstable	unstable

Table B.15: Binding energies (referenced to $^1/_2\,O_2$ and $^1/_2\,N_2$) for a variety of oxygen or nitrogen configurations on the Re(10$\bar{1}$1)-(1×1) surface at 2 GML. The binding sites are as labeled in Fig. 5.20(a).

B.3.2 Reconstructed Re(10$\bar{1}$1)-(1×2)

	oxygen adsorbate	nitrogen adsorbate
binding site	E_{bind} (eV)	E_{bind} (eV)
H1	3.41	0.98
H2	3.86	1.60
H3	3.37	1.26
H4	3.23	1.08
H5	3.62	1.44
H6	2.72	0.53
H7	2.68	1.18
B2	3.26	0.94
B4	3.39	0.70
T1	2.73	0.20
B1	unstable	0.70

Table B.16: Binding energies (referenced to $^1/_2\,O_2$ or $^1/_2\,N_2$) for the adsorption of oxygen or nitrogen to different sites (as labeled in Fig. 5.20(b)) on the Re(10$\bar{1}$1)-(1×2) surface at 0.5 GML.

	oxygen adsorbate	nitrogen adsorbate
binding site	E_{bind} (eV)	E_{bind} (eV)
H2/B4	3.60	1.14
H2/H3	3.53	1.36
H2/H5	3.38	1.16
H5/H1	3.32	1.18
H5/H3	3.52	1.36

Table B.17: Binding energies (referenced to $^1/_2\,O_2$ and $^1/_2\,N_2$) for a variety of oxygen or nitrogen configurations on the Re(10$\bar{1}$1)-(1×2) surface at 1 GML. The binding sites are as labeled in Fig. 5.20(b).

	oxygen adsorbate	nitrogen adsorbate
binding site	E_{bind} (eV)	E_{bind} (eV)
H2/B4/H5/B2	3.06	0.67
H2/H3/H4/H5	3.19	1.03

Table B.18: Binding energies (referenced to $^1/_2\,O_2$ and $^1/_2\,N_2$) for a variety of oxygen or nitrogen configurations on the Re(10$\bar{1}$1)-(1×2) surface at 2 GML. The binding sites are as labeled in Fig. 5.20(b).

B.4 Re(13$\bar{4}$2)

	oxygen adsorbate	nitrogen adsorbate
binding site	E_{bind} (eV)	E_{bind} (eV)
H1	4.03	2.07
H2	3.17	1.49
H3	3.33	1.15
H4	3.31	1.38
H5	2.38	0.47
H6	3.67	2.35
H7	3.08	1.08
H9	3.24	1.22
H10	2.91	0.92
H11	3.46	1.56
B1	3.93	2.03
B6	3.57	1.03
B7	3.80	1.44
T1	3.53	0.08
T3	3.21	0.06
H8	unstable	0.93
T2	3.14	unstable
B2	unstable	unstable
B3	unstable	unstable
B4	unstable	unstable
B5	unstable	unstable
B8	unstable	unstable

Table B.19: Binding energies (referenced to $^1/_2\,O_2$ or $^1/_2\,N_2$) for the adsorption of oxygen or nitrogen to different sites (as labeled in Fig. 5.29) on the Re(13$\bar{4}$2) surface at 1 GML.

	oxygen adsorbate	nitrogen adsorbate
binding site	E_{bind} (eV)	E_{bind} (eV)
B1/H3	3.51	1.17
H1/B7	3.78	1.72
H1/H2	3.53	1.73
H1/H3	3.29	0.76
H1/H6	3.69	2.20
H1/H7	3.58	1.56
H1/B6	3.71	1.50
H1/B7	3.78	1.72
H2/H6	3.29	1.66
H3/H6	3.39	1.79
H4/H6	3.48	1.73
T1/H6	3.59	1.18
B1/H2	3.43	unstable
B1/H6	3.65	unstable
B1/H7	3.54	unstable
B1/B6	3.66	unstable
B1/B7	unstable	unstable

Table B.20: Binding energies (referenced to $^1/_2\,O_2$ and $^1/_2\,N_2$) for a variety of oxygen or nitrogen configurations on the Re(13$\bar{4}$2) surface at 2 GML. The binding sites are as labeled in Fig. 5.29.

oxygen adsorbate		nitrogen adsorbate	
binding site	E_{bind} (eV)	binding site	E_{bind} (eV)
H1/B7/H11	3.58	H1/H6/H9	1.89
H1/H6/H9	3.58	H1/H6/H4	1.38
H1/B7/H7	3.51	H1/H6/H7	1.75
H1/B7/H4	3.33	H1/H6/H9	1.89
H1/B7/B6	3.67	H1/H6/H10	1.78
H1/H6/H11	unstable	H1/H6/H2	1.72
H1/B7/H9	3.63	B1/H6/H9	unstable

Table B.21: Binding energies (referenced to $^1/_2\,O_2$ and $^1/_2\,N_2$) for a variety of oxygen or nitrogen configurations on the Re(13$\bar{4}$2) surface at 3 GML. The binding sites are as labeled in Fig. 5.29.

	oxygen adsorbate	nitrogen adsorbate
binding site	E_{bind} (eV)	E_{bind} (eV)
H1/B7/B6/H11	3.45	1.05
H1/B7/B6/H7	3.55	1.26
H1/H6/H9/H4	3.35	1.42
H1/H6/B6/H7	3.54	–
H1/H6/H9/H10	3.32	1.49
H1/H6/H9/H7	unstable	1.54

Table B.22: Binding energies (referenced to $^1/_2\,O_2$ and $^1/_2\,N_2$) for a variety of oxygen or nitrogen configurations on the Re(13$\bar{4}$2) surface at 4 GML. The binding sites are as labeled in Fig. 5.29.

oxygen adsorption		nitrogen adsorption	
binding site	E_{bind} (eV)	binding site	E_{bind} (eV)
H1/B7/B6/H7/H5	3.20	H1/H6/H9/H7/H2	1.06
H1/B7/B6/H7/H8	3.17	H1/H6/H9/H7/H5	0.81
H1/B7/B6/H7/H11	3.38	H1/H6/H9/H7/H11	1.20
H1/H6/B6/H7/H11	unstable	H1/H6/B6/H7/H8	1.22

Table B.23: Binding energies (referenced to $^1/_2\,O_2$ and $^1/_2\,N_2$) for a variety of oxygen or nitrogen configurations on the Re(13$\bar{4}$2) surface at 5 GML. The binding sites are as labeled in Fig. 5.29.

oxygen adsorption		nitrogen adsorption	
binding site	E_{bind} (eV)	binding site	E_{bind} (eV)
H1/B7/B6/H7/H11/H4	3.15	H1/H6/H9/H7/H11/H2	0.95
H1/B7/B6/H7/H11/H5	3.07	H1/H6/H9/H7/H11/H5	0.62
H1/B7/B6/H7/H11/H8	3.02	H1/H6/H9/H7/H11/H8	0.59

Table B.24: Binding energies (referenced to $^1/_2\,O_2$ and $^1/_2\,N_2$) for a variety of oxygen or nitrogen configurations on the Re(13$\bar{4}$2) surface at 6 GML. The binding sites are as labeled in Fig. 5.29.

Bibliography

[1] T. E. Madey, J. Guan, C.-H. Nien, C.-Z. Dong, H.-S. Tao, and R. A. Campbell, Surf. Rev. Lett. **3**, 1315 (1996).

[2] T. E. Madey, C. H. Nien, K. Pelhos, J. J. Kolodziej, I. M. Abdelrehim, and H. S. Tao, Surf. Sci. **438**, 191 (1999).

[3] Q. Chen and N. V. Richardson, Prog. Surf. Sci. **73**, 59 (2003).

[4] W. Chen, I. Ermanoski, Q. Wu, T. E. Madey, H. H. Hwu, and J. G. Chen, J. Phys. Chem. B **107**, 5231 (2003).

[5] W. Chen, I. Ermanoski, and T. E. Madey, J. Am. Chem. Soc. **127**, 5014 (2005).

[6] W. Chen, I. Ermanoski, T. Jacob, and T. E. Madey, Langmuir **22**, 3166 (2006).

[7] H. Wang, *Adsorbate-induced nanoscale faceting of rhenium surfaces*, Ph.D. thesis, Rutgers University (2008).

[8] M. Reyhan, H. Wang and T. E. Madey, Catal. Lett., **129**, 46 (2009).

[9] K. J. Song, J. C. Lin, M. Y. Lai, and Y. L. Wang, Surf. Sci. **327**, 1732 (1995).

[10] D. B. Danko, M. Kuchowicz, and J. Kolacziewicz, Surf. Sci. **552**, 111 (2004).

[11] R. E. Kirby, C. S. McKee, and M. W. Roberts, Surf. Sci. **55**, 725 (1976).

[12] R. E. Kirby, C. S. McKee, and L. V. Renny, Surf. Sci. **97**, 457 (1980).

[13] M. Sander, R. Imbihl, R. Schuster, J. V. Barth, and G. Ertl, Surf. Sci. **271**, 159 (1992).

[14] I. Ermanoski, K. Pelhos, W. Chen, J. S. Quinton, and T. E. Madey, Surf. Sci. **549**, 1 (2004).

[15] J. Gustafson, A. Resta, A. Mikkelsen, R. Westerström, J. N. Andersen, E. Lundgren, J. Weissenrieder, M. Schmid, P. Varga, and N. Kasper, Phys. Rev. B **74**, 035401 (2006).

[16] H. Wang, W. Chen, and T. E. Madey, Phys. Rev. B **74**, 205426 (2006).

[17] H. Wang, A. S. Y. Chan, W. Chen, P. Kaghazchi, T. Jacob, and T. E. Madey, ACS Nano **1**, 449 (2007).

[18] P. J. Knight, S. M. Driver, and D. P. Woodruff, Surf. Sci. **376**, 374 (1997).

[19] S. Vollmer, A. Birkner, S. Lucas, G. Witte, and C. Wöll, Appl. Phys. Lett. **76**, 2686 (2000).

[20] N. Reinecke, E. Taglauer, Surf. Sci. **454**, 94 (2000).

[21] D. A. Walko, I. K. Robinson, Phys. Rev. B **64**, 045412 (2001).

[22] I. Ermanoski, W. Swiech, and T. E. Madey, Surf. Sci. **592**, L299 (2005).

[23] T. E. Madey, W. Chen, H. Wang, P. Kaghazchi, and T. Jacob, Chem. Soc. Rev. **37**, 2310 (2008).

[24] H. v. Beijeren, Phys. Rev. Lett. **38**, 993 (1977).

[25] S. Prestipino, G. Santoro, and E. Tosatti, Phys. Rev. Lett. **75**, 4468 (1995).

[26] G. Mazzeo, E. Carlon, and H. v. Beijeren, Phys. Rev. Lett. **74**, 1391 (1995).

[27] V. P. Zhdanov and B. Kasemo, Phys. Rev. B: Condens. Matter Mater. Phys. **56**, R10067 (1997).

[28] C. Oleksy, Surf. Sci. **549**, 246 (2004).

[29] J. G. Che, C. T. Chan, C. H. Kuo, and T. C. Leung, Phys. Rev. Lett. **79**, 4230 (1997).

[30] C. T. Chan, J. G. Che, and T. C. Leung, Prog. Surf. Sci. **59**, 111 (1998).

[31] J. G. Che and C. T. Chan, Surf. Sci. **401**, L432 (1998).

[32] C. H. Nien, T. E. Madey, Y. W. Tai, T. C. Leung, J. G. Che, and C. T. Chan, Phys. Rev. B **59**, 10335 (1999).

[33] M. Born, and J. R. Oppenheimer, Ann. Phys. **84**, 457 (1927).

[34] F. Jensen, *Introduction to Computational Chemistry* (Wiley, New York, 1999).

[35] A. Groß, *Theoretical Surface Science* (Springer-Verlag, Berlin 2003).

[36] A. Szabo, N. Ostlund, *Modern Quantum Chemistry* (Dover, New York, 1989).

[37] R. J. Bartlett, J. Chem. Phys. **93**, 1697 (1989).

[38] C. Mller and M. S. Plesset, Phys. Rev. **46**, 618 (1934).

[39] P. Hohnberg and W. Kohn, Phys. Rev. B **136**, 846 (1964).

[40] W. Kohn and L. Sham, Phys. Rev. A **140**, 1133 (1965).

[41] L. H. Thomas, Proc. Cambridge Phil. Soc. **23**, 542 (1927).

[42] E. Fermi, Rend. Accad. Lincei **6**, 602 (1927).

[43] P. A. M. Dirac, Proc. Cambridge Phil. Soc. **26**, 376 (1930).

[44] J.P. Perdew, K. Burke, and M. Ernzerhof, Phys. Rev. Lett. **77**, 3865 (1996).

[45] M. C. Payne, M. P. Teter, D. C. Allan, T. A. Arias, J. D. Joannopoulos, Reviews of Modern Physics, **64**, No. 4, 1045 (1992).

[46] H. J. Monkhorst and J. D. Pack, Phys. Rev. B **13**, 5188 (1976).

[47] U. von Barth and C. D. Gelatt, Phys. Rev. B **21**, 2222 (1980).

[48] D.R. Hamann, M. Schlüter, and C. Chiang, Phys. Rev. Lett. **43**, 1494 (1979).

[49] D. Vanderbilt, Phys. Rev. B **41**, 7892 (1990).

[50] D. J. Singh, *Plane Wave, Pseudopotentials, and the LAPW Method* (Kluwer, Boston, 1994).

[51] R. M. Nieminen, J. Phys. Condens. Matter **14**, 2859, (2002).

[52] K. Reuter, C. Stampfl, and M. Scheffler, *Ab initio atomistic thermodynamics and statistical mechanics of surface properties and functions*, Handbook of Materials Modeling **1** (Springer-Verlag, Berlin, 2005).

[53] E. Kaxiras, Y. Bar-Yam, J. D. Joannopoulos, and K. C. Pandey, Phys. Rev. B **35**, 9625 (1987).

[54] M. Scheffler, *Physics of solid surfaces* (Elsevier, Amsterdam, 1987).

[55] G.-X. Qian, R. M. Martin, and D. J. Chadi, Phys. Rev. B **38**, 7649 (1988).

[56] K. Reuter and M. Scheffler, Phys. Rev. B **65**, 035406 (2001).

[57] *JANAF thermochemical tables*, edited by D. R. Stull and H. Prophet, 2nd ed. (U.S. Governm. Print. Office, Washington, D.C., 1971).

[58] Y. Zhang, V. Blum, and K. Reuter, Phys. Rev. B **75**, 235406 (2007).

[59] G. Wulff, Z. Krystallogr. **34**, 449 (1901).

[60] C. Herring, Phys. Rev. **82**, 87 (1951).

[61] A. S. Barnard and P. Zapol, J. Chem. Phys. **121**, 4276 (2004).

[62] V. A. Shchukin and D. Bimberg, Rev. Mod. Phys. **71**, 1125 (1999).

[63] D M. Zehner and H.E. Farnsworth, Surf. Sci. **30**, 335 (1972).

[64] J. Lenz, P. Rech, K. Christmann, M. Neuber, C. Zubragel, and E. Schwarz, Surf. Sci. **270**, 410 (1992).

[65] I. Ermanoski, C. Kim, S. P. Kelty, and T. E. Madey, Surf. Sci. **596**, 89 (2005).

[66] R. A. Campbell, J. Guan, and T. E. Madey, Catal. Lett. **27**, 273 (1994).

[67] R. Barnes, I. M. Abdelrehim, and T. E. Madey, Top. Catal. **14**, 53, (2001).

[68] W. Chen, T. E. Madey, A. L. Stottlemyer, J. G. Chen, P. Kaghazchi, and T. Jacob, J. Phys. Chem. C **112**, 19113 (2008).

[69] Z. Gai, R. G. Zhao, W. Li, Y. Fujikawa, T. Sakurai, and W. S. Yang, Phys. Rev. B: Condens. Matter Mater. Phys. **64**, 125201 (2001).

[70] K. Ohmori, Y. L. Foo, S. Hong, J. G. Wen, J. E. Greene, and I. Petrov, Nano Lett. **5**, 369 (2005).

[71] M. D. Segall, P. L. D. Lindan, M. J. Probert, C. J. Pickard, P. J. Hasnip, S. J. Clark, and M. C. Payne, J. Phys.: Condens. Matter **14**, 2717 (2002).

[72] B. G. Pfrommer, M. Cote, S. G. Louie, and M. L. Cohen. **131**, 133-140 (1997).

[73] F.D. Murnaghan, Proc. Nat. Acad. Sci. **30**, 244 (1944).

[74] J.H. Rose, J.R. Smith, F. Guinea, and J. Ferrante. Phys. Rev. B. **29**, 2963 (1984).

[75] A. Michaelides and M. Scheffler, *An introduction to the theory of metal surfaces*, To appear in: Textbook of Surface and Interface Science, Vol. I, (Wiley-VCH).

[76] http://en.wikipedia.org/wiki/Rhenium

[77] C. Kittel, *Introduction to Solid State Physics* (Wiley, New York, 1996).

[78] P. Blaha, K. Schwarz, G. K. H. Madsen, D. Kvasnicka, and J. Luitz, WIEN2k, an augmented plane wave + local orbitals program for calculating crystal properties, Technical University Vienna, Austria, (2001).

[79] W. X. Li, C. Stampfl, and M. Scheffler, Phys. Rev. B **65**, 075407 (2002).

[80] M. Todorova, K. Reuter, and M. Scheffler, J. Phys. Chem. B **108**, 14477 (2004).

[81] M. V. Ganduglia-Pirovano and M. Scheffler, Phys. Rev. B **59**, 15 533 (1999).

[82] A. Soon, M. Todorova, B. Delley and C. Stampfl, Phys. Rev. B **73**, 165424 (2006).

[83] E. Lundgren, J. Gustafson, A. Mikkelsen, J.N. Andersen, A. Stierle, H. Dosch, M. Todorova, J. Rogal, K. Reuter, and M. Scheffer, Phys. Rev. Lett. **92**, 046101 (2004).

[84] K. T. Jacob, S. Mishra, and Y. Waseda. Thermochimica Acta. **348** , 61, (2000).

[85] A. Magnéli, Acta Chemica Scandinavica, **11**, 28 (1957).

[86] *The Oxide Handbook*, edited by G.V. Samsonov (IFI/ Plenum, New York, 1982).

[87] P. Clark, B. Dhandapani, and S. Oyama, Appl. Catal. A **184**, 175 (1999).

[88] M. W. Finnis and V. Heine, J. Phys. F:Metal Phys. **4**, 37, (1974).

[89] J. L. F. DaSilva, C. Stampfl, and M. Scheffler, Surf. Sci. **600**, 703 (2006).

[90] M. K. Debe and D. A. King, Phys. Rev. Lett. **39**, 708 (1977).

[91] M. S. Altman, P. J. Estrup, and I. K. Robinson, Phys. Rev. B **38**, 5211 (1988).

[92] H. Landskron, N. Bickel, K. Heinz, G. Schmidtlein, and K. Müller, J. Phys. Condens. Mattter **1**, 1 (1989).

[93] G. Schmidt, H. Zagel, H. Landskron, K. Heinz, K. Muller, and J. B. Pendry, Surf. Sci. **271**, 416 (1992).

[94] V. Fiorentini, M. Methfessel, and M. Scheffler, Phys. Rev. Lett. **71**, 1051 (1993).

[95] W. Moritz and D. Wolf, Surf. Sci. Lett. **88**, L29 (1979).

[96] W. Moritz and D. Wolf, Surf. Sci. Lett. **163**, L655 (1985).

[97] J. Möller, H. Niehus, and W. Heiland, Surf. Sci. **166**, L111 (1986).

[98] K. M. Ho and K. P. Bohnen, Phys. Rev. Lett. **59**, 1833 (1987).

[99] M. Copel and T. Gustafsson, Phys. Rev. Lett. **57**, 723 (1986).

[100] P. Fery, W. Moritz, and D. Wolf, Phys. Rev. B **38**, 7275 (1988).

[101] T. Gritsch, D. Coulman, R. J. Behm, and G. Ertl, Phys. Rev. Lett. **63**, 1086 (1989).

[102] R.I. Masel, *Principles of adsorption and reaction on solid surfaces* (Wiley, New York 1996).

[103] P. J. Estrup, *Chemistry and Physics of Solid Surfaces* V, edited by R. Vanselow and R. Howe, Springer Series of Chemical Physics, p. 205 (Springer-Verlag, Berlin, 1984).

[104] K. W. Jacobsen and J. K. Nørskov, *The Structure of Surfaces II*, edited by J. F. van der Veen and M. A. Van Hove, Springer Series in Surface Science Vol. 11, p. 118 (Springer-Verlag, Berlin, 1988).

[105] H. L. Davis and D. M. Zehner, J. Vac. Sci. Technol. **17**, 190 (1980).

[106] C. Y. Fan and K. Jacobi, Surf. Sci. **482-485**, 21 (2001).

[107] D. Rosenthal, I. Zizak, N. Darowski, T.T. Magkoev, and K. Christmann, Surf. Sci. **600**, 2830 (2006).

[108] M. Gierer, H. Over, P. Rech, P. Schwarz, and K. Christmann, Surf. Sci. Lett. **370**, 201 (1997).

[109] S. Schwegmann, A. P. Seitsonen, V. De Renzi, H. Dietrich, H. Bludau, M. Gierer, H. Over, K. Jacobi, M. Scheffler, and G. Ertl, Phys. Rev. B **57**, 15487 (1998).

[110] H. Wang (private communication).

[111] P. Kaghazchi, T. Jacob, H. Wang, W.Chen, and T. E. Madey, Phys. Rev. B **79**, 132107 (2009).

[112] E. Schwarz, K. H. Schwarz, C. Gonser-Buntrock, M. Neuber, and K. Christmann, Vacuum **41**, 180 (1990).

[113] H. Oppermann and Z. Anorg. Allg. Chem. **523**, 135 (1985).

[114] J. E. Battles, G. E. Gundersen, and R. K. Edwards, J. Phys. Chem. **72** (12), 3963 (1968).

[115] V. D. Budon and A. L. Tseft, Izv. Akad. Nauk Kaz. SSR, Ser. Metall. Obogashch. Ogneuporov, No. 3, 49 (1958).

[116] V. I. Deev and V. I. Smirnov, Dokl. Akad. Nauk SSSR **140** (4), 822 (1961).

[117] R. Pantel, M. Bujor, and J.Bardolle, Surf. Sci. **83**, 228 (1979).

[118] P. Kaghazchi and T. Jacob, Phys. Rev. B **76**, 245425 (2007).

[119] C. M. Chan, K. L. Luke, M. A. van Hove, W. H. Weinberg, and S. P. Withrow, Surf. Sci. **78**, 386 (1978).

[120] J. L. Taylor, D. E. Ibbotson, and W. H. Weinberg, Surf. Sci. **79**, 349 (1979).

[121] S. Ladas, S. Kennou, N. Hartmann, and R. Imbihl, Surf. Sci. **382**, 49 (1997).

[122] H. Bu, M. Shi and J. W. Rabalais, Surf. Sci. **236**, 135 (1990).

[123] H. Bu, M. Shi, K. Boyd, and J. W. Rabalais, J. Chem. Phys. **95**, 2882 (1991).

[124] M. Peuckert, Surf. Sci. **144**, 451 (1984).

[125] J. Rogal, *Stability, composition and function of palladium surfaces in oxidizing environments: A first-principles statistical mechanics approach*, Ph.D. thesis, Free University Berlin (2006).

[126] J. Behler, *Dissociation of Oxygen Molecules on the Al(111) Surface*, Ph.D. thesis, Technical University Berlin (2004).

[127] *CRC handbook of chemistry and physics*, edited by D. R. Lide and H.P.R. Frederikse, 76th ed. (CRC, 1995).

[128] G. Herzberg. *Molecular Spectra and Molecular Structure, I. Spectra of Diatomic Molecules* (van Nostrand Reinhold Company, New York, 1950).

[129] O. Gunnarsson and R. O. Jones. Phys. Rev. B **31**, 7588 (1985).

[130] A. Soon, L. Wong, B. Delley, and C. Stampfl, Phys. Rev. B **77**, 125423 (2008).

[131] C. Stampfl and C.G. Van de Walle, Phys. Rev. B **59**, 5521 (1999).

[132] A. D. Becke, *The Challenge of d and f Electrons*, ACS Symposium Series No. 394, edited by D. R. Salahub and M. C. Zerne, p. 165 (American Chemical Society, Washington DC, 1989).

Summary

Since high-index clean metal surfaces typically have lower surface atom densities and higher surface free energies compared to the close-packed surfaces of the same metal they can be used as the basis for surface reconstruction and facet formation studies. In this context, experiments performed by the group of Prof. Madey from the Rutgers University revealed that on the Re(11$\bar{2}$1) and Ir(210) surfaces strongly interacting adsorbates are able to induce the formation of well defined nanostructures after annealing the system at elevated temperatures. Motivated by these observations we used density functional theory (DFT) calculations to study the adsorption of oxygen and nitrogen on the different surface orientations, which are involved in the nanostructures on Re(11$\bar{2}$1) and Ir(210). The free energies of the various surfaces relevant for the faceting were then evaluated using the *ab initio* atomistic thermodynamics approach that allows investigating of the stability of surfaces being in contact with a surrounding gas atmosphere (reservoir), which is being characterized by a partial pressure p and temperature T.
For adsorbate-induced faceting of Re(11$\bar{2}$1), in a first step we studied the clean and O or N-covered Re(11$\bar{2}$1), (10$\bar{1}$0), (10$\bar{1}$1), and (13$\bar{4}$2) surfaces by DFT to provide detailed information on the structure and energetics of a variety of adsorbate coverages. Constructing the (p,T)-surface phase diagrams of Re(11$\bar{2}$1) in contact with an oxygen or nitrogen atmosphere, we could reproduce the experimental observations: Oxygen adsorption below 900 K (p_{O_2}=5×10^{-10} atm) leads to four-sided pyramids exhibiting (10$\bar{1}$0), (01$\bar{1}$0), (10$\bar{1}$1), and (01$\bar{1}$1) faces, while nitrogen adsorption causes two-sided ridges, combining (13$\bar{4}$2) and (31$\bar{4}$2) faces, to become thermodynamically favored at temperatures below 1080 K (p_{N_2}=5×10^{-10} atm).
Regarding oxygen-induced faceting of Ir(210), we obtained the stability of clean and oxygen-covered surfaces of Ir(210), (311), and (110). The corresponding surface phase diagram showed that the experimentally observed three-sided pyramids with one (110) and two {311} facets are stable over the entire temperature range at which oxygen is adsorbed on the surface at coverages $>$ 0.45 physical ML. At high temperatures, STM images on the faceted surface revealed that some (110) faces show a stepped double-missing row superstructure. Our calculations supported also this result: While at lower temperatures the facets consist of (311), (31$\bar{1}$), and (110) regular faces, at higher temperatures the (110) face is found to be reconstructed, leading to (311)/(31$\bar{1}$)/(110) superstructure facets.

Therefore, our results, which are in agreement with experimental observations, suggest that by choosing appropriate adsorbate/substrate and (p, T)-conditions it is not only possible to tailor the surface morphology, but also to stabilize new surfaces.
Our work has important implications for Ir and Re-based catalysts that operate under oxygen-rich or nitrogen-rich conditions since the structures of the catalysts often affect their performance.

Zusammenfassung

Relativ zu dicht gepackten Oberflächen besitzen saubere, hoch-indizierte Metalloberflächen eine niedrigere Atomdichte an der Oberfläche und somit meist auch eine höhere freie Energie. Deswegen kann man sie als Basis für Studien von Oberflächenrekonstruktionen und der Facettenbildung heranziehen. In diesem Zusammenhang konnte die Gruppe von Prof. Madey an der Rutgers Universität in New Jersey experimentell zeigen, dass auf Re(11$\bar{2}$1) und Ir(210) Oberflächen durch stark wechselwirkende Adsorbate in Kombination mit kontrolliertem Aufheizen wohl-definierte Nanostrukturen ausgebildet werden.
Motiviert durch diese Ergebnisse untersuchten wir mit Hilfe der Dichtefunktionaltheorie (DFT) die Adsorption von Sauerstoff und Stickstoff an verschiedenen Oberflächenorientierungen, welche mit den Nanostrukturen von Re(11$\bar{2}$1) und Ir(210) in Zusammenhang stehen.
Die freie Energie der verschiedenen für die Facettenbildung relevanten Oberflächen wurde anhand der "*ab initio* atomistic thermodynamics"-Methode bestimmt. Diese erlaubt es, die Stabilität verschiedener Oberflächen in Anwesenheit einer Gasatmosphäre (Reservoir), charakterisiert durch den Druck p und die Temperatur T, zu bestimmen.
Um die, durch Adsorption induzierte, Facettenbildung der Re(11$\bar{2}$1) Oberfläche zu untersuchen, wurden sowohl saubere als auch mit O- oder N-bedeckte Re(11$\bar{2}$1), Re(10$\bar{1}$0), Re(10$\bar{1}$1) sowie Re(13$\bar{4}$2) Oberflächen untersucht. DFT Simulationen für verschiedene Bedeckungen lieferten Informationen über die Struktur und Energetik. Darauf aufbauend konnte ein (p, T)-Oberflächenphasendiagramm der Re(11$\bar{2}$1) Oberfläche in Sauerstoff- und Stickstoffatmosphäre erstellt werden. Die experimentellen Ergebnisse konnten reproduziert werden: Sauerstoffadsorption unter 900 K (p_{O_2}=5×10^{-10} atm) führt zu 4-seitigen Pyramiden mit (10$\bar{1}$0), (01$\bar{1}$0), (10$\bar{1}$1) und (01$\bar{1}$1) Seitenflächen. Bei Stickstoffadsorption bilden sich unter 1080 K (p_{N_2}=5×10^{-10} atm) 2-seitige "Ridges" (Wälle) mit (13$\bar{4}$2) und (31$\bar{4}$2) orientierten Seitenflächen aus.
Im Falle der sauerstoffinduzierten Facettenbildung auf Ir(210) untersuchten wir saubere und O-bedeckte Ir(210), (311) und (110) Oberflächen. Im dazugehörigen Oberflächenphasendiagramm erkennt man, wie im Experiment, dass 3-seitige Pyramiden mit einer (110) und zwei (311) Seitenflächen über den gesamten Temperaturbereich bei einer Sauerstoffbedeckung von über 0.45 physikalischen ML

am stabilsten sind. STM Bilder der Oberfläche zeigten, dass bei hohen Temperaturen manche der (110) Seitenflächen eine Rekonstruktion ("stepped missing double row structure") besitzen. Unsere Berechnungen bestätigen auch dieses Beobachtung: Während sich bei tiefen Temperaturen (311), $(31\bar{1})$ und (110) Seitenflächen bilden, rekonstruiert die (110) Seitenfläche bei höheren Temperaturen und führt damit zu (311)/$(31\bar{1})$/(110)-rekonstruiert Seitenflächen.
Diese Ergebnisse, welche in guter Übereinstimmung mit dem Experiment sind, zeigen, dass bei geeigneter Wahl von Adsorbat und Substrat, sowie angemessener Temperatur- und Druck-Bedingungen die Oberflächenmorphologie gezielt gesteuert und sogar neue Oberflächen stabilisiert werden können.
Diese Ergebnisse dieser Arbeit sind sicherlich relevant für Ir und Re-basierte Katalysatoren, die unter sauerstoff- oder stickstoffreichen Bedingungen eingesetzt werden, da die Struktur oft großen Einfluss auf die Leistung des Katalysators haben kann.

Acknowledgements

First of all, I would like to thank Timo Jacob for his continued support and advise during the years of my Ph. D. I was very fortunate to be his Ph. D. student.
I am grateful to Prof. Dr. E.K.U. Gross for his willingness to act as the second referee and the members of the committee at the Free University of Berlin for taking the time for the exam and for reading this thesis.
For the suggestions and discussions I would like to thank Dr. Aloysius Soon, Dr. Hong Jiang, Dr. Jutta Rogal, Dr. Johan Carlson, Prof. Dr. Alex Bradshaw, and Prof. Dr. Roberto Car.
A special thanks goes to Prof. Dr. Theodore E. Madey, Dr. Wenhua chen, and Dr. Hao Wang for the discussions on their experimental data.
Additionally, I would like to gratefully acknowledge Matthias Scheffler for giving me the opportunity to do this work at the Fritz-Haber Institute.
For the nice time at the Fritz-Haber Institute I thank all my colleagues; especially Biswajit Santra, Javier Carrasco, and Björn Hülsen.
I am greatly indebted to my wife and parents for their encouragement, support, and patience during the years of my study.
Finally, I gratefully acknowledge the DAAD for funding of this research.